THESIS

EXPERIMENTAL ASSESSMENT OF CRACKED STEEL BEAMS UNDER MECHANICAL LOADING AND ELEVATED TEMPERATURES

Submitted by

Bashir Ahmadi

Department of Civil and Environmental Engineering

In partial fulfillment of the requirements

For the Degree of Master of Science

Colorado State University

Fort Collins, Colorado

Fall 2016

Master's Committee:

Advisor: Hussam Mahmoud

John van de Lindt
Kelly Strong

ABSTRACT

EXPERIMENTAL ASSESSMENT OF CRACKED STEEL BEAMS UNDER MECHANICAL LOADING AND ELEVATED TEMPERATURE

Bridge fire is a major engineering problem that has been gaining attention by researchers and engineers. As reported in the New York Department of Transportation database, there has been approximately 50 cases of bridge collapse due to fire nationwide with many more cases where fires resulted in repairable damage. The fires are typically due to vehicle crash, arson, and in some cases wildfires. The affected bridges are mostly fabricated from steel, concrete, and temper. The problem of bridge fire is further aggravated by the presence of fatigue cracks in steel bridges. Various experimental and numerical studies have been conducted to evaluate the response of steel beams under elevated temperature. However, to date, there is lack of information on the response of steel beams with pre-existing cracks under elevated temperature.

The importance of evaluating cracked steel beams under elevated temperature stems from the fact that many steel bridges that are currently in service suffer from major deteriorations manifested in the presence of fatigue cracks that are the result of cyclic loading from daily traffic. With no available data on failure behavior of cracked steel beams under fire, this thesis introduces a new testing protocol for evaluating the response of cracked steel beams under elevated temperature. Specifically, the results of experimental tests, conducted at the structural engineering laboratory at Colorado State University, of four initially cracked W8x24 steel beams under point loading and non-uniform elevated temperature are presented. The cracks are introduced across the bottom

flange and the beams are loaded to failure while being subjected to various non-uniform elevated temperature distributions varying from 200 ^{o}C to 600 ^{o}C.

The competition between two different failure modes: excessive deflection and fracture along the crack plane, is evaluated with respect to temperature distributions in the beams. In cases where fracture prevailed, different types of fractures were observed including brittle fracture, ductile fracture, and brittle/ductile transition failure, which depended on the temperature distribution. The results presented include load versus displacement and time versus temperature curves. In addition, digital image correlation method was utilized to develop strain and displacement fields around the cracked regions. This experimental study provides an alternative method for evaluating cracked beams under elevated temperature and will provide engineers with insight into various behavioral aspects of steel beams under the investigated loading demands. Furthermore, the results of this study can be used to calibrate advanced numerical finite element models, capable of capturing large deformations and fracture, which can in turn be used to conduct a parametric study for various sizes of bridge girders under an ensemble of thermal loading scenarios.

ACKNOWLEDGEMENTS

It has been two years since I have joined Dr. Hussam Mahmoud's research team, first as an undergraduate research assistant then as a graduate research assistant where I had the privilege to have him as my advisor for my master's thesis research. Under the leadership and guidance of Dr. Hussam Mahmoud, I have gained tremendous amount of knowledge in connecting engineering theories I learned in classes with practical experimental research works at the structural engineering laboratory of Engineering Research Center at Colorado State University. Dr. Hussam Mahmoud has always given me challenging engineering problems to solve and pushed me beyond my limits. This has led me to gain experience and knowledge in diverse engineering subjects. I am so grateful to have had the opportunity of studying and working under Dr. Hussam Mahmoud's supervision.

I would like to thank my committee members Dr. John van de Lindt and Dr. Kelly Strong for taking their time to review my research work and giving me their valuable insights. I am thankful to Dr. Mehrdad Memari, postdoctoral fellow at Colorado State University, for sharing his knowledge with me in research related work and assisting me throughout the experimental program. I would also like to thank Dr. Mehrdad Memari for helping me enhance my skills in computer modeling and data analysis in the last two years. I also want to talk Junior Garza and Matthew Szydlowski of CSU Engineering Research Center for their tremendous help in construction and preparation of the test setup.

A special acknowledgement goes to Ariel Skelley, who has assumed the role of “Mom”, since I first came to the United States as a high school exchange student in 2005. Her love and support has been pivotal in helping me complete my education. I am extremely grateful for my American family, who have made me one of their own.

Thanks to Abdul Majid Zabuli (AMZ) Foundation scholarship program administered through the U.S. State Department which I was a recipient in my undergraduate studies at Colorado State University. AMZ scholarship paved the way for me to get to my graduate studies.

I would like to thank my brother Abdul Basir for his support. Thanks also to my brothers Rahmikhuda and Zamir for being there for me. I want to thank my friend Omar Amini, Ph.D. student at Colorado State University, for his help in reviewing chapters of this thesis. Thanks to my friend Shukran, Ph.D. student at Colorado State University, for being a supportive friend during this journey. Thanks to my friend Maiwand and all other family and friends who have helped me throughout this journey.

DEDICATION

I am dedicating this thesis to the loving memory of my parents and their endless struggle and commitment for sending their children to school during hard times of war-ravaged Afghanistan. Daada Jaan, Adai Jaan, my childhood dream finally came true today and I have earned my engineering degrees. Your prayers have always given me the strength to stand firm. I am so proud to be your son and to be raised by you. You will live in my memories forever. May God have you both rest in the highest heaven. I will follow the dignified way of life that you had thought me and use my education to help the ones in need.

TABLE OF CONTENTS

LIST OF TABLES

LIST OF FIGURES

Chapter 1 - Introduction

1.1 Problem Statement

The use of steel as a material in structures has proven to be advantageous due its relative high stiffness, strength and ductility. Steel is also favored in construction due to lower project cost, sustainability, speed of construction, and aesthetic appeal of steel (AISC, 2007). The downside of steel as a structural material is its performance under fire and elevated temperature because steel has relatively high conductivity and low specific heat (Mahmoud et al., 2015, Aziz, 2015, Memari and Mahmoud, 2014, Memari et al., 2014). Although current codes provide fire protection safety and insulation provisions for buildings construction, the American Association of State Highway and Transportation (AASHTO) specifications has no provisions for insulation and fire protection of bridges. This makes steel bridges and bridges with steel elements susceptible to excessive demand due to direct fire loading. Previous events have shown fire cases on bridges to be mainly due to accidents of large truck carrying flammable and combustible materials on or under highway bridges (Wright et al., 2013, Bradt 2011, Garlock et al., 2012, Aziz et al., 2015). The potential for exposure of steel beams or girders to fire loading is further complicated by presence of fatigue cracks, which are typically viewed as a serviceability issue in steel bridges. Undoubtedly, the presence of a crack will have an impact on the overall behavior of beams or girders at elevated temperature.

Similarly, findings of a nationwide survey conducted by New York Department of Transportation (NYDOT) shows bridge collapse due to fire to be three times greater than bridge collapse due to earthquake between the time period of 1990 to 2005 (Aziz, 2015). Loss of life has not been recorded because of bridge fire yet; however, loss of serviceability of bridges connecting major

interstate highways could lead to major economic drawdowns due to ground transportation closure (Wright et al., 2013). As previously noted, the main reason for bridge fire is due to accidents of large trucks transporting flammable liquids and combustible materials on or beneath a bridge. Other factors also contribute to bridge fire such as crashing of smaller vehicles and wild fire; however, their effects and frequency are negligible (Garlock et al., 2012).

Fatigue cracking is the formation and propagation of cracks in structural members in tension-tension or tension-compression cyclic service loading. There are 182,706 steel bridges in the United States, which make up 30 percent of all U.S. bridges (NBI, 2013). Over the span of their service life, many steel bridges experience repetitive traffic live load that makes the structural members or sub-assemblies vulnerable to fatigue cracks. In fact, more than 90% damage in steel bridges is due to fatigue cracking (Naser & Serrano, 2011). Although fatigue is a serviceability limit state, crack growth in steel bridge girders could lead to sudden fracture when the un-cracked cross section of the steel element is sufficiently reduced and if the crack is left unrepaired (Fisher et al., 1998, Connor et al., 2005, Dexter et al., 2013, Dexter et al., 2007, Mahmoud and Dexter, 2005, Mahmoud and Riveros 2014). The role of fatigue cracks in steel elements for the assessment of bridges becomes more critical for fracture critical bridges. Fracture critical bridges are bridges where only two main beams or girders are the main load carrying elements in the bridge and fracture of any of the two girders could lead to total collapse of the bridge.

In order to avoid catastrophic failures in fracture-critical steel bridges, Fracture Control Plan (FCP) was developed through a combined effort of AASHTO and AWS in 1976 and adopted by the steel bridge industry (Dexter et al., 2013, Connor et al., 2005). The development and implementation

of CFP was a result of Point Pleasant Bridge collapse in West Virginia in 1967 due to brittle fracture of a fracture-critical member supporting the main span of the suspension bridge. (Dexter et al., 2013). With focus on improving design, material, shop inspection of fabrication and routine inspection of in-service structures, specifically those of non-redundant structures, Fracture Control Plan provisions were developed and revisions were made to AASHTO and AWS bridge design guidelines to minimize fatigue and fractures problems in steel bridges (Dexter et al., 2013).

The use of FCP provisions has undoubtedly been pivotal in mitigating catastrophic failures in non-redundant steel bridges through placing stringent requirements on acceptable flaw sizes, during the fabrication process. However, current significant deterioration in U.S. infrastructure and in steel bridges, coupled with the lack of federal funding available for repairing cracked bridges, have caused many engineers to defer to basic concepts of fracture mechanics to determine the criticality of a crack and when it should be repaired. The use of simple fracture mechanics in making such assessment, in a so-called fitness-for-purpose evaluation (Dexter et al. 2007) has been confined only to linear elastic fracture mechanics with limited crack tip plasticity under service temperature. In cases where existing cracks are present and when the member is subjected to fire loading, linear elastic fracture mechanics will no longer be a viable assessment approach.

The above discussion highlights the susceptibility of steel bridges to the combined hazards of fire loading and deterioration as manifested in the presence of fatigue cracks, which has not been previously addressed. Therefore, understanding the performance of steel beams or girders under elevated temperature in the presence of pre-existing cracks is a first step in assessing steel bridges under such conditions. This research is intended to fill the gap in the literature on the performance of steel beams under elevated temperature and in the presence of large cracks.

1.2 Objective and Scope

Numerous studies have been previously conducted on structural performance of steel bridges and steam beam under elevated temperature, however, there is lack of research on the performance of steel beams with large cracks under non-uniform temperature, which represents the case of a cracked bridge beam subjected to fire event. The objective of this research study is to add to existing database on experimental behavior of beams under elevated temperature to include the behavior not only under elevated temperature but also in the presence of a large crack. In order to study the failure and fracture characteristics of steel beams with large cracks at elevated temperature, an experimental testing program is designed and implemented as shown in Figure 1-1 below. Figure 1-1 shows the main tasks required for the assessment of the cracked beams under fire.

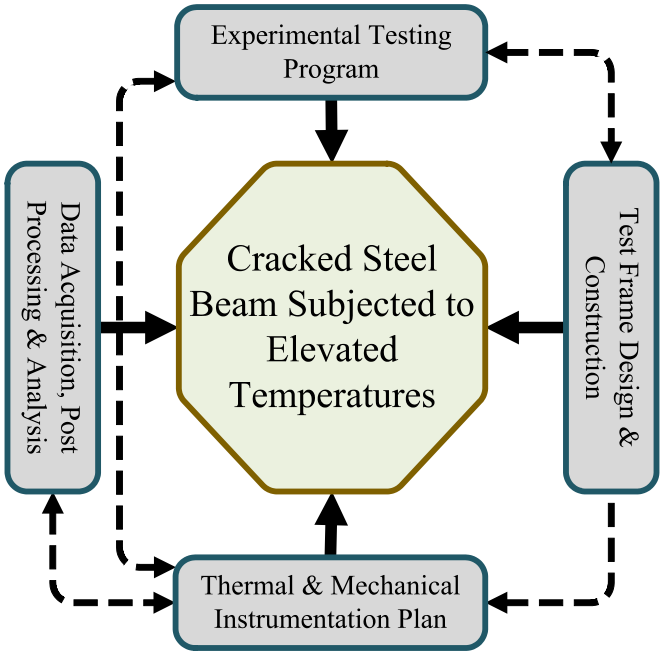

Figure 1-1: Proposed project methodical approach

In order to accomplish the project objective, the following tasks and subtasks are required:

- Task 1: Conduct Comprehensive Literature Review

- Task 2: Devise a New Experimental Setup and Instrumentation Program for Evaluating Cracked Steel Beams Subjected to Fire Loading and Mid Span Mechanical Point Load
    - Prepare four beam specimens with bottom flange crack
    - Design and construct testing frame with proper insulation to mount the hydraulic actuator for mechanical loading at mid span
    - Design and construct smaller horse-rack frame to devise ceramic heaters for heat transfer application to the beam specimens
    - Utilize two proportional–integral–derivative controller (PID controller) for mechanical and thermal load application
    - Develop an instrumentation program to collect data during testing including thermocouples and strain gauges
    - Configure two data acquisition (DAQ) systems to collect mechanical load data and temperature distribution
    - Create random marks at the front of the beam specimens around the cracked region for digital image correlation (DIC) analysis using open source MATLAB code
    - Take reference and loaded pictures from the marked region for DIC analysis in order to develop displacement and strain fields around the cracked region independent of mechanical load DAQ system
    - Develop testing protocol for thermal application
    - Develop Mechanical loading protocol (Monotonic step wise mid-span loading)
- Task 3: Execute the Testing Program

- Apply the thermal testing protocol input time-temperature curves for each specimen
- Apply mechanical load according to the mechanical testing protocol after the temperature reaches a steady state non-uniform distribution
- Collect mechanical load data and thermocouple data from the beam using the DAQ systems
- Conduct finite difference analysis to create 2-D steady state temperature distribution using thermocouple data and interpolation as boundary condition in MATLAB code

- Task 4: Discuss and Interpret the Experimental Results
    - Discus the output time-temperature curves
    - Evaluate load-displacement plot in terms of degradation in stiffness, strength, ductility and maximum deflection
    - Evaluate the fractured surfaces and distinguish between the different failure zones
    - Assess the effect of temperature distribution on the fracture characteristics of the beams (brittle, ductile, or transition)
    - Evaluate strain and deflection in the cracked beams subjected to elevated temperature in comparison to a cracked beam under ambient temperature

1.3 Organization of the thesis

A new experimental testing program along with an instrumentation plan for evaluating cracked steel beam under non-uniform temperature was developed. Four steel beam specimens with a large

crack at the bottom flange were successfully tested under non-uniform temperature and mid-span mechanical loading. This experimental program was completed using the Structural Engineering Laboratory at the Engineering Research Center at Colorado State University (CSU) and utilized the new large-scale fire testing capabilities at CSU.

This thesis is organized in five chapters. Chapter one includes the problem statement, scope of the work, and a brief summary of the methodological approach devised and implemented to execute the proposed research. Chapter two contains background studies and an extensive literature on steel beam and bridge performance and behavior under fire events. Chapter three discusses test methodologies and design of the experimental testing program including instrumentation plan and data acquisition systems. Chapter four presents evaluation and interpretation of the results. Chapter five includes conclusion, field implications, and recommendations for future work.

Chapter 2 - Background and Literature Review

2.1 Introduction

Since there are no fire protection and safety provisions or guidelines provided by AASHTO (2004) for bridges in the United States due to lower risk of life safety on bridges compared with buildings, there has been only handful of research studies on structural behavior of bridges under fire event. Of the existing work, there are no published studies on the characteristics and failure of bridges with pre-existing cracks due to fatigue under elevated temperature. Additionally, classical linear elastic fracture mechanics, which is typically employed in quantifying the potential for fracture in steel bridges is valid for bridge steel beams under service loads and at ambient or lower temperature. Response and failure of bridge steel beams with large crack under ultimate load and applied temperature distribution simulating fire event is a nonlinear problem, which should be quantified experientially. This chapter contains state-of-the-art literature review on bridge fire event as an engineering problem and the current buildings fire code provisions that is relevant to bridges. Review of experimental and numerical research conducted on behavior of steel bridges or their structural elements under fire events. Mechanical and fracture properties of steel at elevated temperature will be also discussed. In addition, fatigue as a serviceability limit state as an engineering problem in steel bridges will be reviewed. Last, some background on fracture mechanics failure criteria will be summarized.

2.2 Statistics of Bridge Fire Events

Bridge fires are caused by crashing of trucks carrying large amounts of fuel and other flammable and combustible material, on the surface and beneath the bridge or at the vicinity of the bridge (Garlock et al., 2012). There are also other factors that attribute to bridge fire such as wild fire and

small vehicle accident, however, their effect and frequency have been minor (Ahrens, 2000). New York Department of Transportation (NYDOT) recorded a total of 1746 cases of bridge collapse in 18 states from 1960 to 2008 through a nationwide survey (Wright et al., 2013). NYDOT survey described collapse as permanent structural damage where the bridge cannot function for its intended service. Figure 2-1 includes a bar chart of the bridge collapse summary indicating the reason for collapse. The majority of the bridge collapse, 1006 cases, were due to hydraulic phenomena such as flood, while collision and overloading accounted for 228 and 220 bridge collapse cases. Fire caused 50 cases of the bridge collapse while 19 collapses were due to earthquake. Bridge collapse because of deterioration was 67, higher than causes of fire and earthquake.

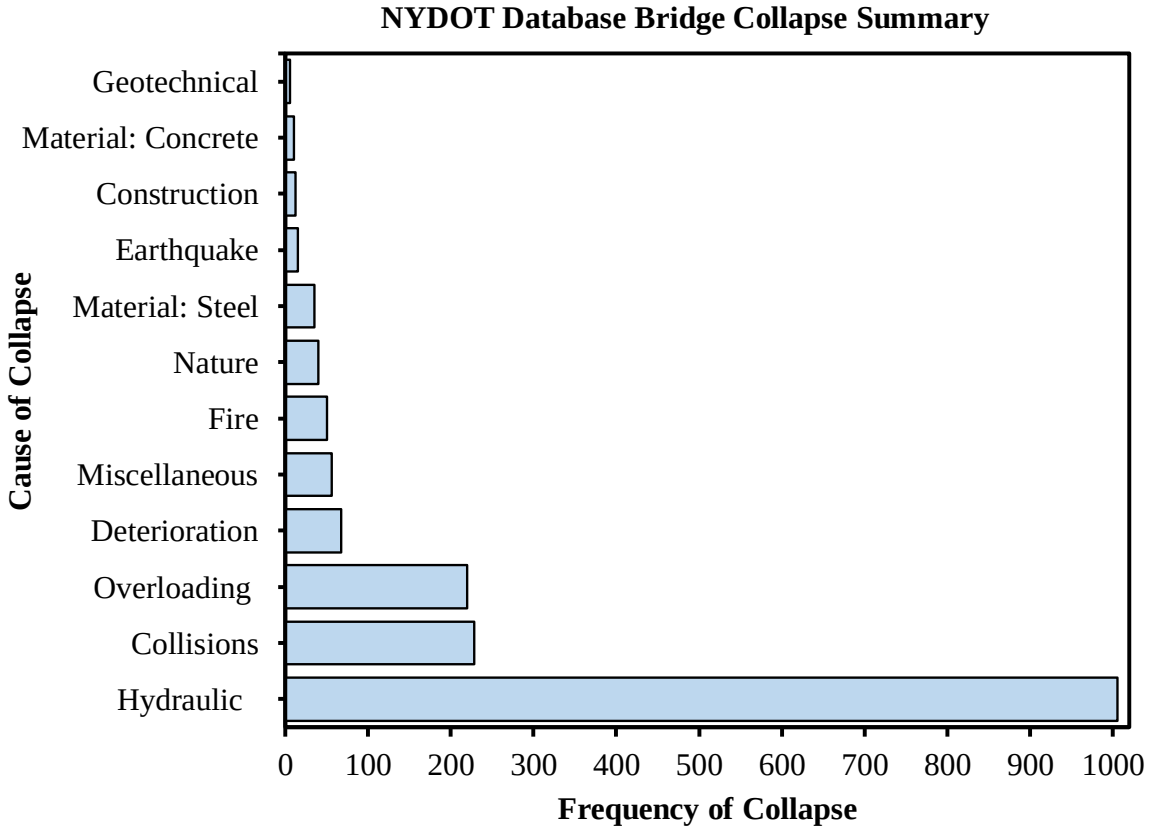

Figure 2-1: Bridge Collapse Bar Chart (Created from NYDOT Database)

The collapse cases due to fire were classified in the NYDOT survey according to the cause of bridge fire event as shown in Figure 2-1. Causes of bridge collapse due to fire are not well recorded since more than 70% of the causes are unknown as shown in Figure 2-2. However, collision is the reason for bridge fire events with the highest percentage among the known causes. According to NYDOT survey, fire caused loss of service or collapse of approximately one bridge per year (Wright et al., 2013).

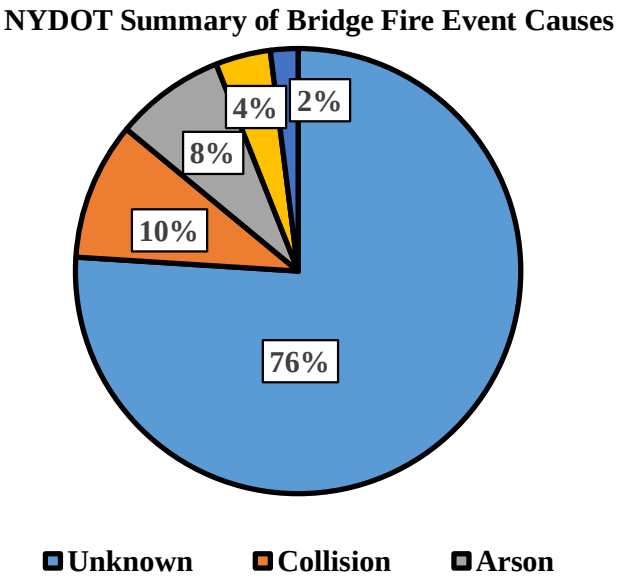

Figure 2-2: Cause of Bridge Fire (Created from NYDOT survey data)

The National Highway Traffic Administration Fatal Accident Reporting Service Encyclopedia (NHTSA-FARS) database is another source that could be used to extract bridge-fire event statistics. NHTSA-FARS database shows an average of 36 fatal incidents involving bridge and fire at the span of 14 years from 1994 to 2008 (Aziz et al., 2015). Figure 2-3 includes a pie-chart of NHTSA-FARS bridge collision summary. NHTSA-FARS database also includes fatal accidents that leads to bridge fire by point of impact summarized in Figure 2-4. As shown in the figure, almost half of the crashes causing bridge fire were at the bridge rails and parapets while the other

half were due to impact at the bridge piers or abutments. Crash events that occurred due to impact at the bridge piers caused a fire burning below the bridge, while the accidents with the impact point on bridge rails and parapets caused fire above the bridge. This is an indication that the probability of fire below or above the bridge is equally the same (Wright et al., 2013). The only limitation in NHTSA-FARS database is that it does not include accidents leading to bridge fire without fatalities, which is critical considering the fact that majority of the bridge fires do not involve fatality (Wright et al., 2013).

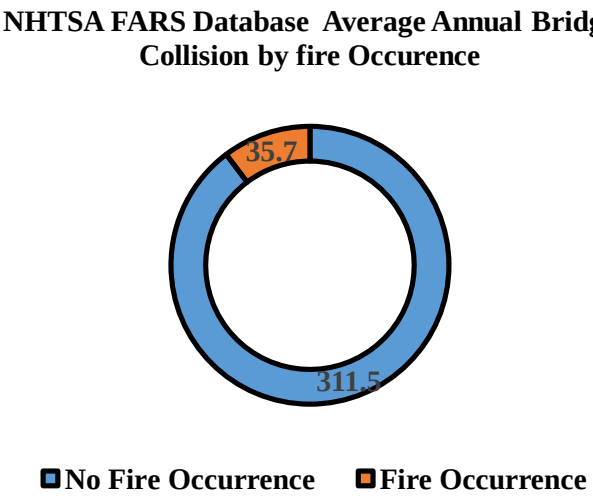

Figure 2-3: NHTSA-FARS collisions leading to bridge fire summary (Created from FARS database)

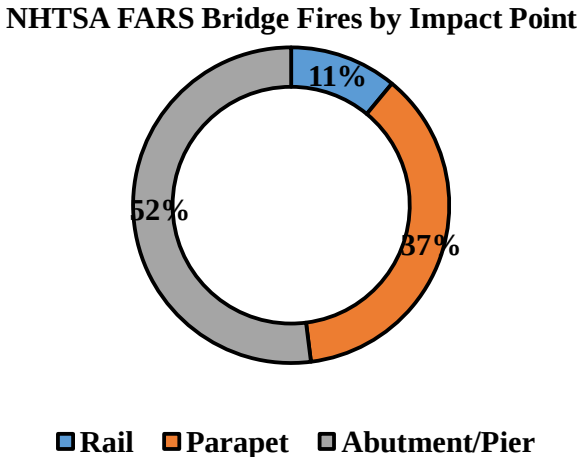

Figure 2-4: Bridge fire by Impact Point (Created from FARS database)

2.3 Recent Cases of Bridge Fire

On January 5, 2002, a gasoline tanker hit a bridge at the intersection of 65, 20 and 59 Interstate highway in Birmingham, Alabama. This accident caused fire on the bridge and as a result the bridge steel girders deflected up to 3 meters. Human casualty included life of the driver and the fire event on the bridge cost an approximately $100,000 in terms of daily traffic closure (FHWA, 2002). Figure 5 includes a picture of the bridge post fire event where a large deflection in one side of the bridge can be seen.

Figure 2-5: Bridge fire by Impact Point (FHWA, 2002)

A tanker transporting diesel fuel and gas was forced by an out of control car to hit an overpass on I-75 om Hazel Park, Michigan. The accident caused fire on the overpass up to temperature of 1260 °C and the overpass collapsed within 30 minutes of the fire initiation (Kodur et al. 20112).

A truck carrying 8600 gallons of gasoline overturned on MacArthur Maze I-80/880 in Oakland, California due to speeding on April 29, 2007 and caused the bridge to collapse after 22 minutes of fire exposure up to 1100 °C. The main cause of the bridge collapse was studied to be due to the girders large deformation and failure in the bolted connections (Kodur et al. 2012).

2.4 Current Building Fire Provisions Relevant to Bridges

All current codes include fire safety and protection guidelines to buildings. There are no codes safety requirement specifically pertaining to bridges. In order to study behavior of bridges and bridge structural members under fire event, building codes and fire loading criteria could be utilized to study bridges at elevated temperatures. This section covers current code provisions of building fire safety and protection as well as fire loading criterion in the current codes.

2.4.1 Fire safety and Protection Guidelines

The Building and Construction Code of National Fire Protection Association state that safety measures are developed in order to minimize human loss, damage of property and collapse of structures in a fire event (NFPA, 2012). In order to minimize impact of fire, building fire safety is managed through active and passive protection systems where active systems control fire through external devise such as sprinklers and passive systems are built within the structures to slow down fire event (Aziz, 2015). International Building Code (IBC, 2012) specifications provide fire resistance requirements for buildings' structural elements. Unlike buildings where fire safety is a vital design criterion, American Association of State Highway and Transportation Officials (AASHTO) has no fire safety and protection guidelines for bridge fire event. This could be due to the fact that fatality and loss of life is rarely recorded at a bridge fire event.

2.4.2 Fire Loading Relevant Provisions

Fire resistance is designed based on 50% of the materials ultimate capacity for buildings in the current codes where fire load is defined as the ratio of demand load on structural member to

strength of the structural member at ambient temperature (Aziz, 2015). American Society of Civil Engineers (ASCE) and Eurocode load factor combination for fire loading are

$$W_{fire}(ASCE) = 1.2\ DL + 0.5LL + 0.5OLL \quad (1)$$

$$W_{fire}(EUROCODE) = 1.0\ DL + 0.5LL + 0.5OLL \quad (2)$$

The time-temperature-curve for ASTM E119 and ISO 834 are respectively outlined by

$$T_{ASTM-E119}(℃) = 750\left(1 - e^{-3.7955\sqrt{t}}\right) + 170.41\sqrt{t} + T_0 \quad (3)$$

$$T_{ISO-834}(℃) = 345\log_{10}(8t + 1) + t_0 \quad (4)$$

Where t is time in hours and equation (3) and minutes in equation (4) and T_0 is the ambient temperature. There are other time-temperature curves such as hydrocarbon fire and external fire which represents more extreme fire. Figure x includes graphical representation of the above time-temperature curves.

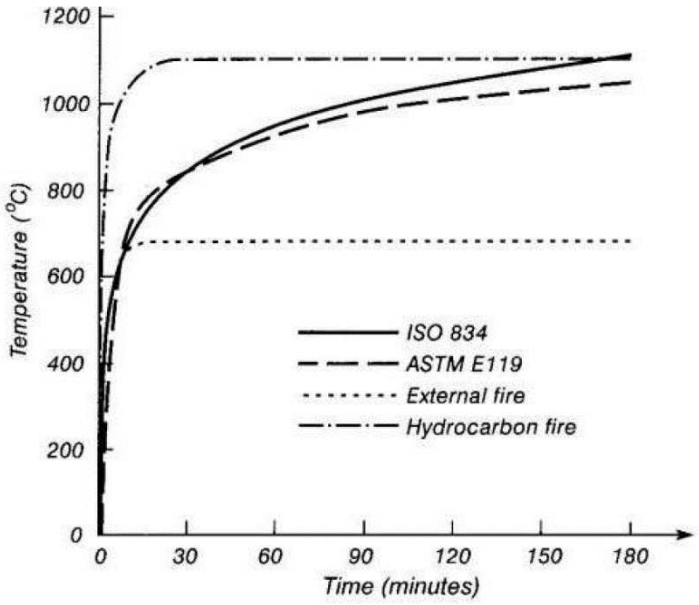

Figure 2-6: Standard time-temperature curves (McIntosh, 2011)

2.5 Previous Research

While there is lack of studies in the literature on the response of steel beam with pre-existing fatigue cracks under elevated temperature and under the combination of elevated temperature and loading, notwithstanding, a number of studies have been conducted on the response of steel beams with and without concrete slabs at elevated temperature but in the absence of pre-existing cracks. This section covers relevant previous experimental and numerical studies on response of bridge or bridge structural member subjected to fire event.

2.5.1 Experimental Studies

Aziz et al. (2015) performed a numerical and experimental studies on three steel bridge girders (hot-rolled and built up girder) supporting a reinforced concrete slab subjected ultimate structural loading and fire to study the performance of a typical bridge steel girder. The main variables in

this study was web slenderness and spacing of the girders. The results of the experimental study showed that failure under approximately 30 minutes of fire loading. The results also indicated that beam failure under fire condition was directly related to web slenderness. While specimens with web slenderness of approximately 50 failed in flexural yielding, the failure changed to web shear buckling in specimens with slenderness of the 100.

Fike and Kodur (2011) conducted an experimental test under ASTM E119 fire loading on a beam-slab composite to study the fire resistance of steel fiber reinforced concrete assembly, which has better fire resistance properties compared with steel alone. The experimental setup consisted of three W10X15 hot-rolled beams connected to two W12X16 steel girders and it was tested as an assembly. The fiber reinforced concrete slab was connected through shear studs. The three hot-rolled beams had no fire protection insulation. However, the two girders were insulated with 22 mm thick external fire protection in order to develop fire resistance rating of about two hours. Results of this experimental study indicated that fiber reinforced properties along with restraint conditions improved the fire resistance of the assembly. The study concluded that a composite steel-concrete assembly does not need external fire protection for the secondary beams and the concrete slab deck.

Wainman and Kirby (1989) completed an experimental study on composite steel beam-concrete slab specimens under standard ISO 834 fire exposure. The test included 21 non-composite specimens made out of 254X146X43 UB, 305X165X46 UB, 356X171X67 UB and 406X178X60 UB with no interaction between the slab and the steel beam and two fully composite steel-concrete beam made out of 254X146X43 UB. Two different grades of steel was used (Grade 43A and 50B/50D). Both standard ISO 834 fire loading and mechanical four-point bending load was

symmetrically applied along the span of the beam. No insulation layer for fire protection purpose was used in the composite assemblies. Failure was determined based on deflection limit of L/30, where L is the span length. Results of the experimental test showed that composite action, steel grade and load level significantly influences fire resistance of the steel beam composite with concrete slab. Additionally, composite action increased fire resistance from 25 minutes to 35 minutes under ISO 834 fire loading.

Bletzcacker (1996) performed an experimental research a composite steel beam with concrete subjected to ASTM E119 fire loading. The test included 12 composite beams made of W12X27 hot-rolled steel at span of 5.10m. In this experimental test, a cementitious insulation layer was sprayed on the beams and the slab for fire protection. The main focus of this study was on the effect of composite actions, axial and rotation restraints and connection types on the response of the composite beams at elevated temperature. The results of the experimental test showed that increasing the stiffness of the end boundary conditions beyond a certain level affects fire resistance of the composite beam. The results indicated that with increasing stiffness of the boundary conditions, local buckling became more evident in the flange and web of the W-shape section because as the restraints provided by the boundary conditions increased, the fire load developed further axial forces. It was also indicated that composite action improves fire resistance since composite action provides more restrains.

Vinmonsatit et al. (2007) conducted small-scale experimental tests on hot-rolled and built up steel beams tested at steady state elevated temperatures of 400 °C, 550 °C and 700 °C. The built up sections were five and were named as TG1 through TG5 and the hot-rolled sections were UC

152X152X23 and 203X203X52 kg/m. All the specimens spanned 1.66 m. The built up sections were 305 mm deep and web slenderness of 112, 152 and 203. While the depth of the built-up sections were not changed, slenderness of the specimens were varied by web thickness between 1.5 to 2.7 mm. This experimental study was performed to study shear buckling of the girders as well as development of plastic hinge in the flange plates. The test concluded that plate girders lose shear capacity under elevated temperature at a large scale and shear buckling decreases significantly at elevated temperatures.

2.5.2 Numerical Studies

Similar to previous experimental studies, the limited numerical studies of response of steel beam and bridge under elevated temperature does not cover steel beams with existing fatigue crack.

Cinitha et al. (2012) developed a Finite Element Model using ABAQUS to investigate behavior of steel beam at elevated temperature, which was tested as part of a thermal power plant. The finite element analysis was modeled to account for nonlinear effect of temperature and mechanical load. The numerical analysis included three different fire conditions namely two-sided, three-sided and four-sided fire exposure to temperatures of up to 800 °C. The fire condition was conducted to simulate steel beam within thermal power plan conditions. The results of the study indicated that steel beams with three-sided and four-sided elevated temperature conditions had higher maximum deflection. This study does not specify details regarding fire loading protocol.

Mendes et al. (2000) performed a numerical analysis to simulate the Vasco da Gama Bridge collapse due to a ship fire accident in Lisbon, Portugal. A 2-D bridge model was developed to investigate the temperature distribution from fire exposure and collapse time. The experiment used three different fire scenarios resulting in different temperature distribution, fuel type and burning

rate. The results of this numerical study showed that anchorage of the bridge broke within 20 to 30 minutes of fire exposure.

Dotreppe et al. (2006) completed a finite element simulation analysis to investigate collapse of the tied-arch Viregnis Bridge that spanned 136 m in Belgium on August 14, 1985 due to a fire event. Explosion of a gas pipe caused the fire at base footing of the bridge. Using SAFI software program, beam element was used to develop the nonlinear finite element model which included steel girders, concrete slab, trusses and arches. The results of the experiment that included failure modes agreed with the data collected from the field after the bridge collapse.

Bennetts and Moinuddin (2009) performed a numerical study to investigate the overall behavior and vulnerability of bridges exposed to fire. The study included a suspension under three different fire conditions on the bridge. Suspension cables for varied with insulated for fire protection and no insulation. The objective of this experiment was to determine time to failure for the cables and towers. Results of the analysis concluded cables with no insulation cover has 10 minutes less time to failure than the insulated ones under extreme loading.

2.6 Temperature-Dependent Steel Properties

Temperature-dependent thermal, mechanical and deformational properties of steel play a crucial role in performance of structural steel. Use of steel in structures is favorable due to its relatively high stiffness and strength, however, stiffness and strength of steel decreases under elevated temperature application. Steel temperature-dependent properties are developed experimentally,

therefore, constitutive relationships of steel under elevated temperature developed by different codes have variations. (Kodur and Harmathy, 2015).

Mechanical properties of steel as a function of temperature govern stiffness and strength degradation and increase in fracture toughness of structural steel. Thermal properties of steel controls temperature distribution and transfer in a steel structure.

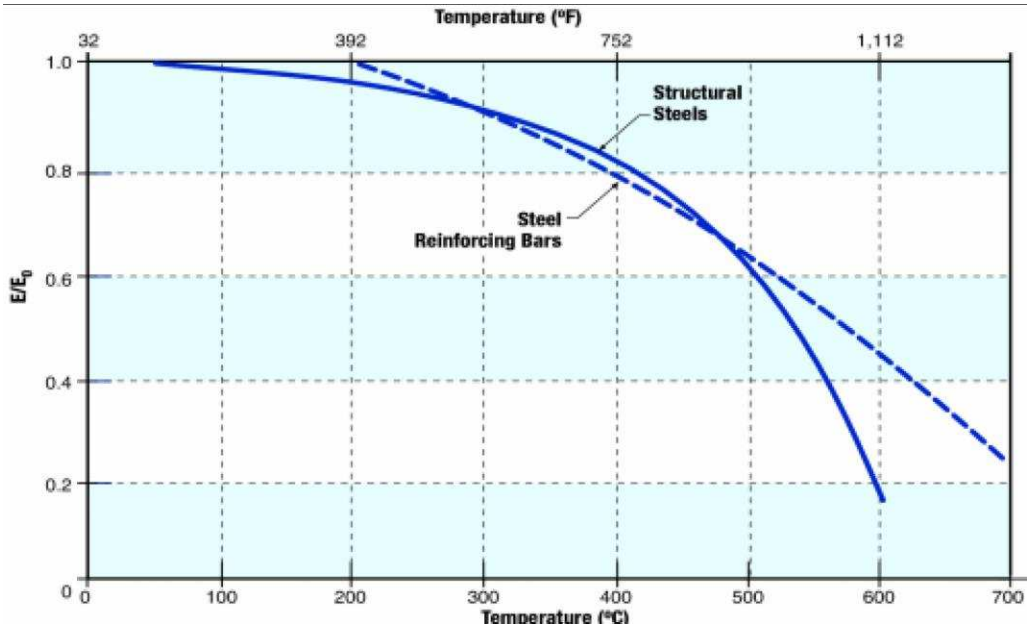

Figure 2-7: Normalized modulus of elasticity of steel as a function of temperature (Bradt, 2011)

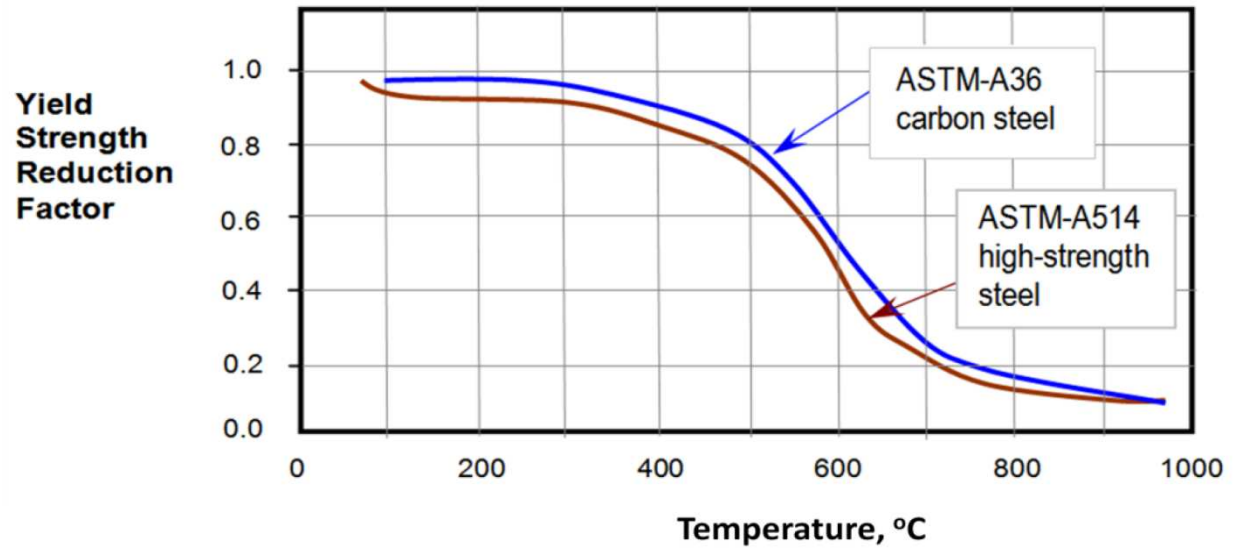

Figure 2-8: Normalized yield strength of steel as a function of temperature (Bradt, 2011)

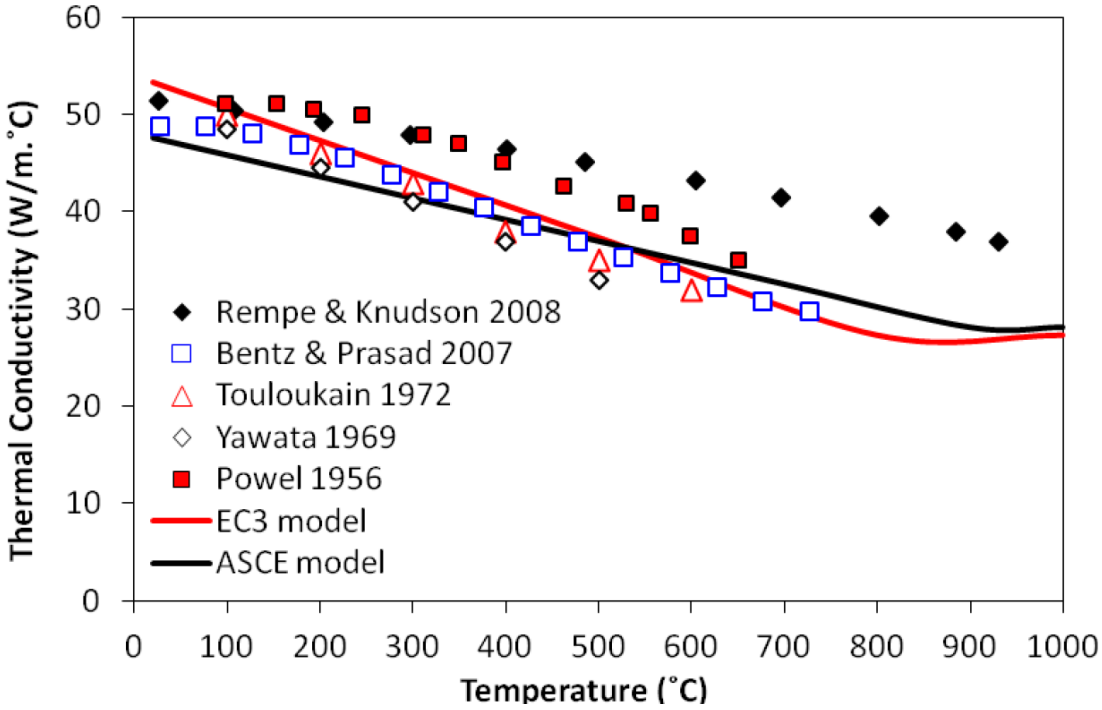

Figure 2-9: Thermal conductivity of steel as a function of temperature (Aziz, 2015)

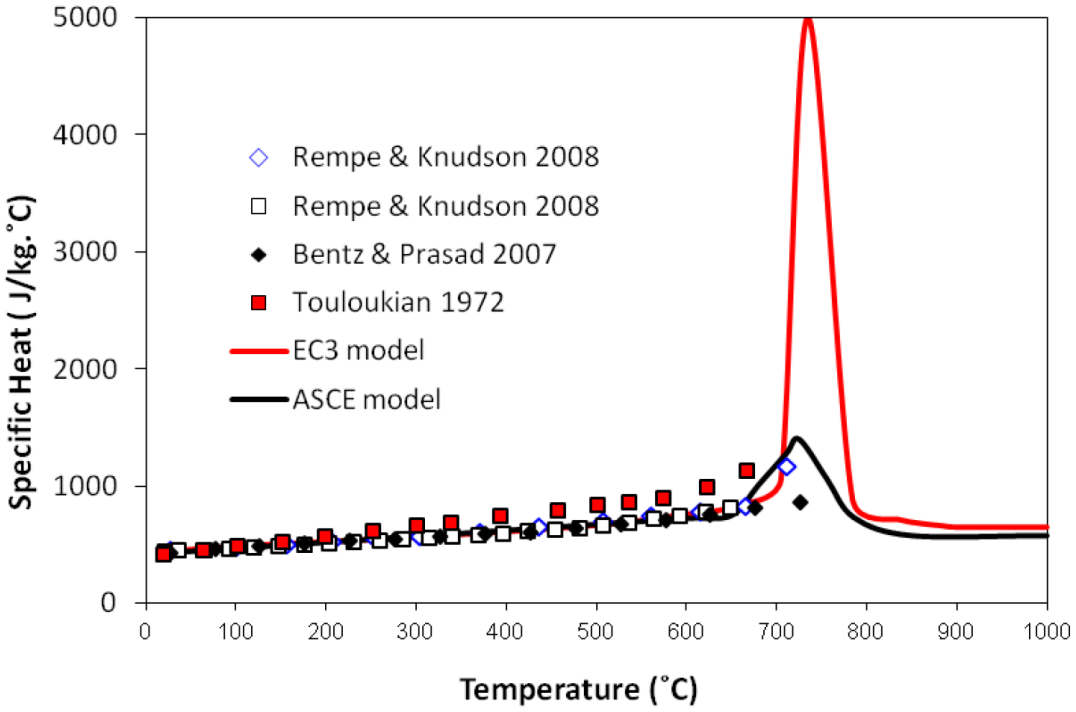

Figure 2-10: Specific heat of steel as a function of temperature (Aziz, 2015)

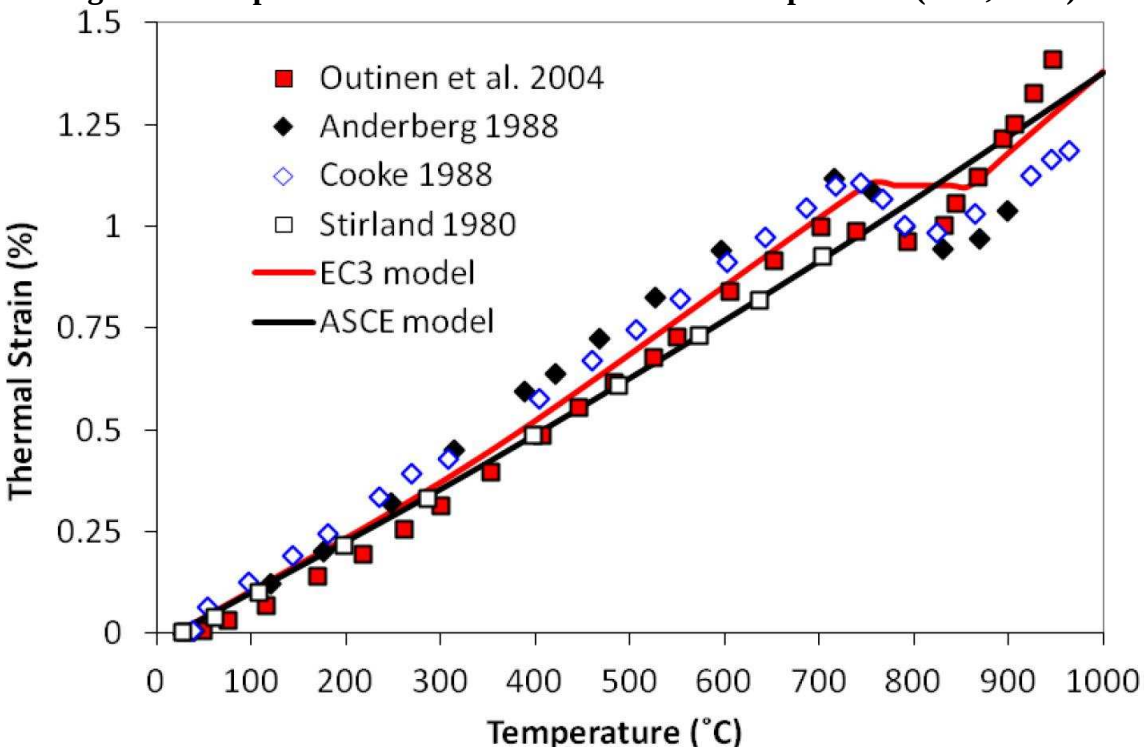

Figure 2-11: Thermal strain of steel as function of temperature (Aziz, 2015)

2.7 Fracture Mechanics

Fracture Mechanics focuses on rapture in loaded solid elements due to crack initiation and crack propagation. It was developed because classical maximum stress failure criterions were not adequate to address failure of loaded solids under low applied stresses due to existence of cracks and flaws in solids (Sun & Jin, 2012). Unlike classical maximum stress criterion, failure in fracture mechanics is addressed based on interaction between stress, material flaw such as cracks and material constants such as fracture toughness (Sun & Jin, 2012). In fracture mechanics, focus is on stress and displacement distributions around the crack tip rather than the magnitude of stress. Figure 2-12 shows progression of stress concentration around a solid plate with edge crack loaded in a uniaxial fashion. As seen in the figure, geometric discontinuity due to existing flaw or crack forces stress flow near the crack tip, which results in larger stress concentration near the crack compared with the rest of the region in the plate under the applied uniaxial load.

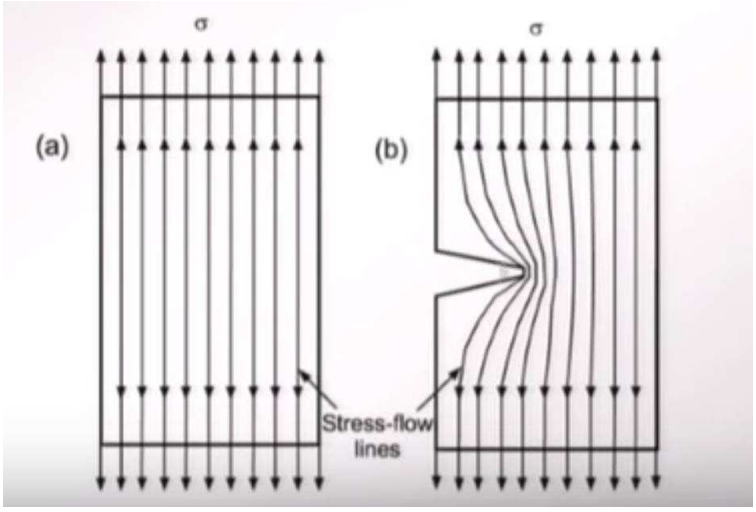

Figure 2-12: Concentration of stress around a crack tip due to geometric discontinuity (NPTEL – Fracture Mechanics Lectures)

Cracks in solid material such as steel has an upper and a lower face and when a cracked solid is loaded, these two surfaces move relative to each other. This phenomenon occurs in three different modes, Mode I, Mode II and Mode III. Figure 2-13 contains a schematic of the three fracture modes under elastic stress. As shown in the figure in 3D Cartesian Coordinate, two surfaces of the crack move away in the y-direction symmetrically in Mode I which is also called opening mode under tensile load. The surfaces slide relative to each other in Mode II also called in plane shearing mode and the surfaces move away from each other in z-direction in Mode III also called out of plane shearing mode or a tearing mode. The most common fracture failures are under Mode I.

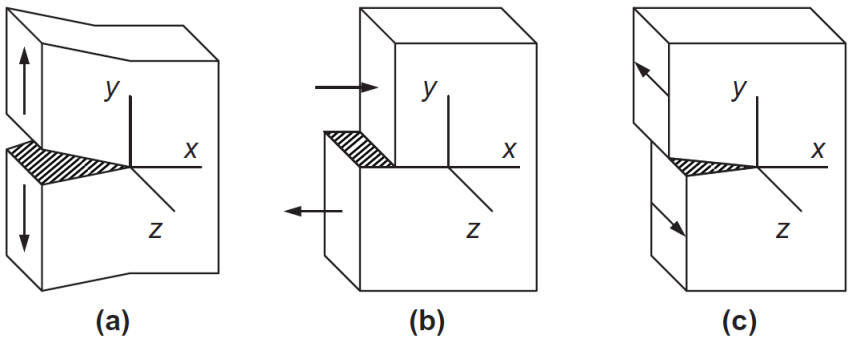

Figure 2-13: Schematics of Fracture mode. (a) Mode I – opening mode, (b) Mode II – sliding mode and (c) Mode III – tearing mode (Sun & Jin 2012)

Failure criteria in fracture mechanics are approached through either Linear Elastic Fracture Mechanics (LEFM) or Elasto Plastic Fracture Mechanics (EPFM). LEFM is developed based on the assumption that the stress field around the crack tip is within the elastic limit (limited plasticity) under service load, while EPFM accounts for large plasticity in the stress field around the crack tip under ultimate loads. LEFM is used to analyze brittle fracture where crack opens rapidly with minimum plastic deformation in an unstable manner, while EPFM is used to determine fracture of

ductile material, where crack opens stably and there is significant amount of plastic deformation around the crack surface (Sun & Jin, 2012).

2.7.1 Linear Elastic Fracture Mechanics (LEFM)

In LEFM, a sharp crack tip that does not go through any plastic deformaiton at the crack tip is assumed. The applied load is also assumed to be service load which approximately about 50% - 60% of the yield strength of the material at is peak value. Figure 8 shows an idealized crack tip and applied load versus displacement under LEFM conditions.

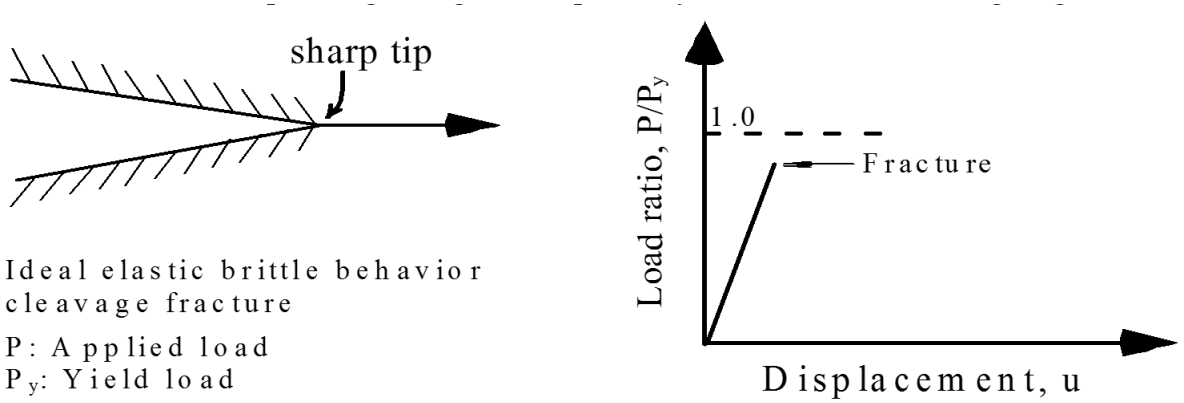

Figure 2-14: Idealized crack tip in LEFM under applied service load (Sun & Jin 2012)

In LEFM, failure criteria are either based on local stress field around the crack tip or global energy balance. The approach through crack tip stress field involves K, the stress intensity factor. K is a fracture mechanics parameter which defines the resistance of the material with respect to loading rate at the crack tip. Global energy balance approach utilizes the conservation of energy to establish fracture design criteria and limit states (Sun & Jin, 2012).

2.7.1.1 Stress Intensity Factor K

The stress intensity factor, K, valid for a small region around the crack tip with sufficiently small plastic deformation, is a function of crack length, crack tip nominal stress, and crack geometry. It is described as by

$$K = F_c F_s F_w F_g \sigma \sqrt{\pi a} \quad (5)$$

Where,

$K = Stress\ intensity\ factor$

$F_c = Shape\ factor\ of\ the\ crack$

$F_s = Surface\ factor\ of\ the\ crack$

$F_w = Finite\ width\ factor$

$F_g = Stress\ non-uniformity\ factor$

$\sigma = Normal\ nominal\ stress$

$a = half\ crack\ length$

Figure 2-15 includes a sketch of a typical edge crack of a tension plate under normal stress. To determine failure criteria in LEFM, stress intensity factor K is checked against K_{IC}, fracture toughness which a constant determined experimentally. George R Irwin (1975) proposed that fracture failure takes place or crack in a member loaded in tension grows in an unstable manner when

$$K > K_{IC} \quad (6)$$

From the relationship between the stress intensity factor, K, and fracture toughness, K_{IC}, critical crack length can be determined at which fracture occurs under LEFM (Sun & Jin, 2012).

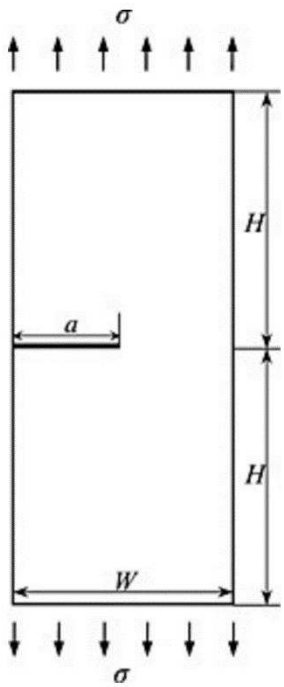

Figure 2-15: Edge Crack in plate under normal stress (An et. al, 2014)

There are different experimental methods, which can be used to determined fracture toughness of the materials. Charpy V-Notch Test conducted according to ASTM E. 2. (2007) is a very common method to determine fracture toughness of steel. Charpy V-Notch is an impact test through which the absorbed energy of a material during fracture is determined. Fracture toughness of steel is temperature and geometric-scale dependent. Figure 11 shows experimental data obtained to determine fracture toughness of ferritic steel under elevated temperature. This figure is critical with respect to this study since one of the objectives of this experimental program is to evaluate

competition of steel's fracture toughness improvement at elevated temperature versus degradation of stiffness and strength of steel at elevated temperature.

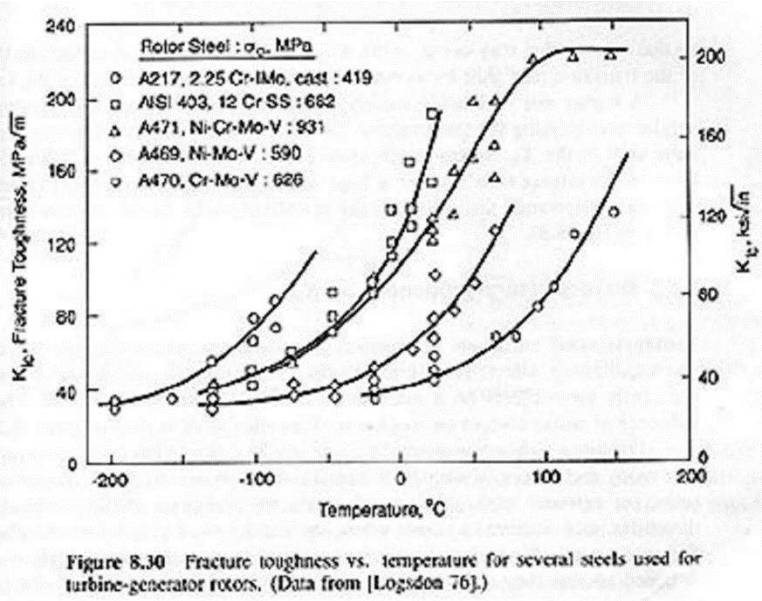

Figure 8.30 Fracture toughness vs. temperature for several steels used for turbine-generator rotors. (Data from [Logsdon 76].)

Figure 2-16: Fracture toughness of steel as function of temperature (Dowling, 1993)

2.7.1.2 Energy Release Rate G

Global energy balance is another approach to evaluate failure criteria in LEFM. In this method, total potential energy of a cracked element under tensile load and its virtual crack growth is calculated. A schematic of crack tip with the virtual crack is shown in Figure 9. Assuming a two-dimensional plate, a new dimensionless function denoted as $\pi = \pi(a)$ is introduced which is defined as energy per unit thickness of the cracked plate. Based on this function, the potential energy decreases with increasing crack length and the released energy would be absorbed in the new cracked body. Irwin introduced another fracture parameter G, the energy released defined as

$$G = -\frac{d\pi}{da} \tag{7}$$

Where G is compared against G_{IC} which is a new material constant used to measure materials resistant to fracture. If the energy release rate G is greater than G_{IC}, the loaded member will fracture.

The stress intensity factor and energy release rate set fracture mechanic fracture criteria apart from classical failure criteria because these approaches make fracture mechanics not dependent on strength of material but on crack size, material geometry and stress around the crack.

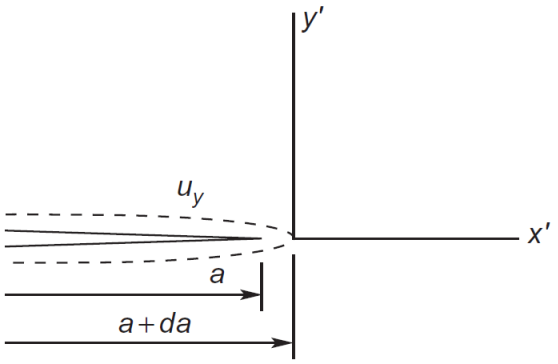

Figure 2-17: Virtual crack extension considered in global energy balance approach (Sun & Jin, 2012).

2.7.2 Elasto Plastic Fracture Mechanics (EPFM)

EPFM was developed because both stress intensity factor and energy release rate approach works only in Linear Elastic Fracture Mechanics (LEFM), where the cracked element is assumed to be under linear elastic stress range and non-linear effects such as large plastic deformations are ignored. Several fracture parameters have been developed to estimate fracture of steel and other

materials loaded up to large plastic deformation taking into account the nonlinear affects. These parameters include J-integral, crap tip opening displacement (CTOD) and crack tip opening angle (CTOA). Only CTOD and J-integral will be discussed which is relevant to the experimental program of this study.

EPFM considers the plastic deformation and other nonlinear effects around the crack tip during fracture. The crack tip is not an ideal sharp tip anymore but rather a realistic crack with blunt tip. Also, the applied load is not limited to yield load and the non-linear portion of the load-displacement curve is taken into account in EPFM. Figure 13 describes the crack tip blunting under large plastic deformation as well as non-linear applied load beyond elastic limit. Two parameters that are generally used in EPFM are Crack Tip Opening Displacement (CTOD) and J-integral which give estimate of material's fracture toughness independent of the cracked material geometric configuration.

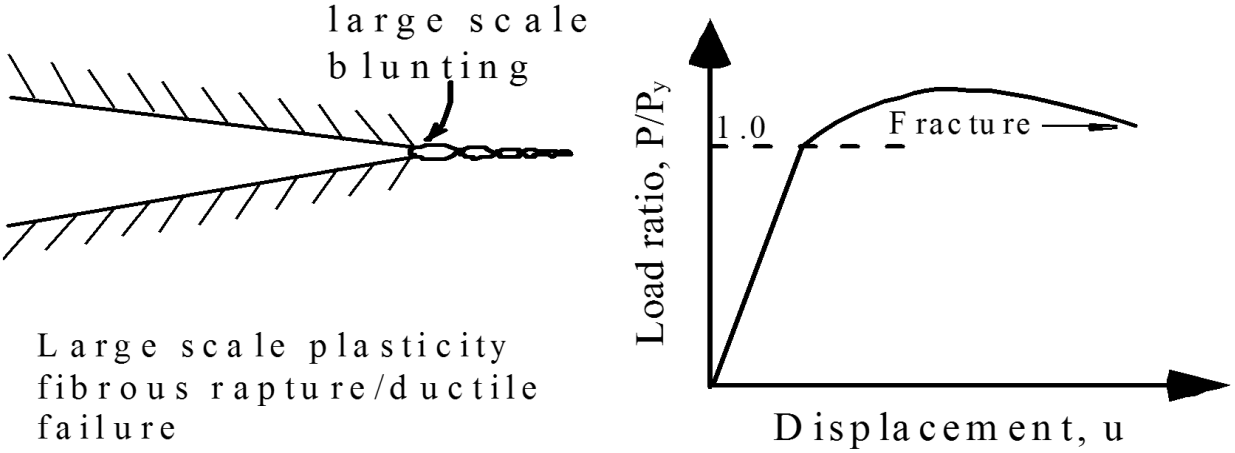

Figure 2-18: EPFM crack tip with large scale blunting and non-linear load-displacement curve (Sun & Jin, 2012)

2.7.2.1 Crack Tip Opening Displacement

Based on CTOD method crack initiation occurs under Mode I when the following condition is met (Sun & Jin, 2012):

$$\delta = \delta_c \tag{8}$$

Where δ is the CTOD shown in Figure 14 and three-point bending test is used to experimentally determine δ_c.

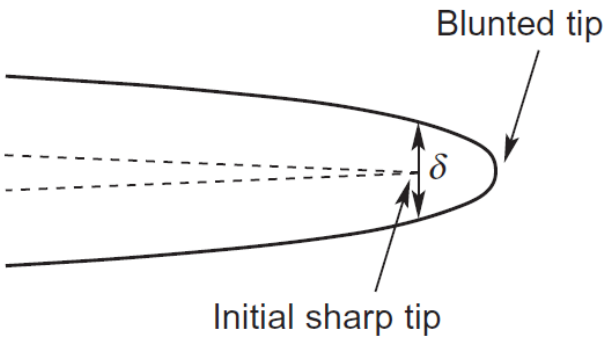

Figure 2-19: Definition of CTOD with original crack position (Sun & Jin, 2012)

According to the models developed by Irwin and Dugdale, general CTOD equation was derived as

$$\delta = \beta * \left(\frac{K^2}{\sigma_Y}\right) \tag{9}$$

Where β equals to 1 based on Dugale model and 4/π according to Irwin's model. Looking at the relationship between stress intensity factor K and CTOD δ, it can be concluded that CTOD method is the same as stress intensity factor for small scale yielding where plastic deformation is minimum.

According to Dugdale model, CTODF in a plate with crack under uniform normal stress σ, is defined as

$$\delta = -\left(\frac{8a\sigma_Y}{\pi E}\right)\ln\left(cos\left(\frac{\pi\sigma}{2\sigma_Y}\right)\right) \tag{10}$$

Using the above equations, critical fracture criteria is defined by

$$\delta_c = -\left(\frac{8a\sigma_Y}{\pi E}\right)\ln\left(cos\left(\frac{\pi\sigma}{2\sigma_Y}\right)\right) \tag{11}$$

A stress corresponding to failure criteria can also be determined as

$$\sigma_f = \left(\frac{2}{\pi}\right) * \sigma_y * \cos^{-1}[\exp(-(\frac{\pi E\delta_c}{8a\sigma_Y}))] \tag{12}$$

Similarly, critical crack length can also be determined as

$$2a = \frac{-\left(\frac{\pi E\delta_c}{4\sigma_Y}\right)}{\ln\left(cos\left(\frac{\pi\sigma}{2\sigma_Y}\right)\right)} \tag{13}$$

2.7.2.2 J-Integral

Developed by Rice (1968), J-integral was proposed as an alternative approach to determine failure criteria in EPFM defined by:

$$\oint \left(\mathrm{Wdy\text{-}T_i} \frac{\partial u_i}{\partial x} ds \right) = J \tag{14}$$

Where the line integral is an arbitrary curve around the crack tip as shown in Figure 2-20, W is strain energy per unit volume and T_i is the components of the traction vector defined respectively by

$$W = \int \sigma_{ij} d\varepsilon_{ij} \tag{15}$$

$$T = [\tau_{ij}]\{n\} \tag{16}$$

Where u_i is the displacement vector components, ds is the incremental length of the arbitrary curve, and x, y are the Cartesian coordinates with y taken perpendicular to crack line.

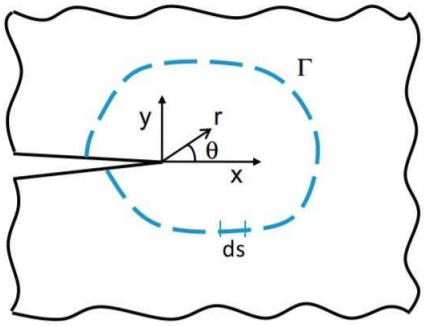

Figure 2-20:Arbitrary line integral contour taken around the crack tip for definition of J-integral (Sun & Jin, 2012)

Taking a closed contour, the J-integral will be equal to zero. The integral path independently goes from one face of the crack to the other face closing the counter with assumption of the crack face

not being loaded. It is customary to consider a path where calculating the closed contour integral is easy and convenient. Similar to LEFM, J is compared against J_{IC}, material parameter, to determine fracture in nonlinear fracture mechanics where large plastic deformation is considered around the crack tip.

There have been numerous studies to estimate J-Integral based fracture criterion ($J = J_{IC}$) (Sun & Jin, 2012). The most prominent approach is determining J-integral from load-displacement curve data obtained experimentally (Zhu et al., 2012). The estimated of J-integral from load-displacement curve under three-point pure bending is given by:

$$J = \frac{2A_{tot}}{Bb} \tag{17}$$

Where $b = W - a$, W is the beam specimen depth, B is the thickness of the material and A_{tot} is the total area under the load-displacement curve representing the total absorbed ductility energy. Using the equation (17), critical value of J can be calculated from the load-displacement curve of a beam under three-point bending.

Chapter 3 - Experimental Program

3.1 Introduction

The experimental program is developed with the goal of evaluating the failure mode and fracture characteristics of a cracked steel girder under mechanical and fire loading. For this purpose, the test setup was designed to accommodate both mechanical and thermal loading and an instrumentation plan was developed in order to collect the relevant data. The specimens were subjected to elevated temperature followed by monotonic loading in a step by step manner in order to reliably capture the data.

This chapter summarizes the test matrix and includes details of the test frame design for both mechanical and applied elevated temperatures loads, the instrumentation plan for both mechanical loading and temperatures distribution, insulation approach to protect the equipment and achieve the required thermal distribution, and the testing protocol.

3.2 Specimen Details & Test Matrix

Four beam specimens were prepared from W8X24 hot-rolled A36 steel. Each specimen was cut to 3708.50 mm; however, the true span of each beam specimen was 2997 mm to accommodate the extra length for roller end boundary conditions. Edge crack of 0.50 mm was introduced at mid-span of each specimen using electrical hand saw through the flange thickness and on both sides of the bottom flange. The specimen preparation process is shown in Figures 3-1 and 3-2. During the cutting process, extra attention was given to minimize human error and to ensure crack configuration is uniform across all the specimens. This configuration of pre-existing crack in the bottom flange was selected in order simulate the presence of a crack in a typical beam resulting

from welding for example a shelf plate attachment to the flange, which could cause a fatigue crack to develop if not properly designed. In addition, since the goal of this study is to evaluate the response of the cracked beam under ambient and elevated temperature, it is irrelevant as where the crack would be initially located. For example, if the crack was introduced in the web instead, a larger load would have been required but the crack would still have propagated up and down the web and into the flange. The total crack length, being an edge crack and defined with length *a* equaled to 76.20 mm. This included all the flange width up to the thickness of the web from both sides. Figure 3-3(a) shows cross section of a W8x24 beam specimen with the introduced crack at the bottom flange, and Figure 3-3(b) shows a photo of the crack.

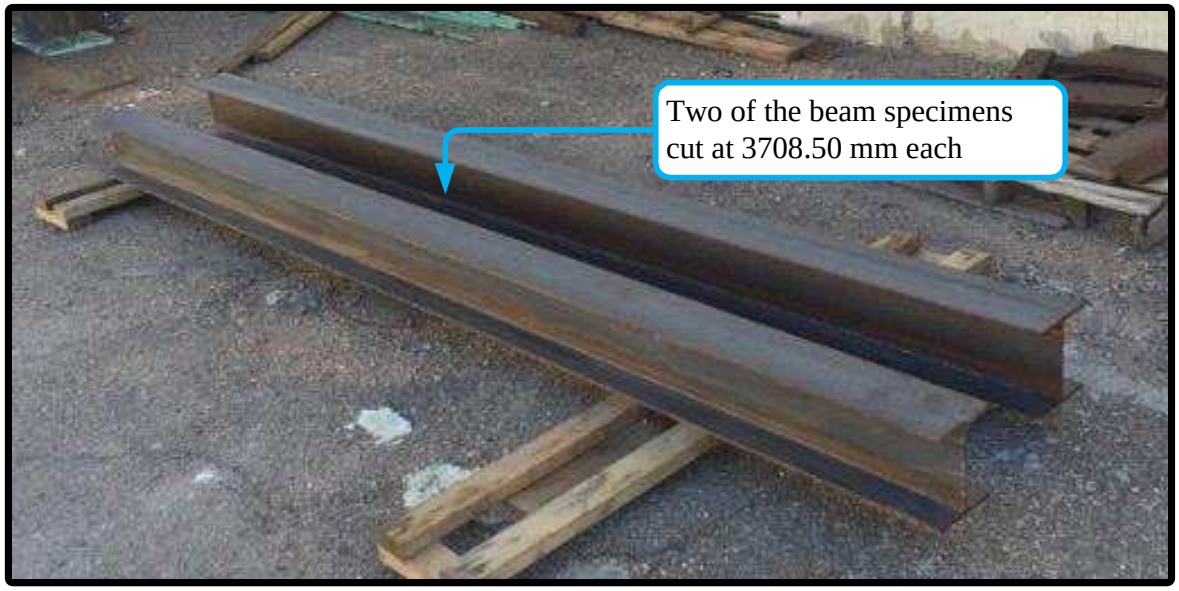

Figure 3-1: Beam specimens cut at the designated spans

Figure 3-2: Electric hand saw using in cutting the pre-existing bottom flange cracks

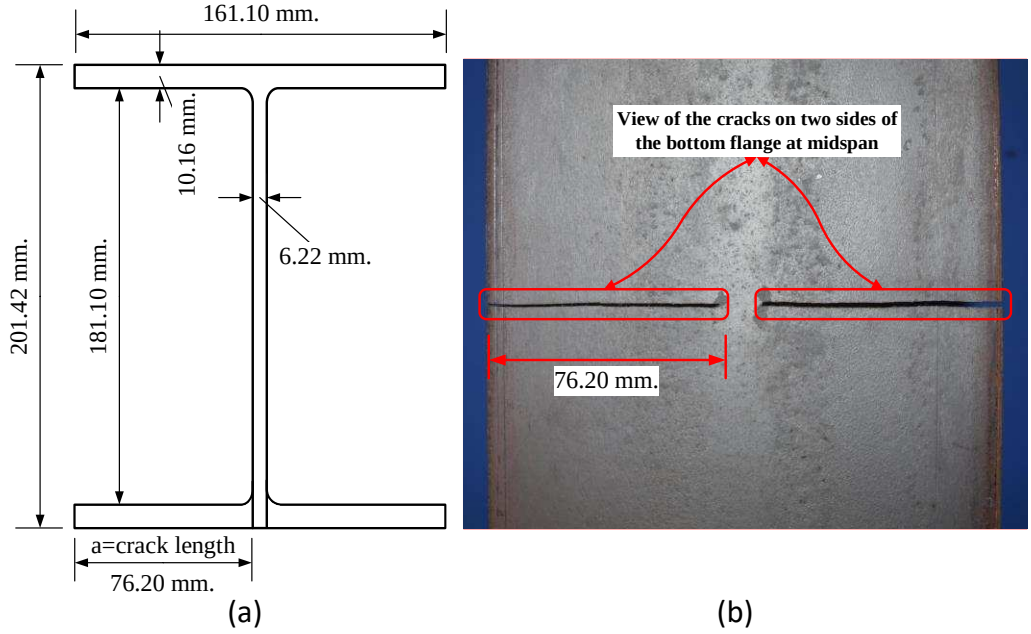

Figure 3-3: (a) cracked cross section dimension of the specimens (b) cracked bottom flange view

The four specimens were subjected to temperatures of up to 23.4 °C (ambient), 200 °C, 400 °C and 600 °C, respectively in a non-uniform fashion across and along the beam. From here on these are referred to specimens 1-4 corresponding to the limiting temperatures. Once out the temperatures reached steady state, specimens were subjected to mechanical loading at mid-section until failure. The project test matrix is outlined in Table 3-1. Thermal application and mechanical loading are discussed later in the chapter.

Table 3-1: Test Matrix

Specimen	Maximum Temperature	
1	23.4 ° C (Ambient)	74.3 °F (Ambient)
2	200° C	392 °F
3	400° C	752 °F
4	600° C	1112 °F

3.3 Test Setup

The test setup was designed to accommodate both mechanical and thermal loadings. Front view and top view of the test setup is shown in Figures 3-4 and 3-5, respectively. A 110-kip hydraulic actuator was utilized for mechanical loading. The test frame consisted of a top frame that was used to mount the actuator at mid span and a bottom lateral frame that provided roller supports to the tested beams. Both frames were designed using the AISC-360 Steel Construction Specifications (2010). As seen in the figures, roller supports were provided to replicate simply supported boundary condition and allowing unrestrained rotation under mechanical loading and free expansion of the beam under thermal loading. A lateral bracing system was bolted to the bottom

frame in order to avoid lateral torsional buckling of the specimen before it reaches its ultimate strength. These lateral bracings can also be seen in Figure 3-6.

In order to avoid top flange local buckling of the beam, 50.80 mm thick steel plate was clamped to the top flange which can be seen in Figure 3-4, 3-5, and 3-6. The applied point load was transferred from the actuator to the beam using a short column stub as shown in schematically in Figure 3-4.

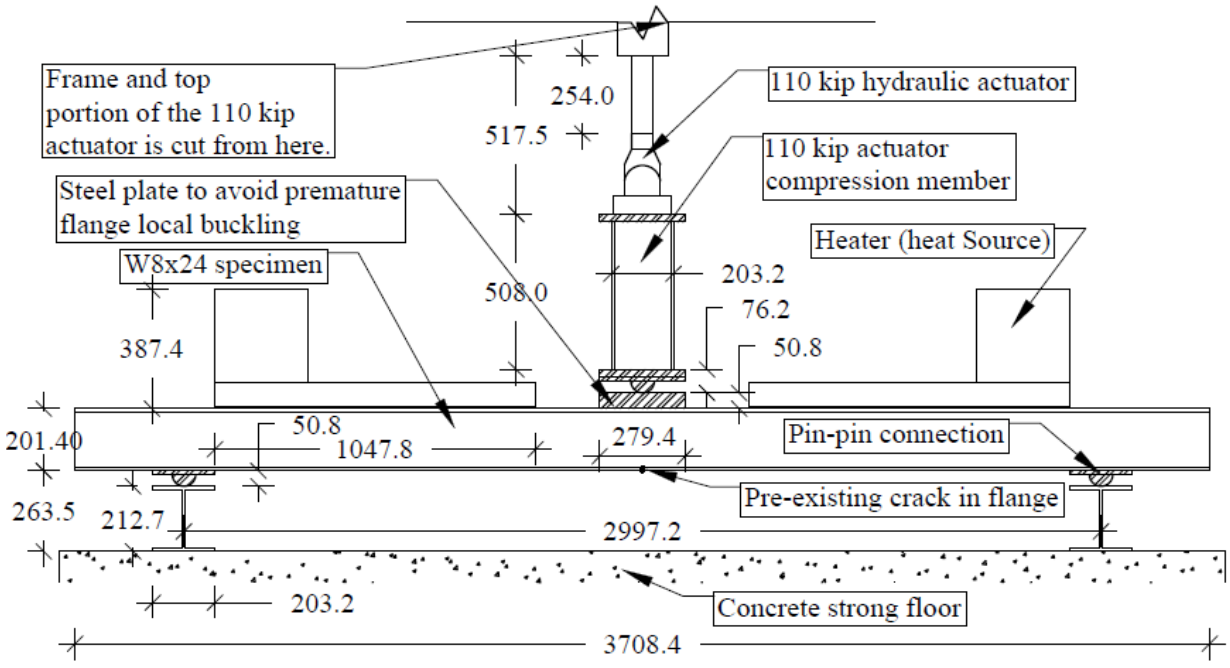

Figure 3-4: Experimental Test Setup Drawing

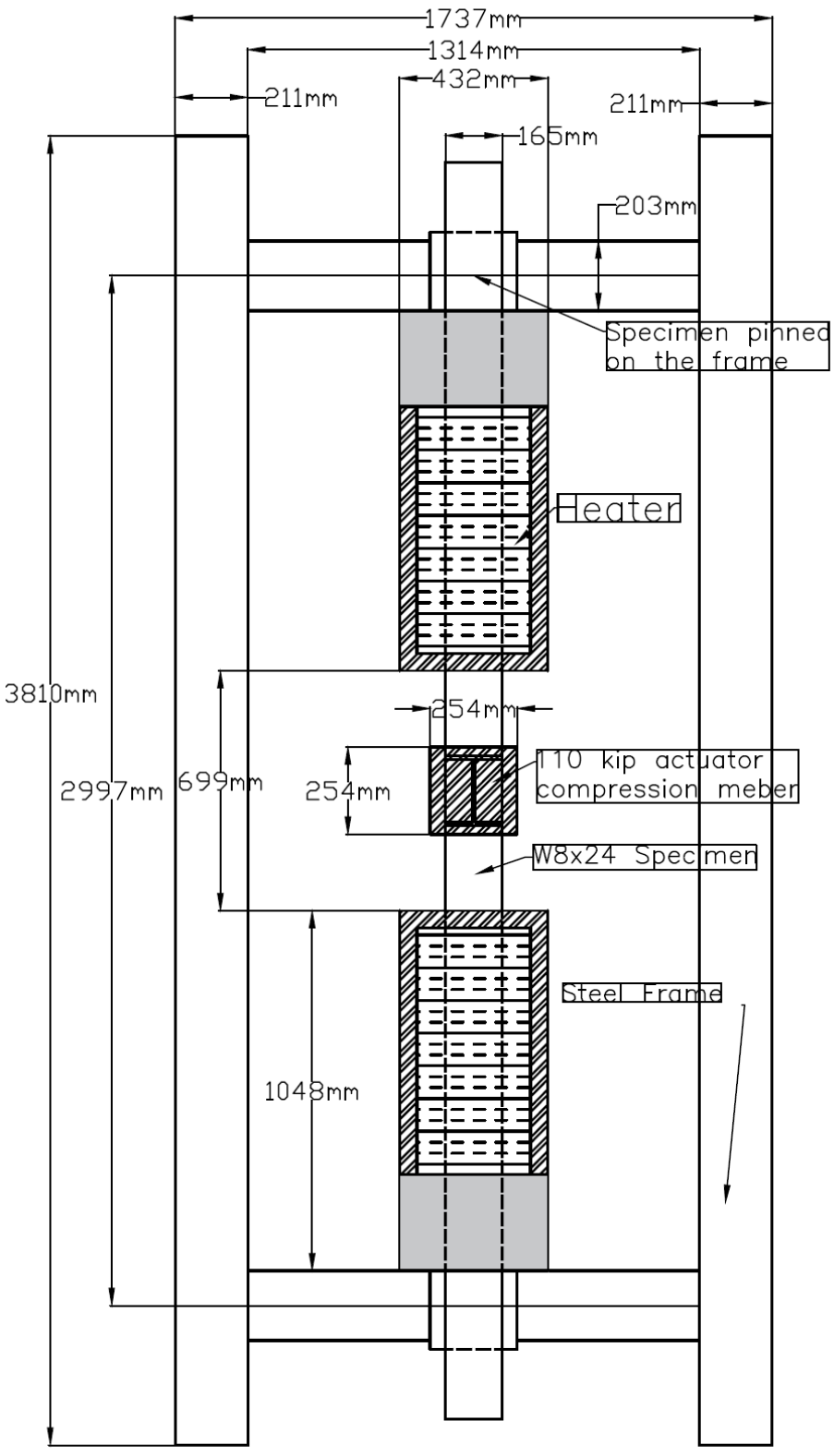

Figure 3-5: Experimental test setup top view

The second component of the test setup is temperature distribution application which includes a pair of ceramic radiative heaters, heaters' frames and ceramic fiber glass insulation chamber. The ceramic radiative heaters were placed on top of the beam for temperature distribution from the top flange across and along the beam and an insulation chamber made from ceramic fiber glass is provided around the beam in order to confine the avoid the heat loss. Photos of the test setup with and without insulation are included in Figure 3-6 and Figures 3-7, respectively. The ceramic radiative heaters were supported vertically through placing their edges on two small heaters' frames, which are shown in Figure 3-7. Figure 3- 8 shows the ceramic heaters front view, which was placed facing the top flange of the beam specimens to provide heat transfer through conduction. Figure 3-9 includes top view of a finished test setup.

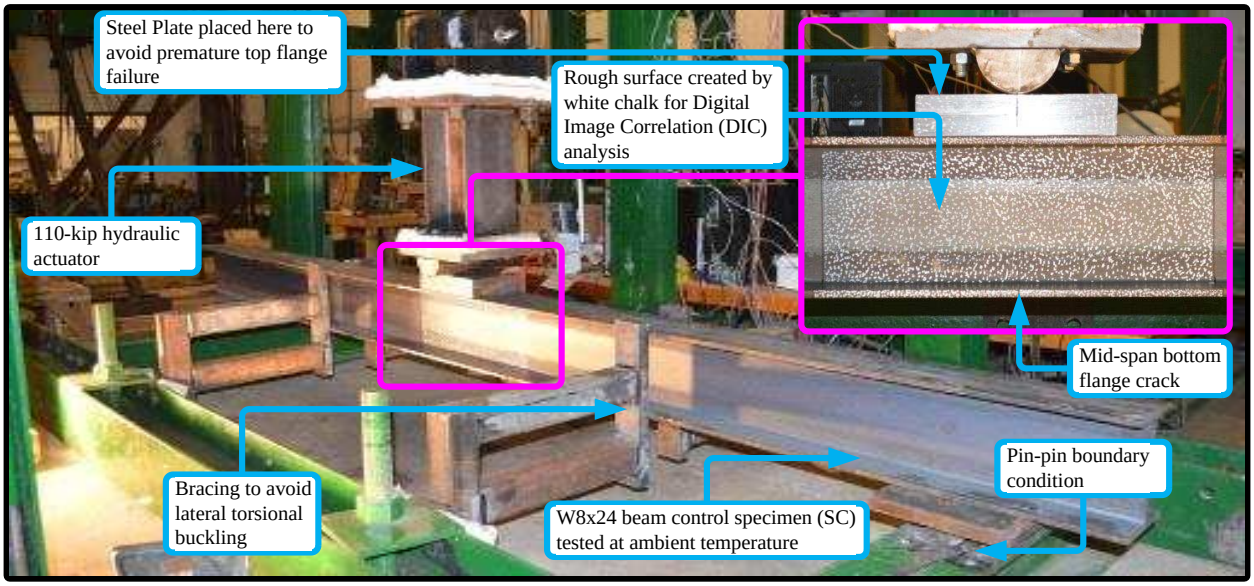

Figure 3-6: Experimental Setup View without the insulation chamber

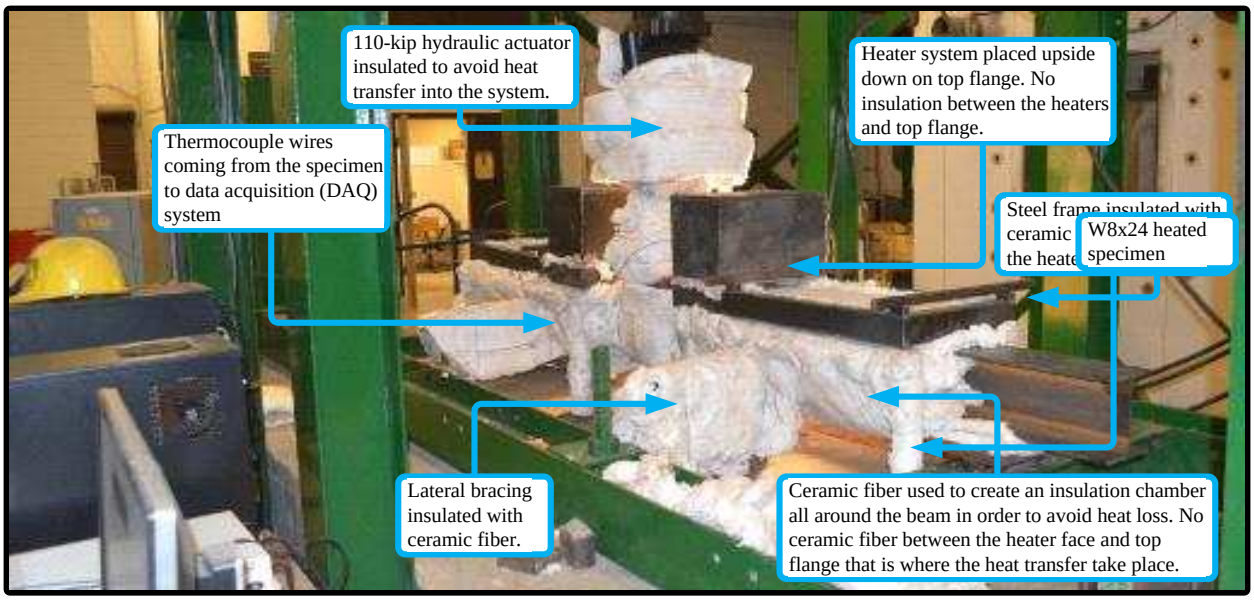

Figure 3-7: Experimental Test Setup View with insulation chamber and insulation works

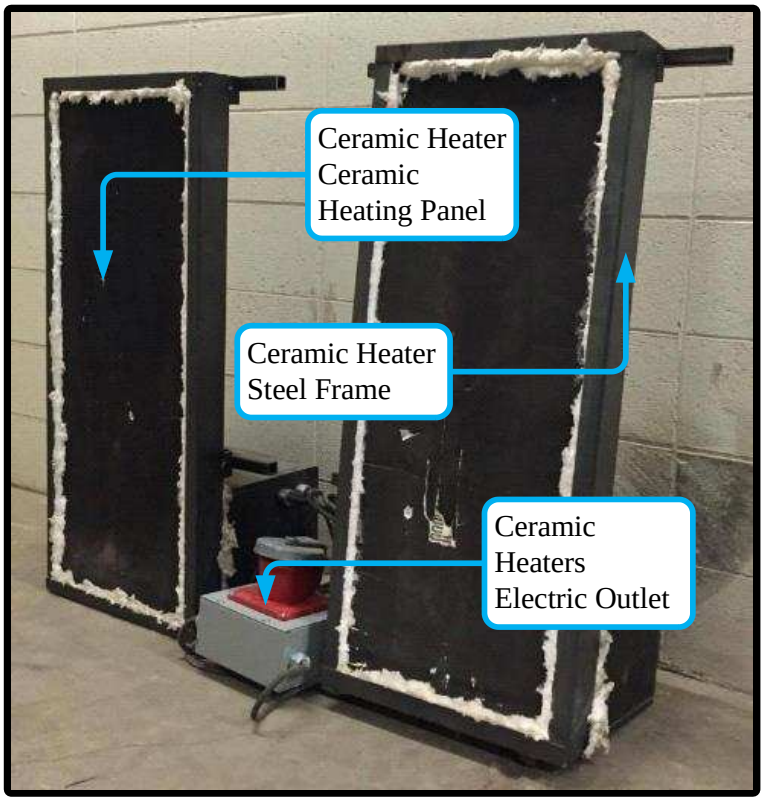

Figure 3-8: Pair of radiative ceramic heaters for heat application through conduction

Figure 3-9: Top view of finished test setup

3.4 Instrumentation Plan and Testing Protocol

The instrumentation plan was developed to collect mechanical and thermal test data. The mechanical data comprised of load and displacement data of the actuator which were collected using a Linear Variable Differential Transducer (LVDT) and a load cell mounted to the actuator. In addition, mechanical data pertaining to the specimen were obtained through post-processing still images, which were collected using a high-resolution camera. The thermal data comprised of temperature readings at various locations on the specimen, which were collected using

thermocouples placed at various locations. A Proportional–Integral–Derivative (PID) controller was used to execute the loading protocol associated with the hydraulic actuator and a Proportional–Integral–Derivative Filter (PIDF) controller was used for the temperature protocol. Specifically, a 407 PID Controller was used to execute the mechanical loading protocol and an EZ-ZONE PIDF Controller was used for the thermal application protocol. Two Campbell Scientific Data Acquisition (DAQ) systems were used to collect the mechanical load-displacement and temperature data independently. Figure 3-10 includes images of the PID controller and DAQ systems while Figure 3-11 shows an image of the heaters' PIDF controller. Figure 3-12 contains schematic representation of instrumentation plan framework. Utilizing test configuration symmetry, sufficient number of thermocouples were placed on the beam to record time temperature data. The thermocouples were designated as TCx, where x represents the thermocouple number, as shown in Figure 3-12. As seen in Figure 3-12, the PIDF controller sends signals to the ceramic heaters and actuator. In return, the actuator sends feedback (load-displacement data) to one of the DAQ systems and the thermocouples sends feedback (time-temperature data) to its corresponding DAQ system. It is important to note that one of the thermocouples, which is not shown in Figure 3-12, was used to provide a feedback loop for temperature control. This thermocouple was placed on the loader bar of the actuator near load cells. Attention was given in order to make sure the thermocouple reading placed on the actuator stays around the ambient temperature. All test data are collected in the computer through LOGGERNET software from the DAQ systems. The collected data were then post processed and analyzed for the experimental results.

Taking advantage of symmetry, the number of thermocouples placed along the beam was minimized as shown in Figure 3-12. For instance, TC4 was placed under the heater on the left side on top flange to represent the entire top flange region that is underneath the heater; however, there are no thermocouples in the same location on the right side since it is assumed that the temperature is the same on both sides. Similar TC3 was installed underneath the heater on the left side at the bottom flange to represent the temperature distribution in the region that is covered by the heaters at the bottom flange. Thermocouple TC2 and TC5 were used to collect data on temperature distribution along the cross section containing the crack.

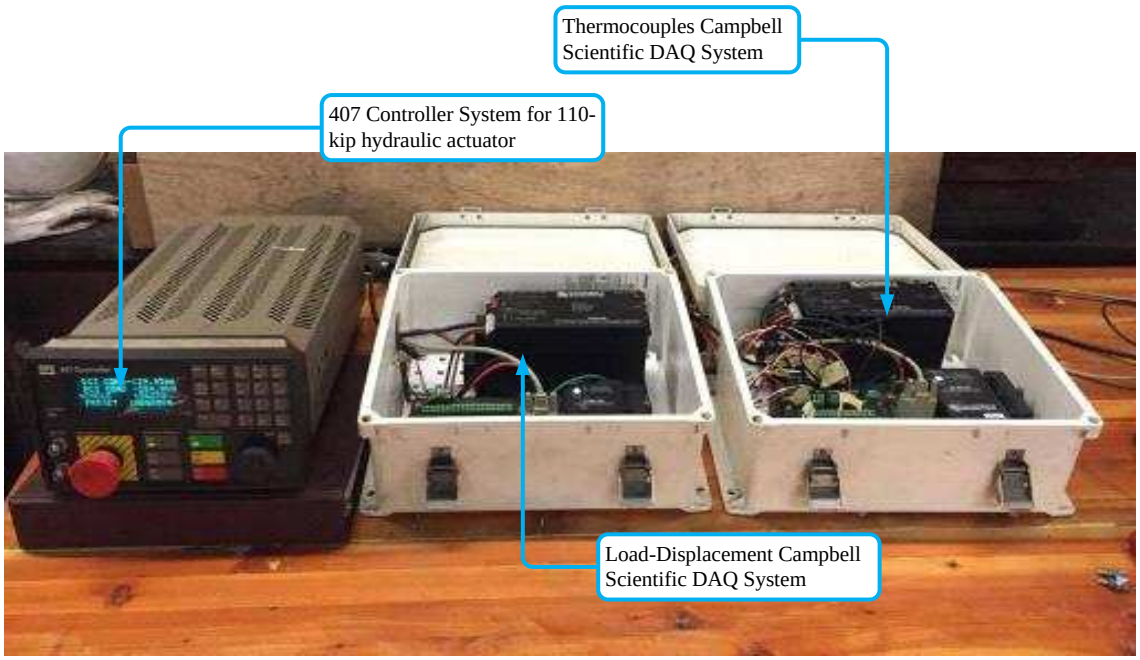

Figure 3-10: A 407 PID controller and DAQ system for the actuator and DAQ system for ceramic heaters

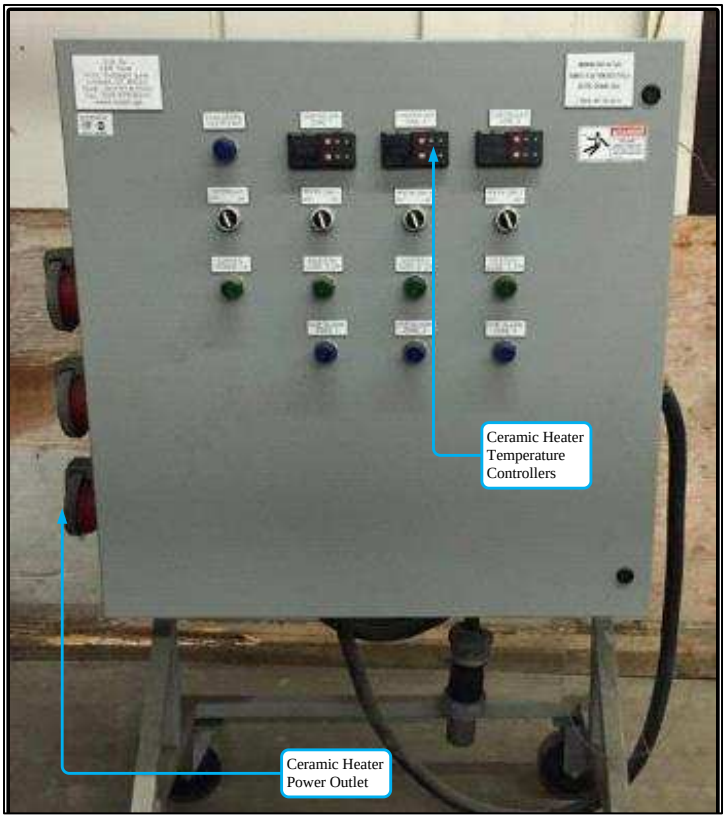

Figure 3-11: A PIDF temperature application controller system

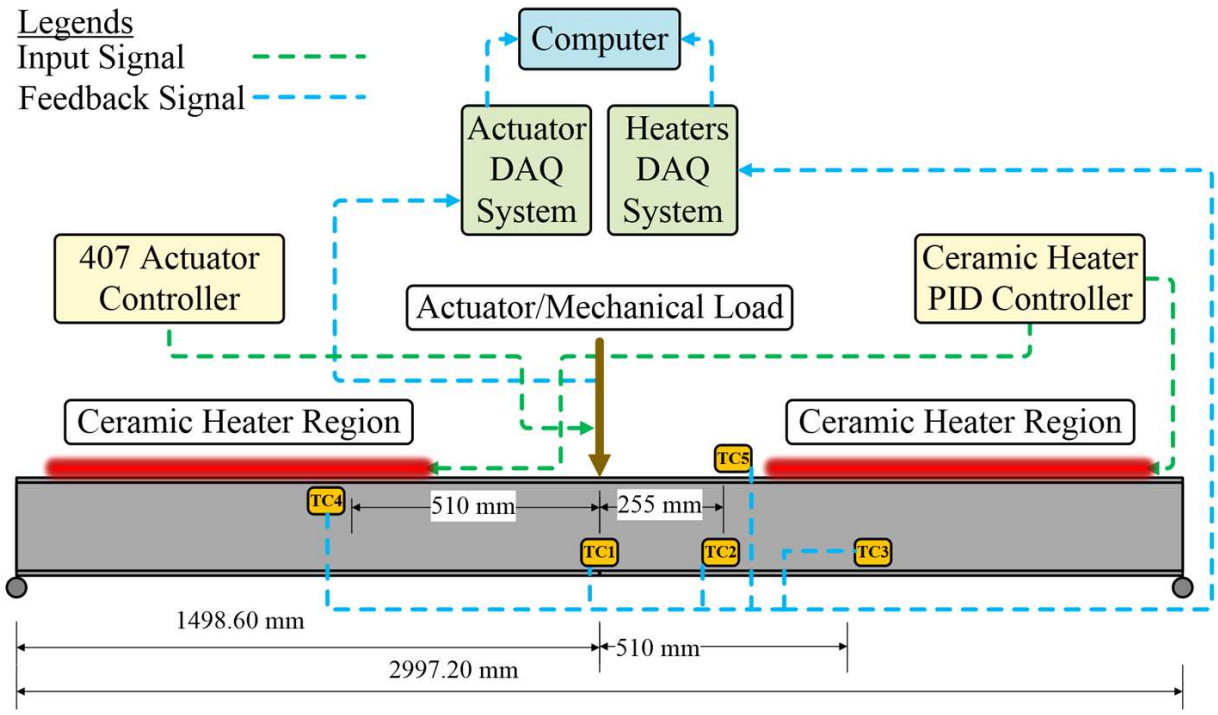

Figure 3-12: Schematic representation of the instrumentation plan framework

Additionally, Digital Image Correlation (DIC) was used to capture displacement and strain fields near the cracked flange region. This was conducted through post-processing still images, taken at various loading steps, that were collected using a digital camera placed perpendicular to the specimen side view. The camera was placed on a tripod and images were taken from a distance of 508 mm away from the specimen. Two images were collected for each specimen. The first image was taken directly before the mechanical load was applied to establish a baseline condition before any deformation. The second image was taken after the mechanical load was applied and right before failure, while the camera remained stationed at its original place. Ncorr whish is an open source 2-D digital image correlation MATLAB program was used to develop displacement and strain fields using the reference picture (unloaded) and the loaded picture. An image of the Ncorr graphic user interface (GUI) is shown in Figure 3-13. Figure 3-14 shows an image of the specimen with the region around the crack at mid span with chalk marking. As shown in Figure 3-14, chalk

was used to create random white marks in order to conduct the DIC analysis more effective since DIC analysis used the relative movements of pixels with respect to the reference picture and these white marks make the analysis smoother and more effective.

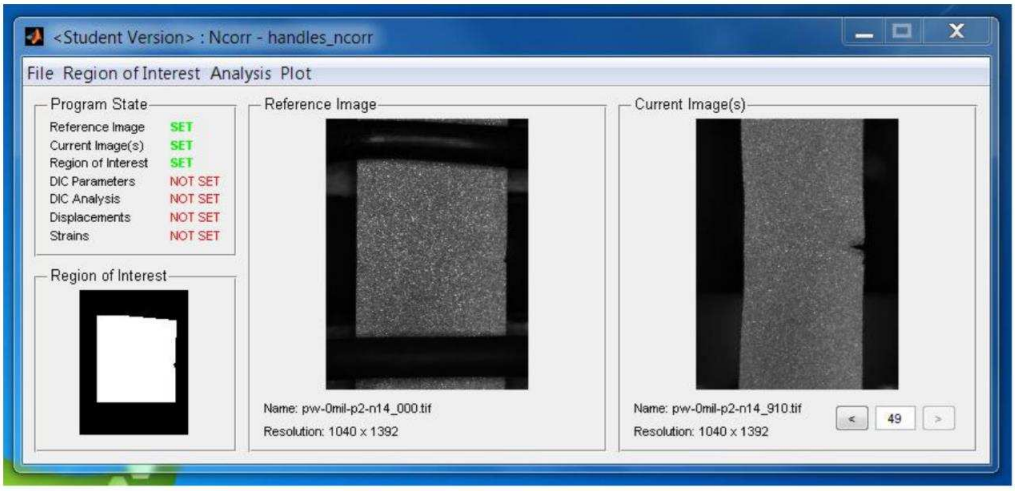

Figure 3-13: Ncorr MATLAB digital imager correlation code Graphic User Interface

Figure 3-14: Front View of the specimen mid span used for capturing pictures for DIC analysis

3.5 Testing Protocol

Testing protocols are divided in two sections, thermal testing protocol and mechanical testing protocol.

3.5.1 Thermal Testing Protocol

Thermal loading protocol was developed so that each specimen reach maximum steady state non-uniform temperature during the time of mechanical loading application. Specifically, input temperature as a function of time was divided into two segments. The first segment of the input time-temperature curve was linearly increasing with respect to time from ambient to the maximum desired temperature, which varies in each test. The second segment of the input temperature was to keep the temperature constant at the maximum desired temperature so as to reach a steady-state non-uniform distribution condition. The thermal testing protocols for specimens 2 through 4 are summarized in Figure 3-15 in the form time-temperature curves. After the temperature distribution reached steady state, mechanical loading was monotonically applied.

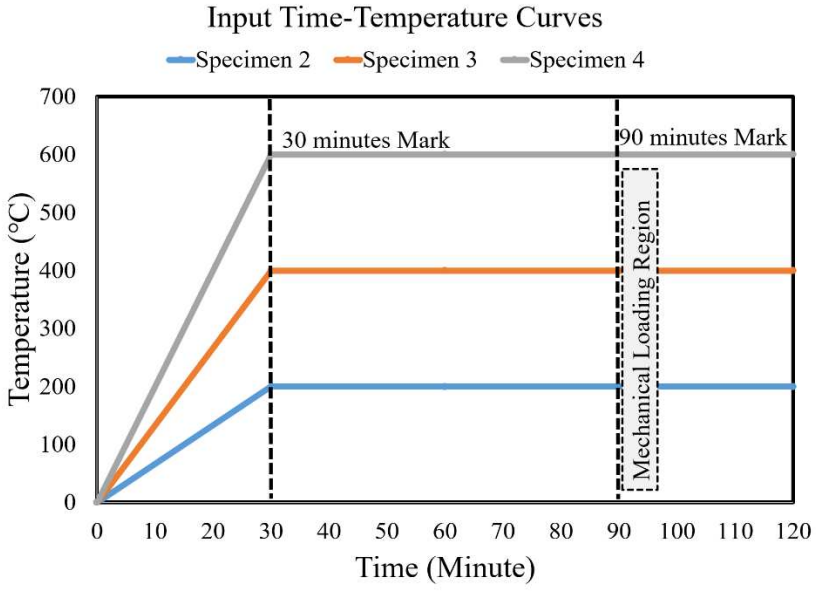

Figure 3-15: Thermal testing protocol and input time-temperature curves

3.5.2 Mechanical Testing Procedure

A 110-kip hydraulic actuator was used to apply monotonic loading at mid-span of the beam specimens until fracture occurs. This loading was applied at a rate of 4.448 kN/sec that is equivalent to 1 kip/sec until failure. Figure 3-16 contains a graph of the input mechanical loading protocol. Each specimen failed at its ultimate limit state at different load since the ultimate load to fail each specimen is different as discussed in more details in Chapter 4

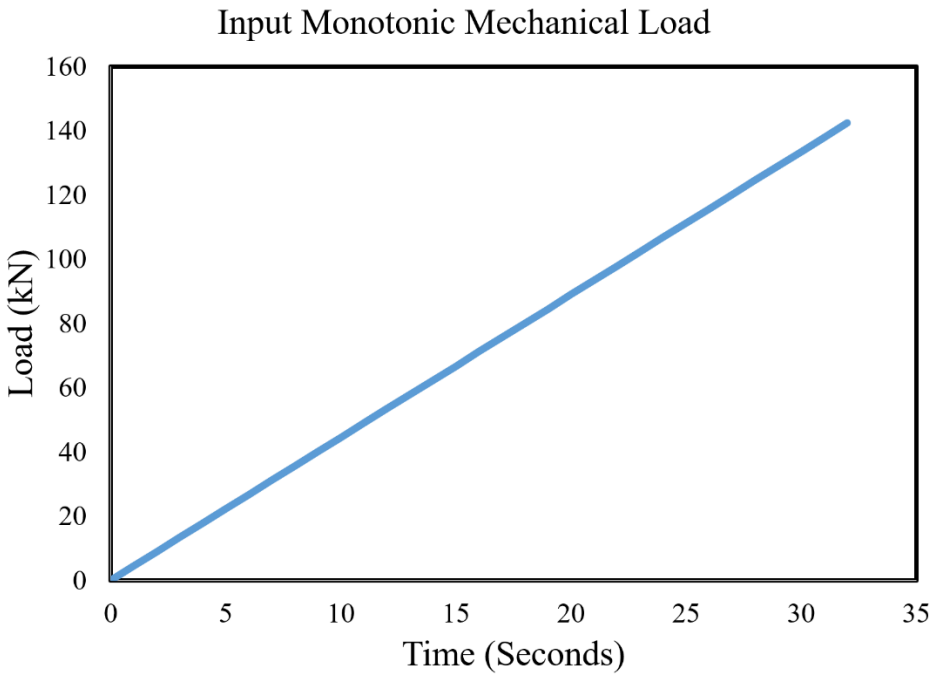

Figure 3-16: Input monotonic mechanical loading protocol

Chapter 4 - Results and Discussions

4.1 Introduction

This chapter includes the results of the testing program, which is divided into two sections – 1) thermal analysis and 2) mechanical load analysis. Time-temperature curves obtained for the specimens are provided along with 2-D finite difference analysis of steady-state heat transfer problem using thermocouple data as boundary conditions. Mechanical analysis includes discussion on load versus displacement data and digital image correlation displacement and strain fields around the crack region and fracture profiles of the specimens.

4.2 Thermal Analysis Results

Time-temperature curves and 2-D finite difference analysis and results are discussed for each specimen in this section.

4.2.1 Time-Temperature Curves

Time-temperature curves and 2-D finite difference analysis and results are discussed for each specimen in this section.

4.2.1.1 Specimen 2 Time-Temperature Curves

Figure 4-1 shows the input time-temperature curve and output time-temperature curves from all five thermocouples for specimen 2 subjected to non-uniform temperatures of up to 200 ℃. Comparing the input from PIDF controller with the recorded thermocouple data, the effect of heat loss is evident even though ceramic fiber glass insulation chamber is used in the test setup to confine the heat. Temperature non-uniformity is also observed in the data as the thermocouples placed near the heater regions, closed to the top flange, recorded higher temperatures than those further away from the heat source.

As shown in the figure, mechanical loading started at the 90-minute mark since temperature gradient distribution reached steady state and became stable in this region. There are numerous micro-level oscillations in the time-temperature curves that are due to sensitivity of thermocouple sensors. However, this is negligible since the increasing trend is held throughout the region and the region of interest, marked by the constant portion of the curves.

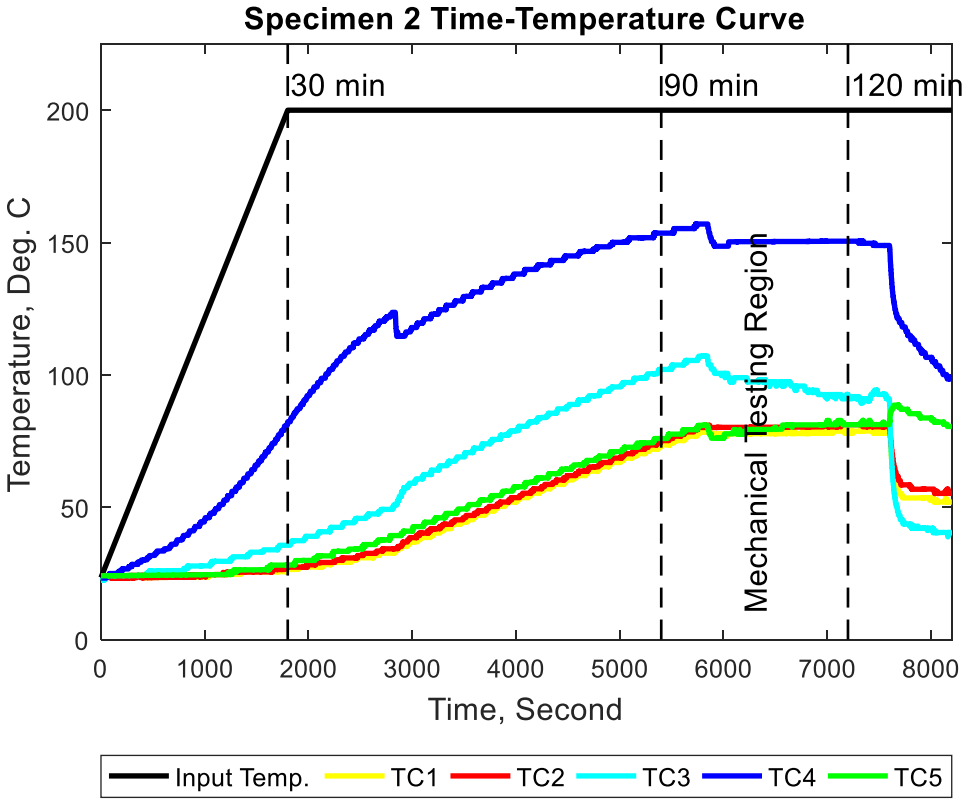

Figure 4-1: Specimen 2 time-temperature curves

4.2.1.2 Specimen 3 Time – Temperature Curves

Figure 4-2 shows the input time-temperature curve and output time-temperature curves from all five thermocouples for specimen 3, which was subjected to non-uniform temperatures of up to 400 °C. The time-temperature curves of specimen 3 indicates similar behavior to specimen 2 in terms of heat loss observations. However, TC4 located at the bottom of the top flange under the heater

sustained the height values of input temperature. This was not the case with specimen 2 where TC4 reached only up to 150 °C as shown in Figure 1. This could be due to human error in placement of insulation chamber around the beam specimens or due to heat accumulation in the chamber. The critical point is that all five thermocouples reached their steady state at the region of mechanical loading as shown in Figure 4-2. In addition, at time interval right before the mechanical testing region, TC4 showed temperature values more than the input applied temperature (2.5 % higher). This is theoretically not possible due to heat loss and is again likely attributed to the resolution of the thermocouples being used. As mentioned in Chapter 3, the standard error limit of the K-type thermocouples used is +/-0.75%. The error is attributed to the thermocouples resolution and human error.

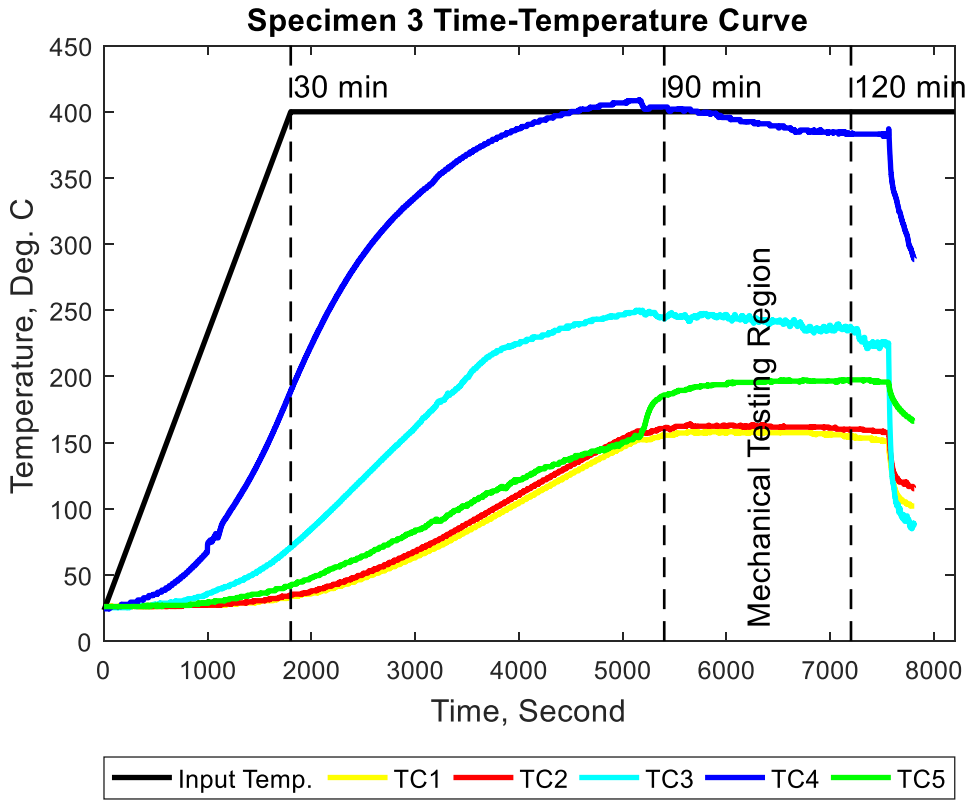

Figure 4-2: of Specimen 3 time-temperature curves

4.2.1.3 Specimen 4 Time – Temperature Curves

Figure 4-3 shows the time-temperature curves for the thermocouples installed on specimen 4 along with the input time-temperature curve, which was subjected to non-uniform temperature of up to 600 °C. The input temperature from PIDF controller in specimen 4 is similar to the other two specimens except that the maximum temperature after which the curve is kept constant is up to 600 °C. The peak temperature under the heat region from TC4 is about 11 % higher than the input applied temperature. Since the error is much higher than the thermocouples error limit, this could be due to accumulation of heat around TC4 confined by the insulation chamber. Moreover, there are some instability in the steady state test region, but overall the temperature in the test region is constant. The local oscillation in the temperature curves are also seen in specimen 4 as shown in Figure 4-3.

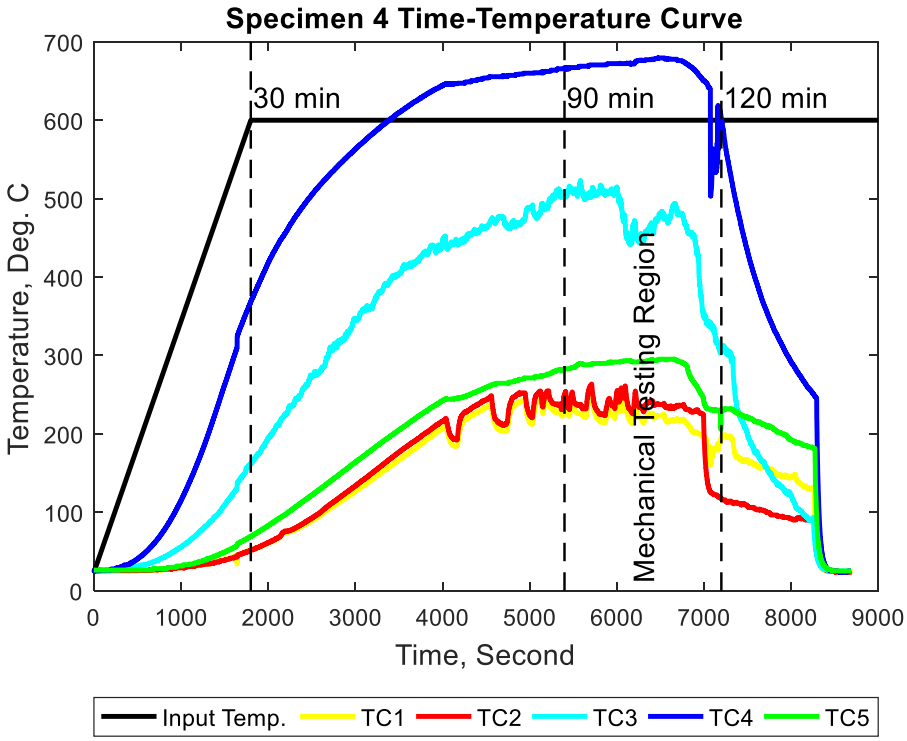

Figure 4-3: Specimen 4 time-temperature curves

4.2.1.4 Comparison of Time – Temperature Curves for all Specimens

Figure 4-4 includes comparison of thermocouple 1 (TC1) time-temperature curve for specimen 2 through 4. As indicated in Chapter 3 in Figure 3-12, TC1 is located near the cracked bottom flange region mid span. The thermocouples follow their input applied time-temperature curve. The thermocouple TC 1 in specimen 2 reached maximum temperature of about 80 ℃ in the steady state region during the mechanical testing, while TC1 in specimen 3 and 4 reached maximum steady state temperature of about 150 ℃ and 250 ℃, respectively. Instability and micro-level oscillation is higher in specimen 4 compared with specimen 2 and 3 at the mechanical testing region.

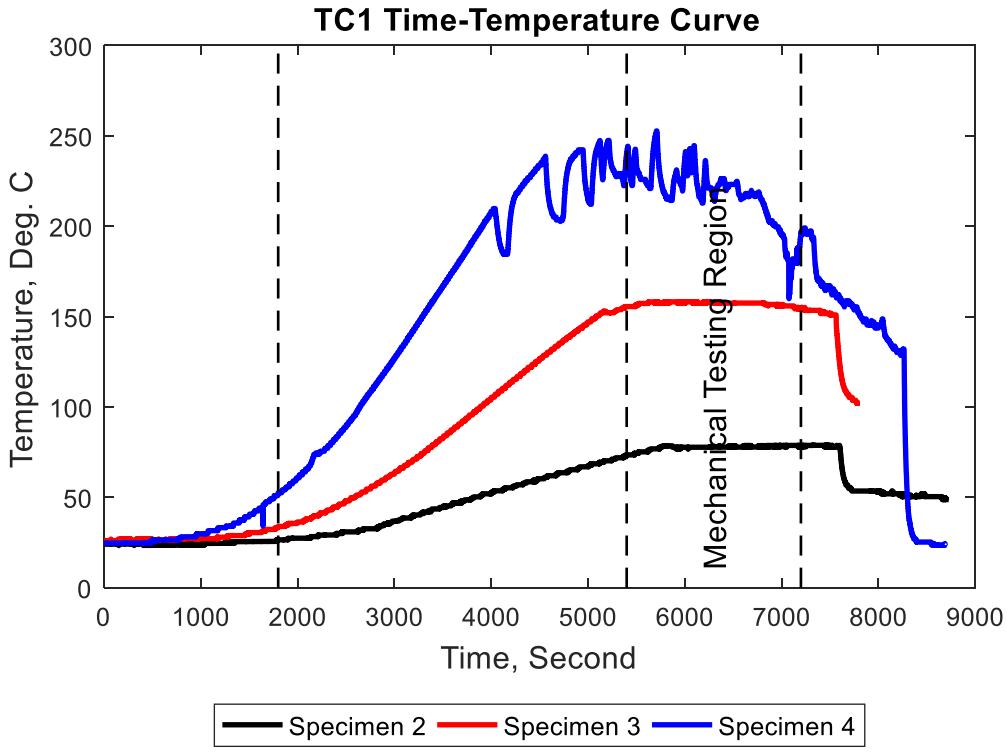

Figure 4-4: Comparison of TC1 time-temperature curve for specimens 2 through 4

Figure 4-5 shows comparison of time-temperature curves for thermocouple 2 (TC2) for specimens 2 through 4 located at the bottom flange away from the cracked region shown in Figure 3-12. The

maximum steady state temperature during mechanical loading in TC 2 reached similar values compared with TC1 for all specimens. This is because the distance between TC1 and TC2 shown in Figure 3-12 is 255 mm which small in terms of temperature gradient. TC2 also shows similar micro-behavior compared with TC1 in all specimens. However, TC2 in specimen 2 shows a rapid drop at the end of mechanical testing region. This is not a matter of concern because mechanical testing was completed at the early region of the steady state.

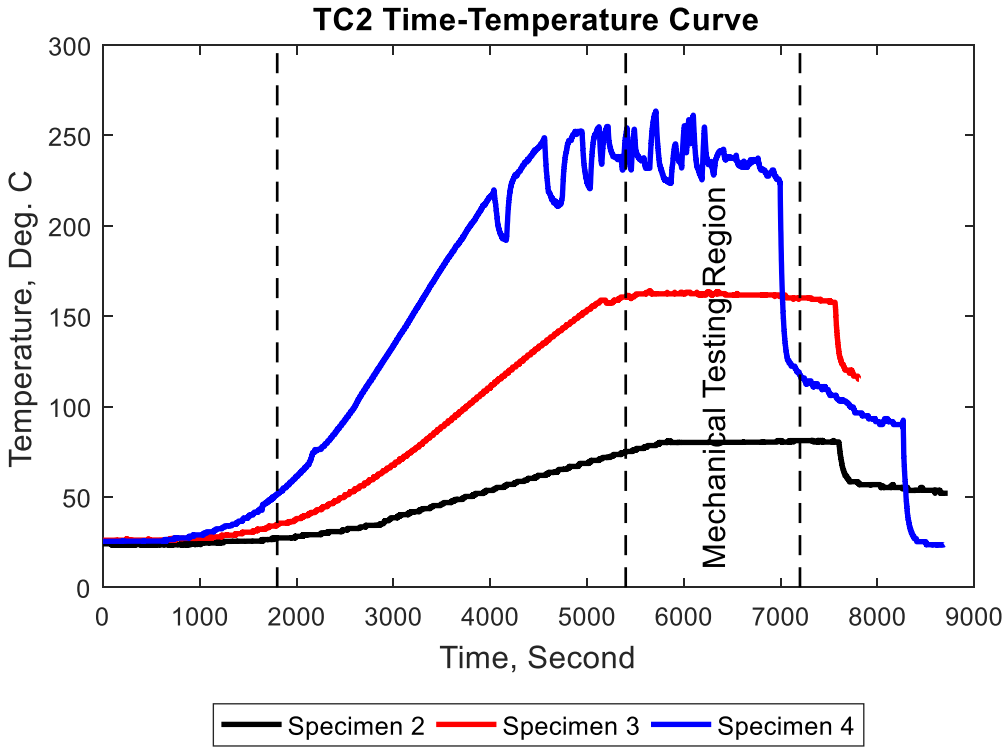

Figure 4-5: TC2 time-temperature curves for specimens 2 through 4

Figure 4-6 contains comparison of TC3 time-temperature curves for all specimens 2 through 4. Figure 3-12 in Chapter 3 shows the location of TC3 which is located 510 mm away from the mid span at the bottom flange under near the heaters region. TC3 in specimen 2 reached maximum steady state temperature of about 100 °C. The maximum steady state temperature of TC3 in

specimen 3 and 4 reached about 230 ℃ and 550 ℃ respectively. TC3 picked up higher values of input temperature compared with TC1 and TC2 because it is located closer to the heat source.

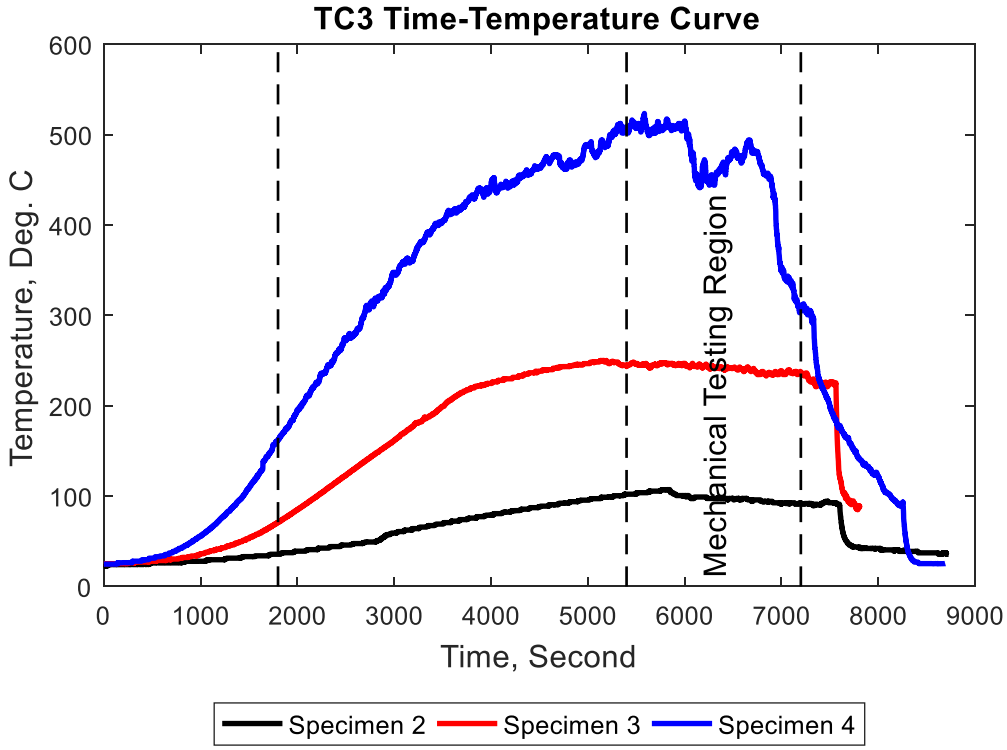

Figure 4-6: TC3 time-temperature curves for specimens 2-4

The time-temperature curves of TC4 for specimens 2 through 4 is summarized in in Figure 4-7. TC4 was located right underneath the heater region at the top flange 550 mm away from mid span at shown in Figure 3-12 in Chapter 3. Except specimen 2 where TC reached maximum steady state temperature of about 140 ℃, the other specimens reached the maximum input temperature in the mechanical region. TC4 has the highest micro-level stability in the mechanical testing region compared with all other thermocouples. In addition, the reason why TC4 picked up higher temperature than applied temperature is explained previously.

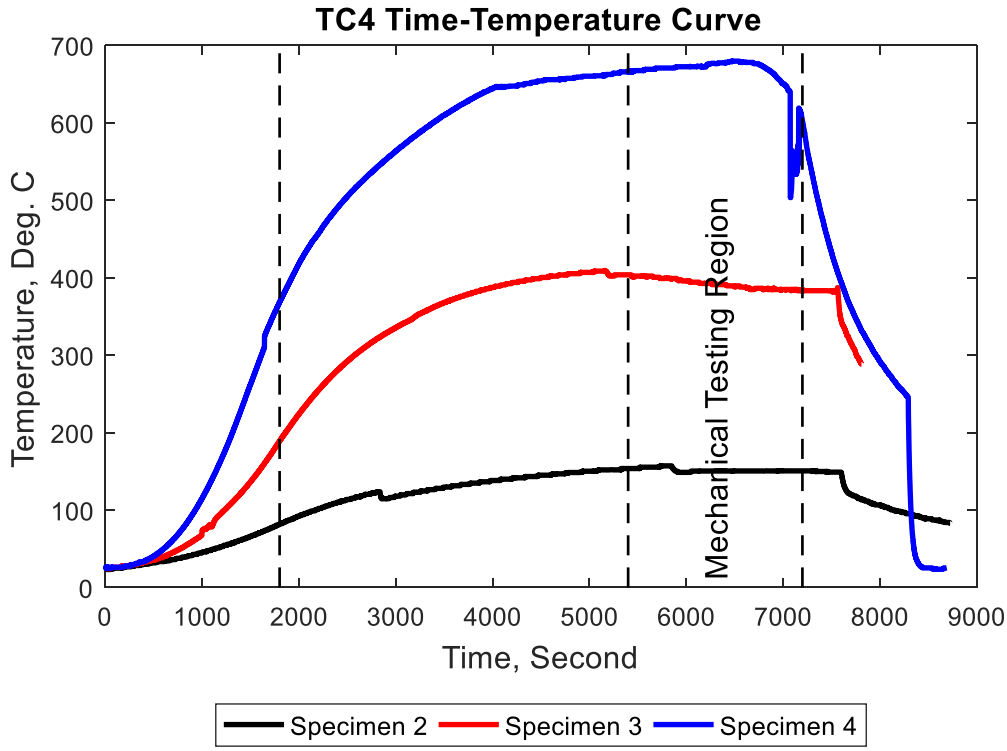

Figure 4-7: TC4 time-temperature curves for specimens 2-4

TC5 time-temperature curves in included in Figure 4-8. TC5 was located in the top flange between the mid span crack region and the inner edge of the heater region. The steady state maximum temperature values recorded by TC5 is similar to TC1 and TC2 and that is because these three thermocouples were located away from the heat source. The other reason these three thermocouples registered lower temperatures at the steady state region is because this region of the insulation chamber was opened several times in order to capture pictures for Digital Image Correlation (DIC) analysis.

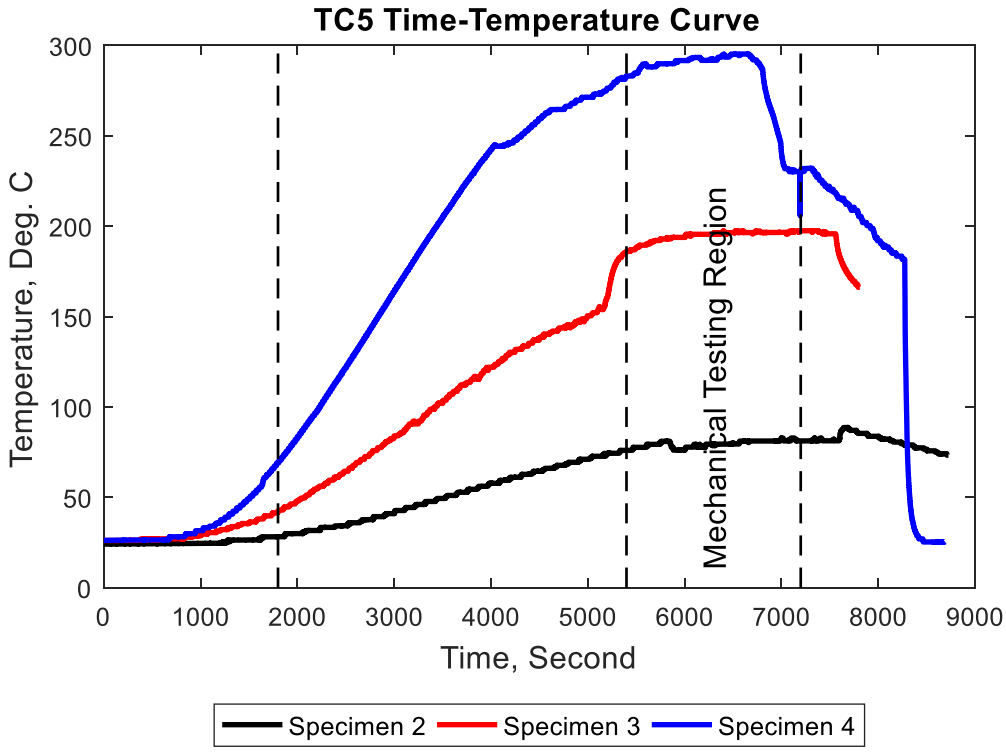

Figure 4-8: TC5 time-temperature curves for specimens 2-4

4.2.2 Temperature Distribution along the Specimen Length

This section presents results of 2-D finite difference analysis for specimens 2 through 4 using a MATLAB code and interpolation of thermocouple values as boundary conditions. The 2-D temperature gradient for the mentioned specimens shows steady state temperature distribution along the beam span during mechanical loading.

4.2.2.1 Temperature Distribution along Specimen 2

Figure 4-9 shows a 2-D temperature distribution for specimen 2 during the mechanical loading along the beam span. Due to large ratio of span to depth of the beam, the 2-D figure is not to scale in order to fit it in the page. The maximum temperatures shown in Figure 4-9 is the same as the one shown in time-temperature curves for specimen 2 because the 2-D heat distribution was

created using average interpolated values of the thermocouples at the steady state stage. The maximum steady state temperature in specimen 2 reached only up to 150 ℃ of the applied 200 ℃ input temperature from the heat source. In addition, the maximum temperatures are seen in the region underneath the heater because that is where the conduction heat transfer took place.

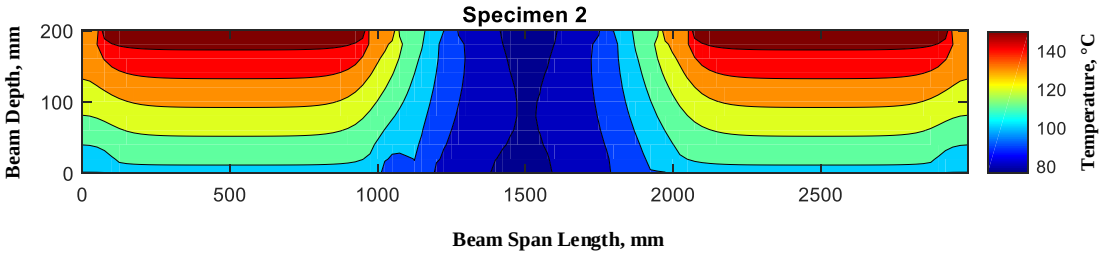

Figure 4-9: Specimen 2 steady state temperature distribution along the span of the beam

4.2.2.2 Temperature Distribution along Specimen 3

The 2-D steady state heat distribution for specimen 3 along the beam span is shown in Figure 4-10. The temperature distribution in specimen 3 is similar to specimen two, however, unlike specimen 2, the maximum temperature registered the full applied input temperature in the heater region. The temperature distribution at mid span around the cracked region is relatively uniform as a result of the values of TC 1, 2 and 5 being similar.

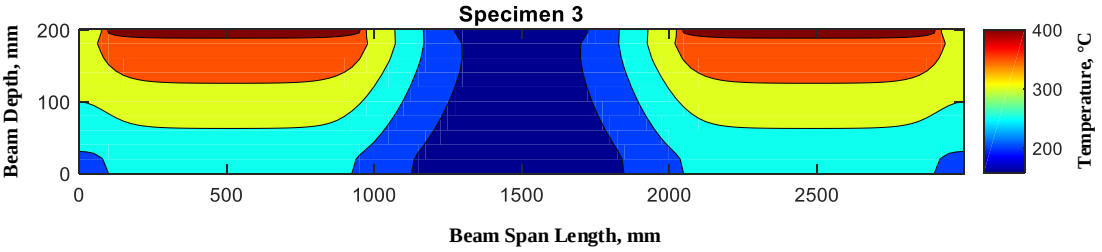

Figure 4-10: Specimen 3 steady state temperature distribution along the span of the beam

4.2.2.3 Temperature Distribution along Specimen 4

Steady state temperature distribution in 2-D along the beam span for specimen 4 is included in Figure 4-11. The maximum temperature in specimen 4 also picked up the full applied input temperature. Similar to the previous specimens, the mid span region of specimen 4 has relatively uniform temperature. Specimen 4 has the highest non-uniform temperature compared with specimen 2 and 3.

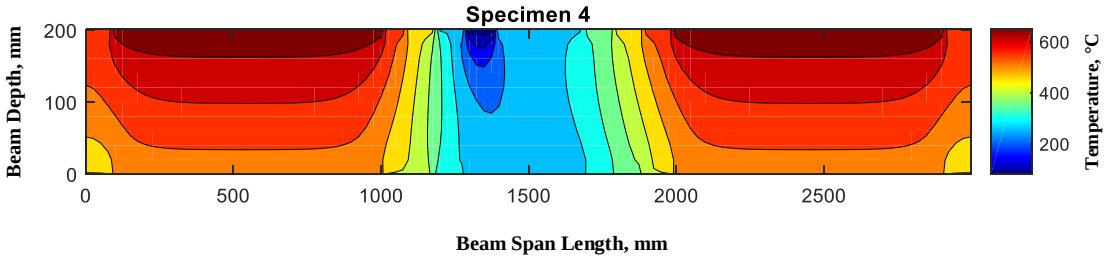

Figure 4-11: Specimen 4 steady state temperature distribution along the span of the beam

4.2.2.4 Comparison of Temperature Distribution along all Specimens

Comparison of the 2-D steady state temperature distributions from the finite difference analysis for all four specimens are included in Figure 4-12. The 2-D contours are plotted along the span length of the beam; however, as mentioned earlier, the dimensions of the beam span and depth are not to scale. The 2-D contour plots represent the average steady state temperature distribution during the mechanical testing time interval. As seen in Figure 4-12, the steady state temperature distribution contour for specimen 1 is uniform since it was tested at ambient temperature and therefore all boundary conditions were set to ambient temperature of 23.4 °C. The other three specimens have non-uniform temperature distribution contours and all three exhibit similar trends. The highest temperature in all three specimens is found in the region where the heaters were mounted. Since the thermocouples were placed at specific points along the beam, the rest of the

boundary condition points were linearly interpolated between the thermocouple data points across and along the beams.

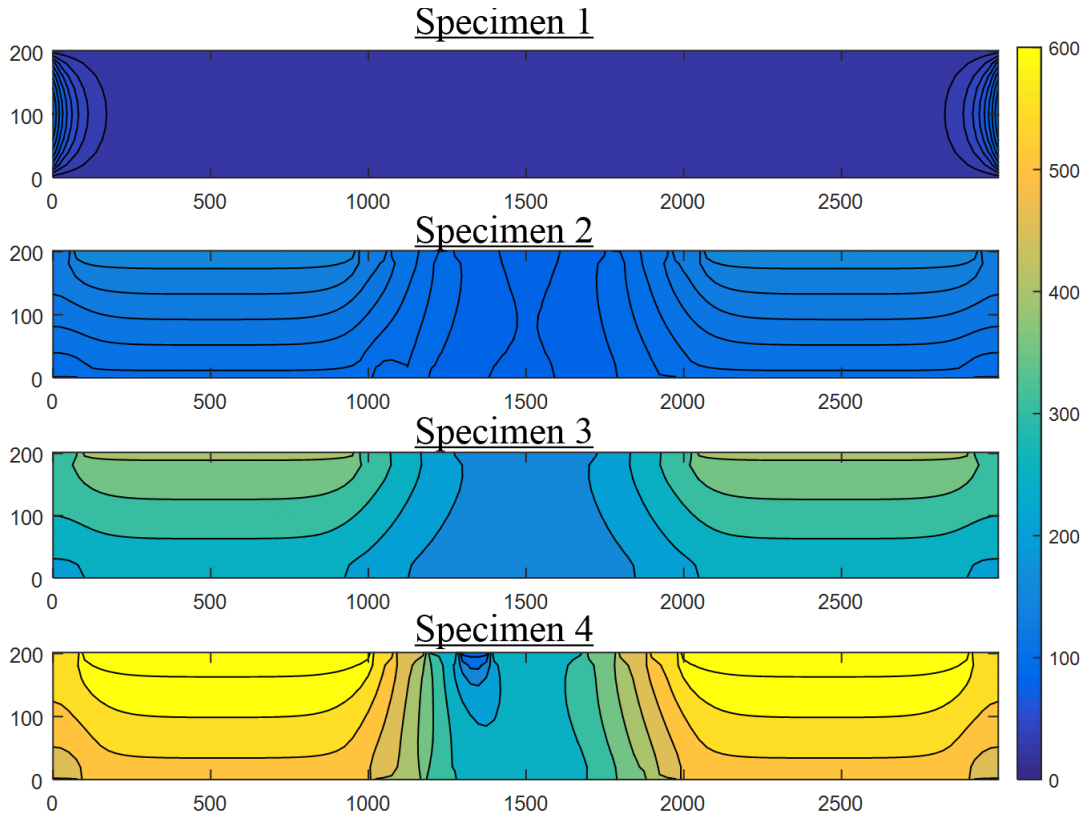

Figure 4-12: Steady state temperature distribution along the beam span for all specimens

4.3 Mechanical Loading Results

Results and comparison of global failure behavior of each specimen under ultimate mid span loading and local behavior of the cracked w-section and fracture surfaces are presented in this section.

4.3.1 Load versus Displacement Curves

This section contains load versus displacement curve for all the specimens as well as their comparison and discussion.

4.3.1.1 Load versus Displacement Curve for Specimen 1

The load versus displacement curve for specimen 1 is shown in Figure 4-13 where it fractured at an ultimate load of about 113.25 kN. Specimen 1 was tested at ambient temperature (23.4 ℃) as the control specimen. Maximum displacement of specimen 1 at the time of fracture was 27.64 mm, and the average stiffness before yielding was 7281.02 kN/mm.

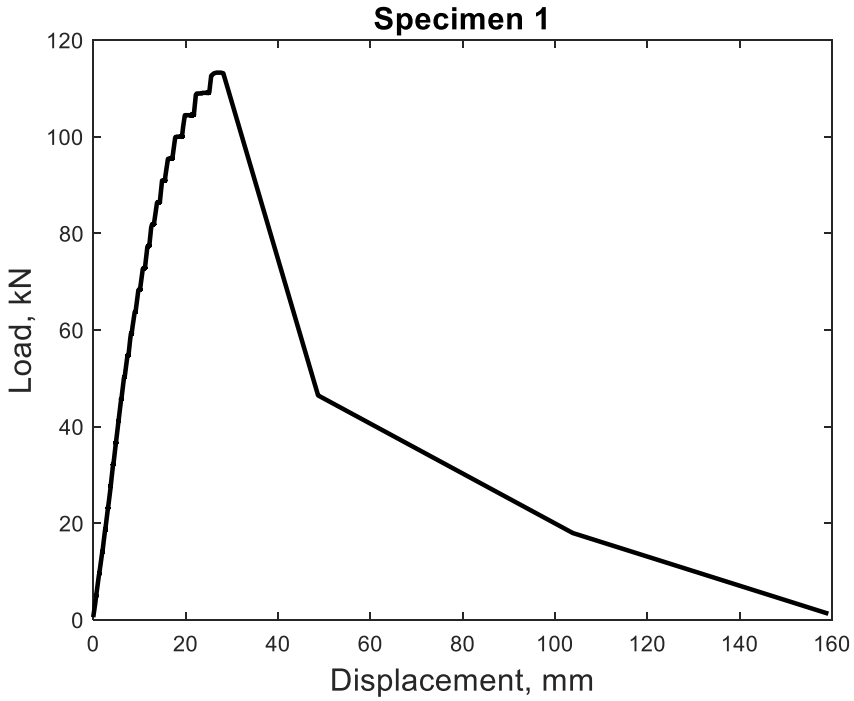

Figure 4-13: Specimen 1 load versus displacement curve

4.3.1.2 Load versus Displacement Curve for Specimen 2

Figure 4-14 includes load versus displacement curve for specimen 2, which fractured at 119.19 kN ultimate load, slightly higher than specimen 1. This specimen was tested at non-uniform

temperature of up to 200 ℃. Maximum displacement of specimen 2 at the ultimate fracture load was 37.11 mm. The average stiffness calculated from the linear portion of the curve was 3574.42 kN/mm.

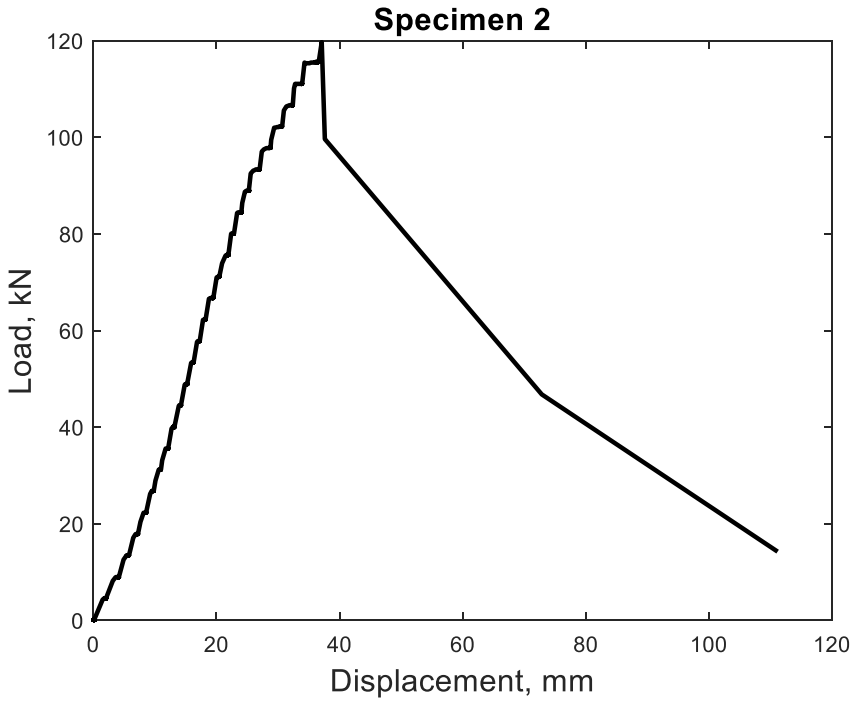

Figure 4-14:Specimen 2 load versus displacement curve

4.3.1.3 Load versus Displacement Curve for Specimen 3

Figure 4-15 shows the load versus displacement curve for specimen 3 tested at non-uniform temperature of up to 400 ℃. Specimen 3 fractured at an ultimate load of 131.76 kN with corresponding maximum displacement of 39.65 mm. The average calculated stiffness of specimen 3 was 3334.20 kN/mm.

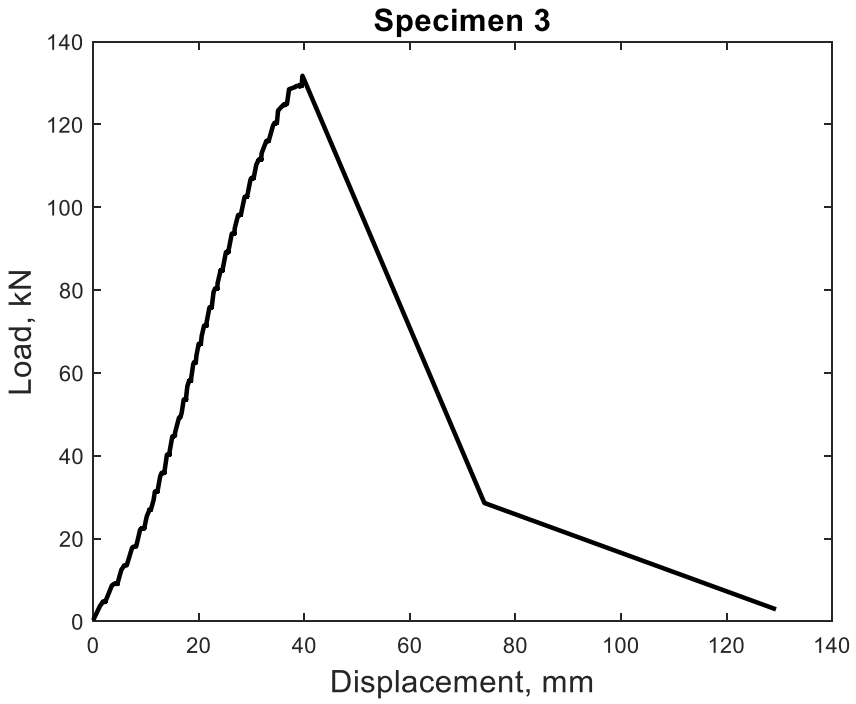

Figure 4-15: Specimen 3 load versus displacement curve

4.3.1.4 Load versus Displacement Curve for Specimen 4

The load versus displacement curve for specimen 4, which failed in excessive deflection is shown in Figure 4-16. The ultimate load at failure was 93.19 kN with maximum deflection of 95.73 mm. The average stiffness of specimen 4 was 111.19 kN/mm.

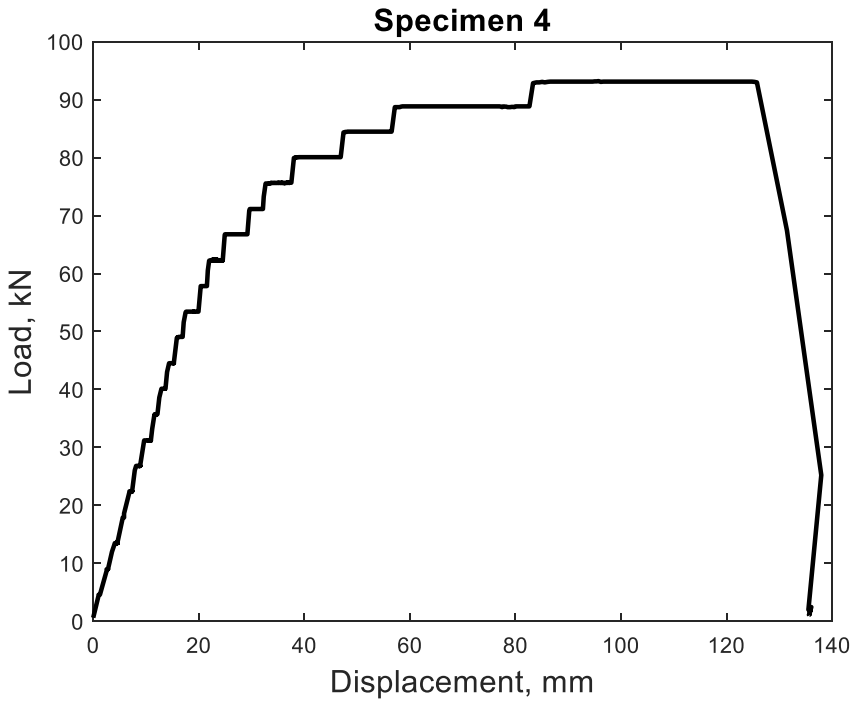

Figure 4-16: Specimen 1 load versus displacement curve

4.3.1.5 Comparison of Load versus Displacement Curve for all Specimens

The load versus displacement curves for all four specimens are shown in Figure 4-17. Table 4-1 summarizes stiffness, ultimate load, ductility energy (J-integral) and mid-span maximum deflection of all four specimens with normalized values with respect to the corresponding highest values. Figure 4-18 contains a bar chart with normalized values of stiffness, strength, J-integral and maximum deflection. The stiffness values were calculated from the average slope of the linear elastic portion of the load-displacement curves and the ultimate load and maximum mid-span deflection were taken from the load-displacement data. The J-integral values were calculated from the area under the curve using the experimental developed equation discussed in Chapter 2.

As shown in Figure 4-17, while the ultimate load to fracture with the corresponding maximum displacement increased with increasing the applied temperatures, the stiffness dramatically

decreased with increasing temperature. Similarly, the J-integral value, which is a function of steel plastic fracture toughness, increased with increasing temperature. While steel losses stiffness and modulus of elasticity under elevated temperature, fracture toughness of steel improves with increasing temperature. However, this trend changes with specimen 4 is taken into consideration. That is because steel loses about 50 % of its stiffness and strength at 600 ℃. In addition, fracture capacity of steel increases elevated temperature only to a certain level and then it decreases. The competition between strength of steel at elevated temperature with fracture toughness is evident in specimen 4 where steel degradation at elevated temperature is much more dominant compared with increase in the fracture capacity at elevated temperature. In result the specimen failed in excessive deflection.

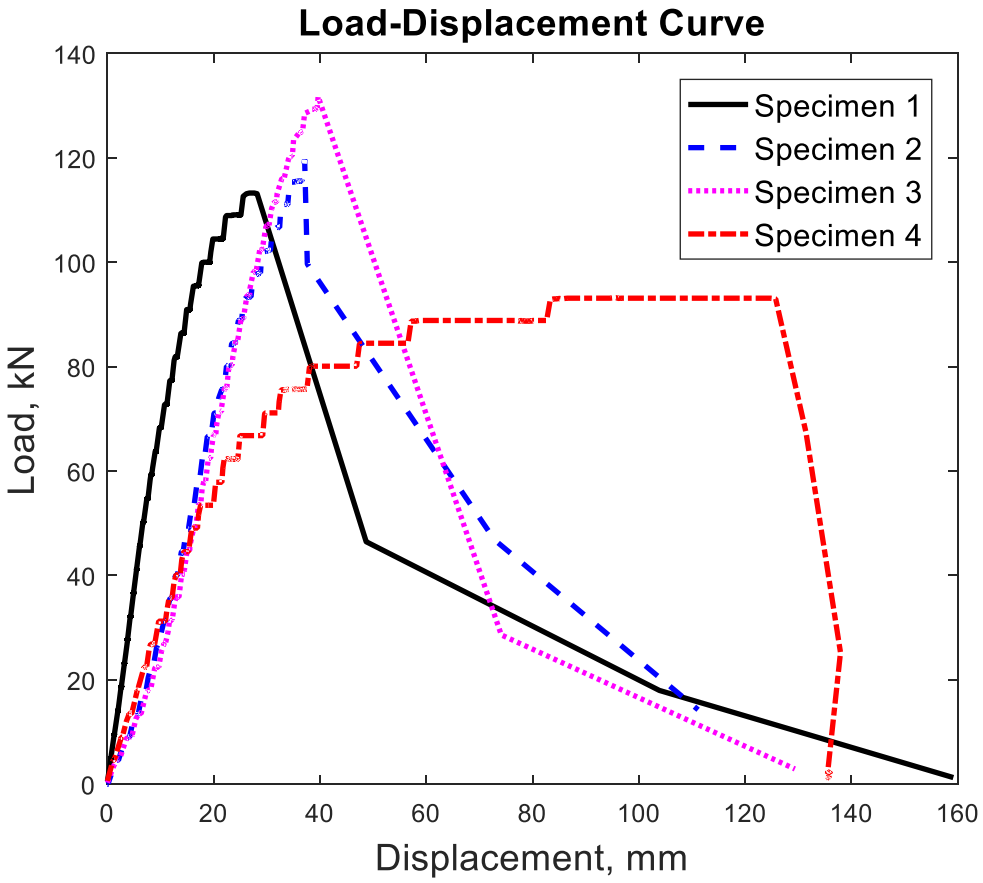

Figure 4-17: Comparison of load versus displacement curves for specimens 1-4

Table 4-1: Fundamental behavior Characteristics of the Beams

Stiffness				
	Specimen 1	Specimen 2	Specimen 3	Specimen 4
Stifness (kN/m)	7281.02	3574.42	3334.20	111.19
Normalized Stiffness	1.00	0.49	0.46	0.02
Strength				
	Specimen 1	Specimen 2	Specimen 3	Specimen 4
Ultimate Load (kN)	113.25	119.70	131.76	93.19
Normalized Strength	0.86	0.91	1.00	0.71
J-Inetegral				
	Specimen 1	Specimen 2	Specimen 3	Specimen 4
J-Integral (kJ/mm^2)	9.34	10.24	10.47	17.52
Normalized J-Integral	0.53	0.58	0.60	1.00
Maximum Deflection				
	Specimen 1	Specimen 2	Specimen 3	Specimen 4
Deflection at Ultimate Load (mm)	27.64	37.11	39.65	95.73
Normalized Deflection	0.29	0.39	0.41	1.00

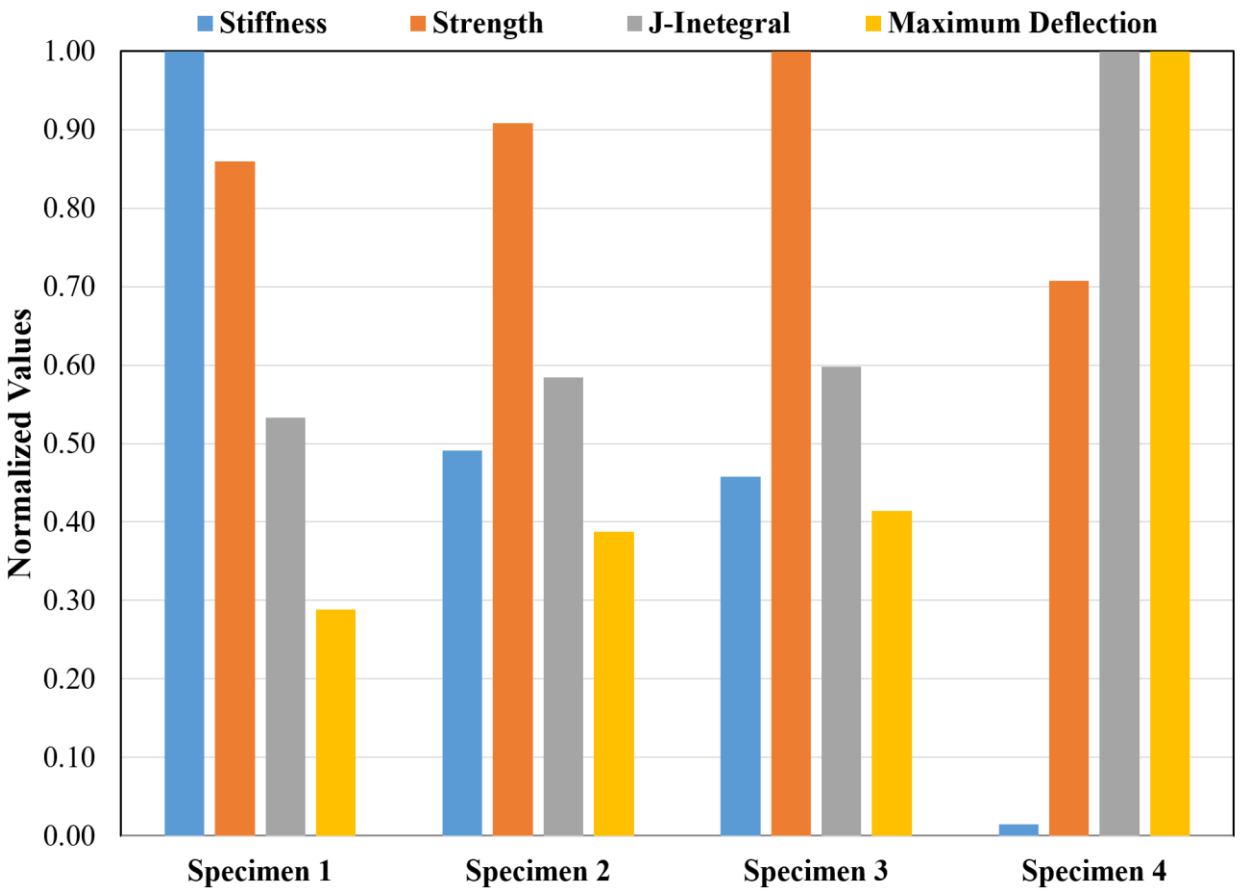

Figure 4-18: Normalized values of stiffness, strength, J-integral and maximum deflection

4.3.2 Overall Failure and Fracture Characteristics

This section covers overall failure behavior and fracture profile and characteristics of each specimen. Failure of each specimen along with details of the fracture surfaces are discussed in here in terms of brittle to ductile fracture.

4.3.2.1 Overall Failure and Fracture Characteristics of Specimen 1

Failure of specimen 1 was marked by an overall fracture along the section containing the pre-existing crack. Figure 4-19 shows a side view of the fractured section of the beam at mid span. The specimen fractured vertically in a straight line. As seen in the figure, the fracture initiated from

the cracked bottom flange and zipped through all the way up top flange. The steel plate seen on top flange was used in order to avoid premature local flange buckling from the mechanical point load application.

Figure 4-19: Specimen 1 global failure behavior

The fracture surface profile for specimen 1 is included in Figure 4-20. This figure includes one side of the fracture surfaces. The fracture surface is divided in two segments with magnified views. The section fractured in a brittle manner initially up to about 45 mm in the first segment as shown in Figure 4-20. Chevron marks are shown on the surface, which are distinctive of brittle fracture. The fracture in the second segment is more ductile as indicative by shear lips along the crack face.

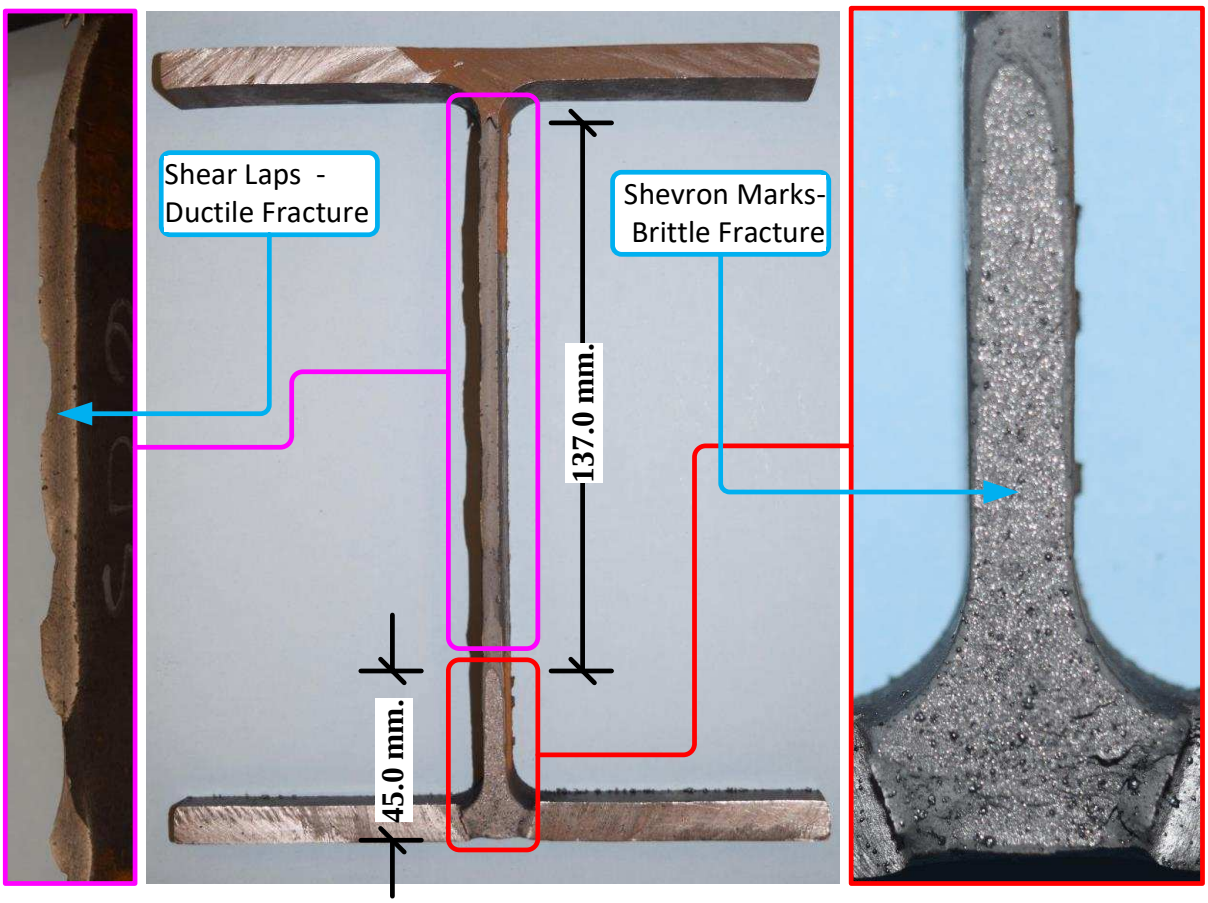

Figure 4-20: Specimen 1 fracture profile & characteristics

4.3.2.2 Overall Failure and Fracture Characteristics of Specimen 2

Failure behavior of specimen 2 is shown in Figure 4-21. Specimen 2 fractured similar to specimen 1 as shown in the figure. The insulation chamber made out of ceramic fiber is seen around the beam specimen in Figure 4-21.

Figure 4-21: Specimen 2 global failure behavior

The fracture surface profile for specimen two is shown in Figure 4-22. Specimen two fracture surface profile is also divided in two parts. The first part of the fractured surface is about 76 mm along the w-section depth and the second part of the fractured surfaces extends all the way up to the top flange. Looking at the magnified views of the fracture profile, the signs of brittle fracture has decreased significantly compared with specimen 1. There are only few Chevron marks at the very start of the fracture and the rest of the profile is characterized with shear lips, which is a sign of ductile fracture. This makes sense because temperature increases ductility energy, causing the fracture to be more ductile.

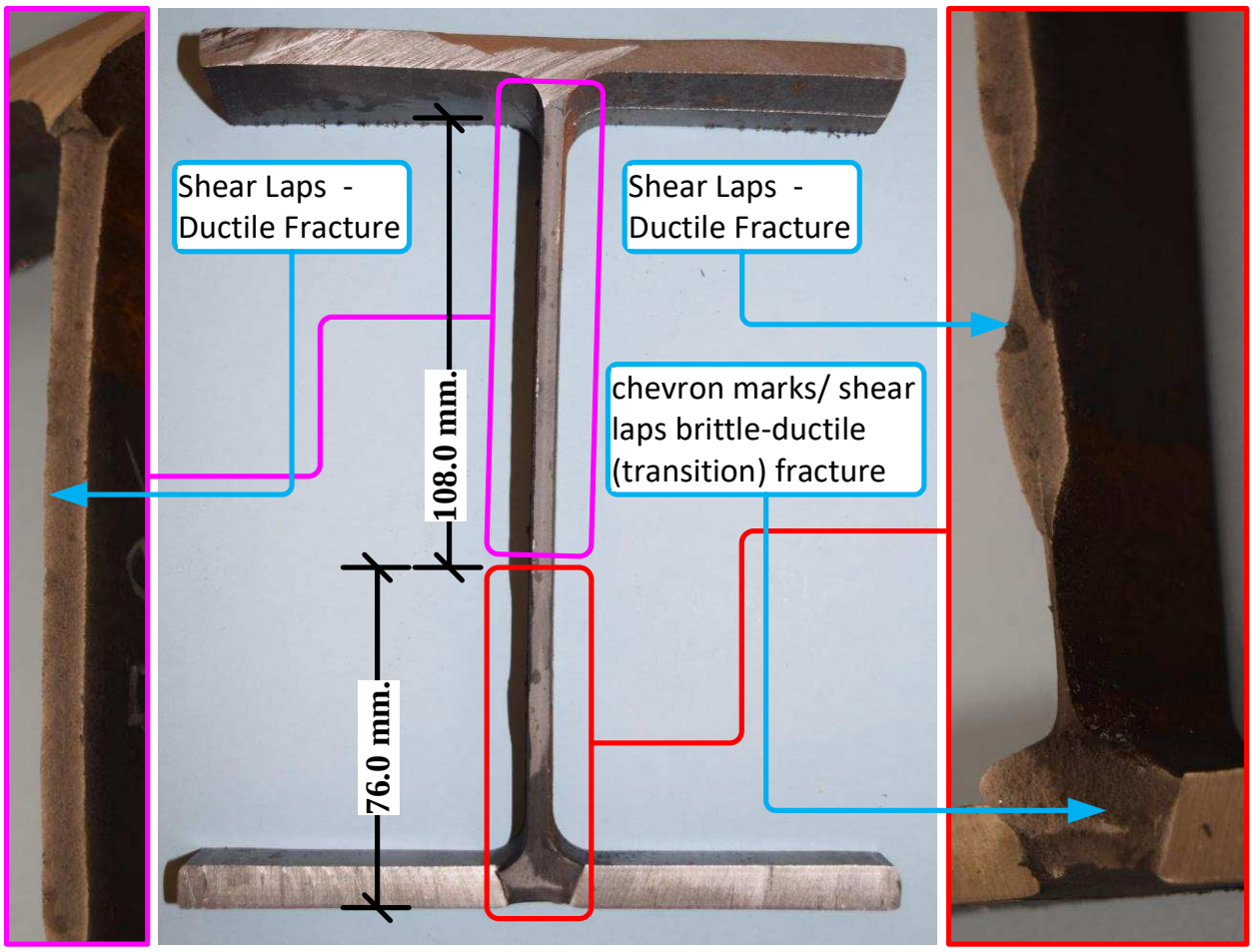

Figure 4-22: Specimen 2 fracture profile & characteristics

4.3.2.3 Overall Failure and Fracture Characteristics of Specimen 3

Specimen 3 after fracture failure is shown in Figure 4-23, which also fractured very similar to specimen 1 and 2 in terms of its global behavior.

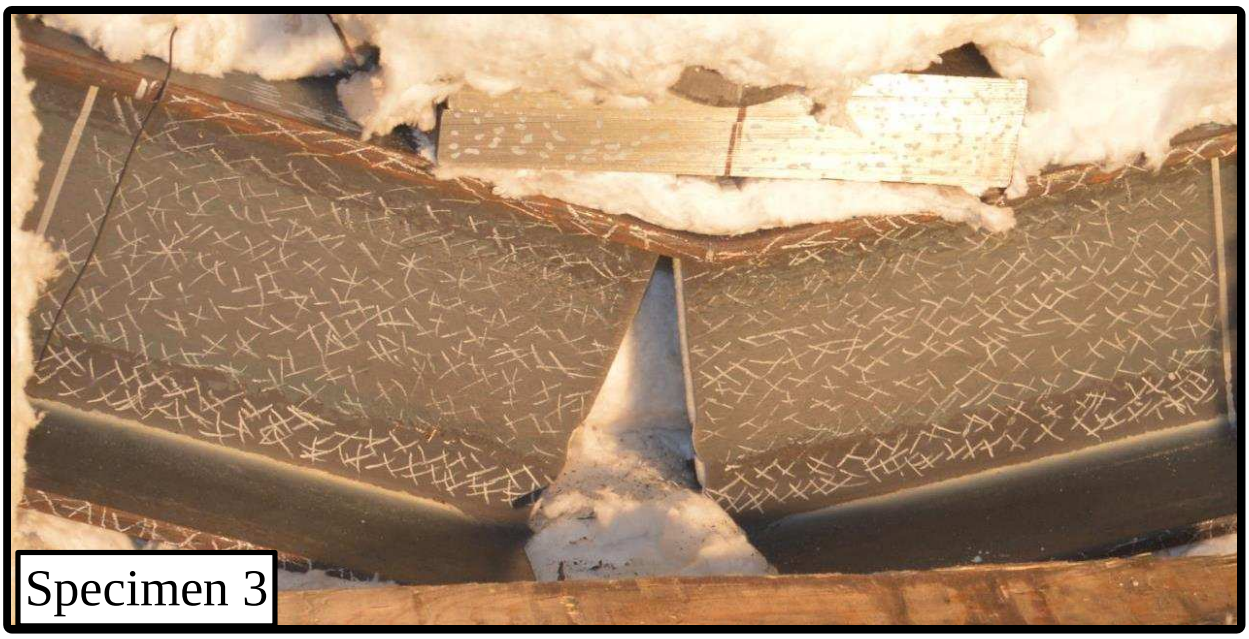

Figure 4-23: Specimen 3 global failure behavior

Figure 4-24 shows the fracture surface profile for specimen 3, which was tested at non-uniform temperature of up to 400 °C. When evaluating the fracture profile of specimen 3, one can clearly see no signs of brittle fracture (i.e. the absence of chevron marks). The entire surface is marked by shear lips, indicating ductile fracture. This specimen follows the trend that with increasing temperature fracture becomes more ductile, which is consistent with fracture mechanics failure theories.

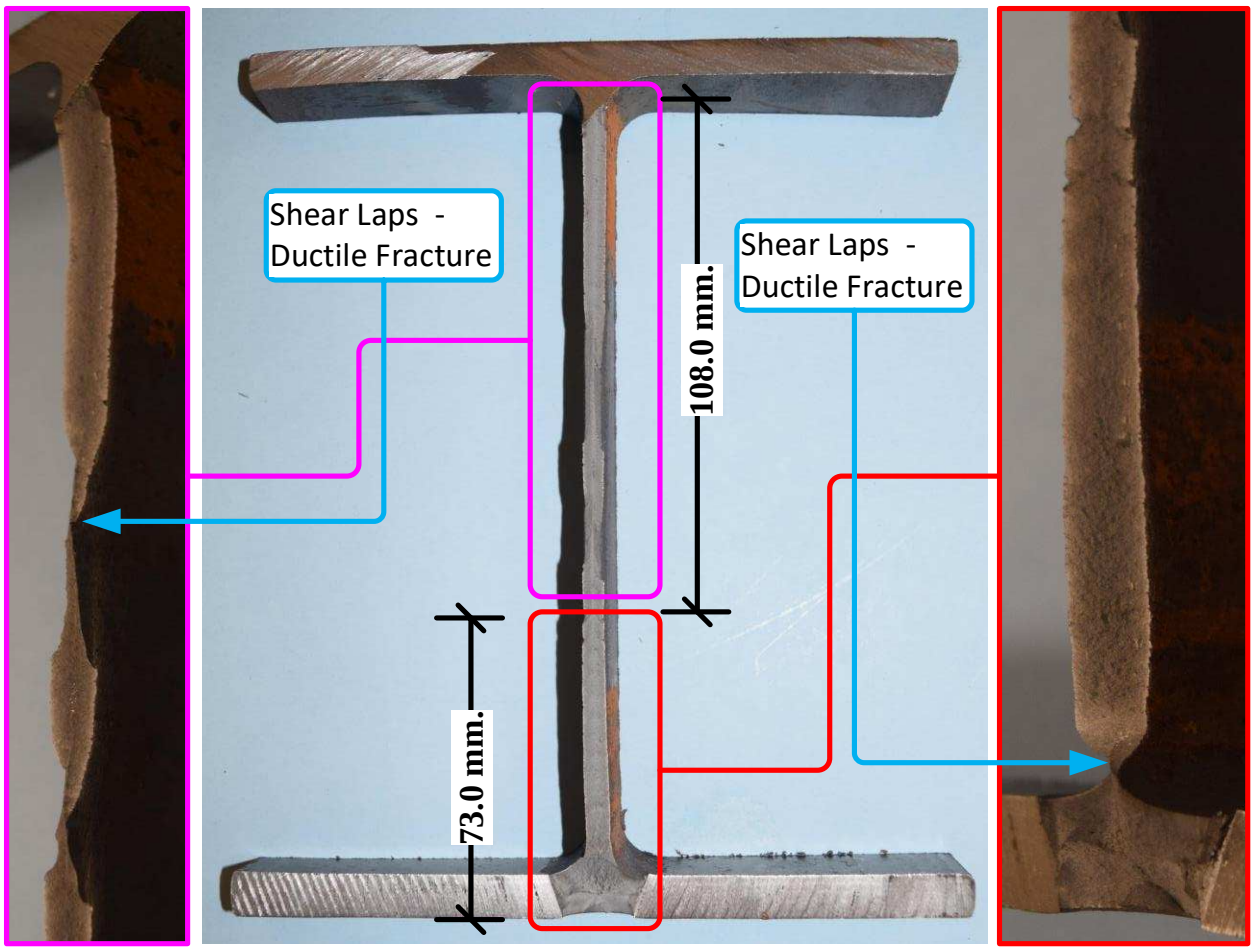

Figure 4-24: Specimen 3 fracture surface profile & characteristics

4.3.2.4 Overall Failure and Fracture Characteristics of Specimen 4

Figure 4-25 includes picture of specimen 4 after ultimate failure. As shown in the figure, specimen 4 did not fracture at all. The failure behavior of this specimen is completely different than the other three specimens. This is because specimen 4 was tested at elevated temperatures of up to 600 ℃. The excessive temperature shifted the failure from a fracture along the cracked section to global deflection. The bottom flange mid-span image of specimen 4, which failed in excessive deflection is shown in Figure 4-26. There is no fracture profile to discuss for specimen 4. As seen in figure, the pre-existing crack in the bottom flange is at its place after the ultimate failure of the beam

specimen. However, there are minor signs of plastification near the crack tip from both sides as shown in the figure. The competition between the decreasing modulus of elasticity, hence the excessive deflection, and the increasing fracture toughness played a role in the overall behavior of this specimen. That is because the stiffness of the steel degraded the fracture toughness increased.

Figure 4-25: Specimen 4 global failure behavior

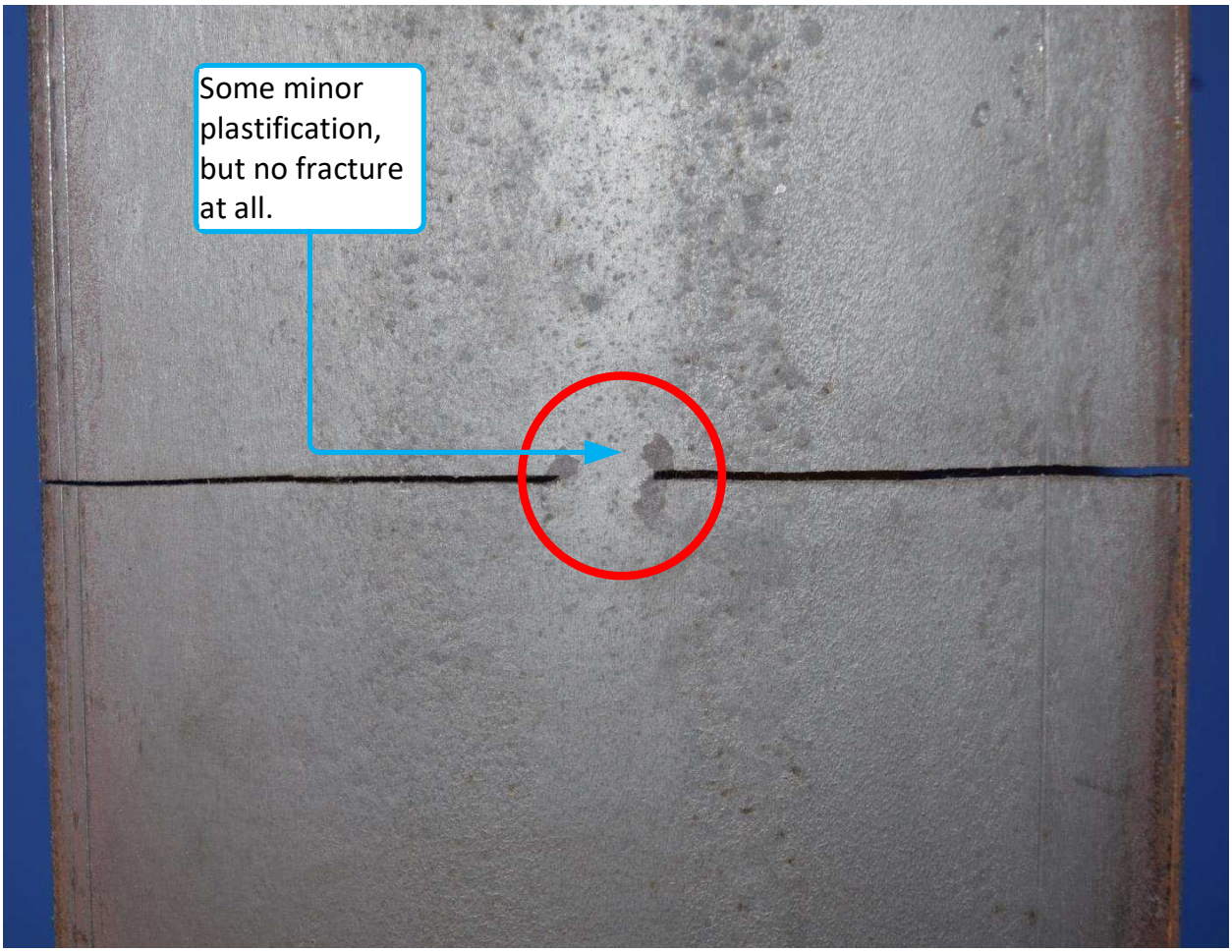

Figure 4-26: Specimen 4 mid span bottom flange view after failure

4.3.2.5 Comparison of Overall Failure and Fracture Characteristics for all Specimens

Table 4-2 and Figure 4-27 summarizes comparison of failure and fracture behavior of all specimens.

Table 4-2: Failure modes of beam specimens

	Specimen 1	Specimen 2	Specimen 3	Specimen 4
Ultimate Failure Mode	Fracture	Fracture	Fracture	Excessive Deflection

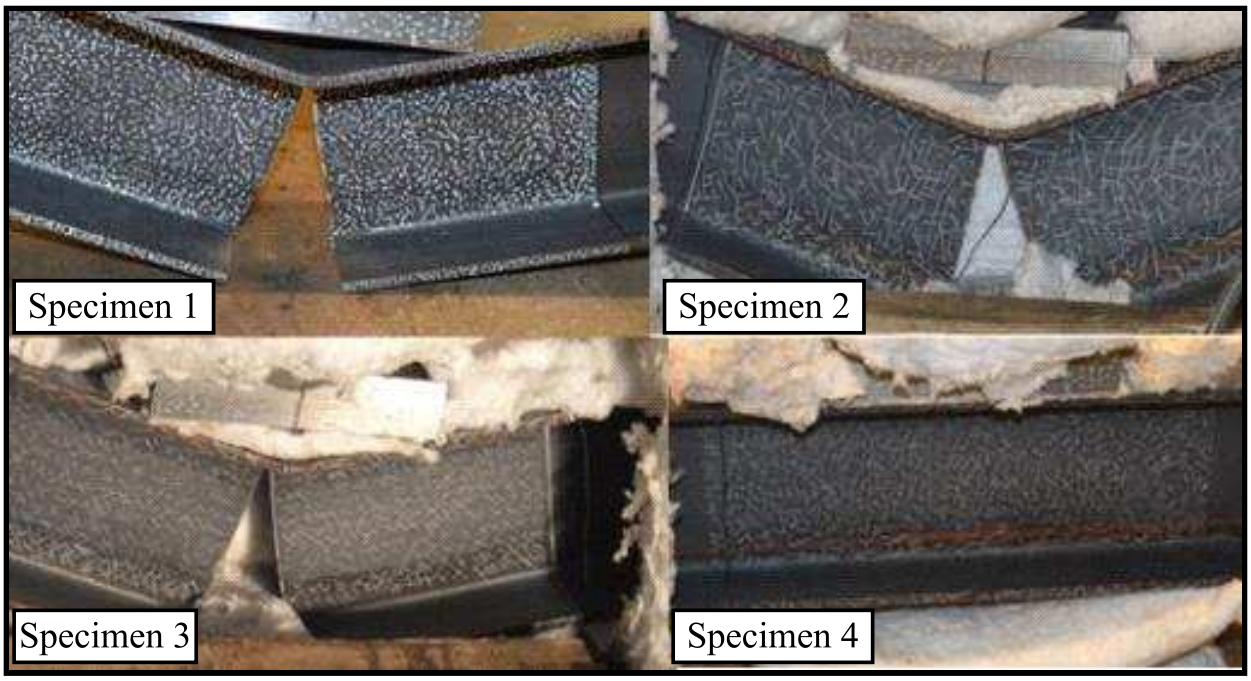

Figure 4-27: Comparison of global failure behavior for all specimens

Observing Table 1, the stiffness decreases significantly with increasing temperature. The stiffness in specimen 1, which was tested at ambient temperature is almost 50 percent larger than that of specimen 2 and the stiffness decreases further more in specimen 3 and specimen 4. This is due to degradation of modulus of elasticity of steel at elevated temperature.

When evaluating the results, it is seen that specimen 2 failed at a load of 119.70 kN which is higher than 113.25 kN recorded for specimen 1. This increase in load capacity can be attributed to the increase in ductility energy due to the elevated temperature since specimen 1 was tested at ambient temperature while specimen 2 was tested at non-uniform elevated temperature with the maximum temperature of up to 200 °C. The fracture toughness of steel is also an influential parameter in this case. As the temperature increases, the modulus of elasticity of steel decreases resulting in lower stiffness; however, this is counteracted by an increase in fracture toughness, which results in an

enhanced resistance to fracture for the beams. A similar trend is observed for specimen 3, which was tested at elevated non-uniform temperatures of up to 400 °C. Specimen 4 tested at temperature distribution of up to 600 °C failed in excessive deflection. Specimen 4 did not fracture and this is due to degradation of steel stiffness at elevated temperature, which was offset by an increase in the fracture toughness capacity of the steel.

4.3.3 Strain and Displacement Fields

In this section digital image correlation analysis was conducted to create vertical displacement fields and strain fields around the cracked region, which is the midpoint of the beam specimens. The maximum value of the vertical displacement fields generated through the use of DIC are compared with the maximum displacement values obtained from load-displacement curves. These displacement and strain fields are taken from the last mechanical loading step directly before the specimens' failure. Therefore, the strain fields are non-linear because the applied loads were up to ultimate failure. There is no other way to verify these strain fields theoretically. However, a 3D finite element analysis using software such as ABAQUS could be used to verify the non-linear strain field developed experimentally.

4.3.3.1 Specimen 1 Strain and Displacement Fields

Figure 4-28 and 4-29 contains strain and displacement fields respectively for specimen 1 that was tested at ambient temperature. As shown in Figure 4-28, the maximum displaced can be read on the contour color plot is 22.5 mm, which is close (27.64 mm) to the maximum displacement obtained from load-displacement plot. The important point to consider here is that the two maximum displacements are obtained from independent sources (digital image correlation and

load-displacement data). This indicate that the digital image correlation method and results are accurate.

The non-linear strain field for specimen 1 shows high strain around the region of crack in the bottom flange as indicated in Figure 4-29. The strain field decreased away from the bottom flange cracked region. The high strain near the crack region is an indication of plastification and stress concentration near the crack.

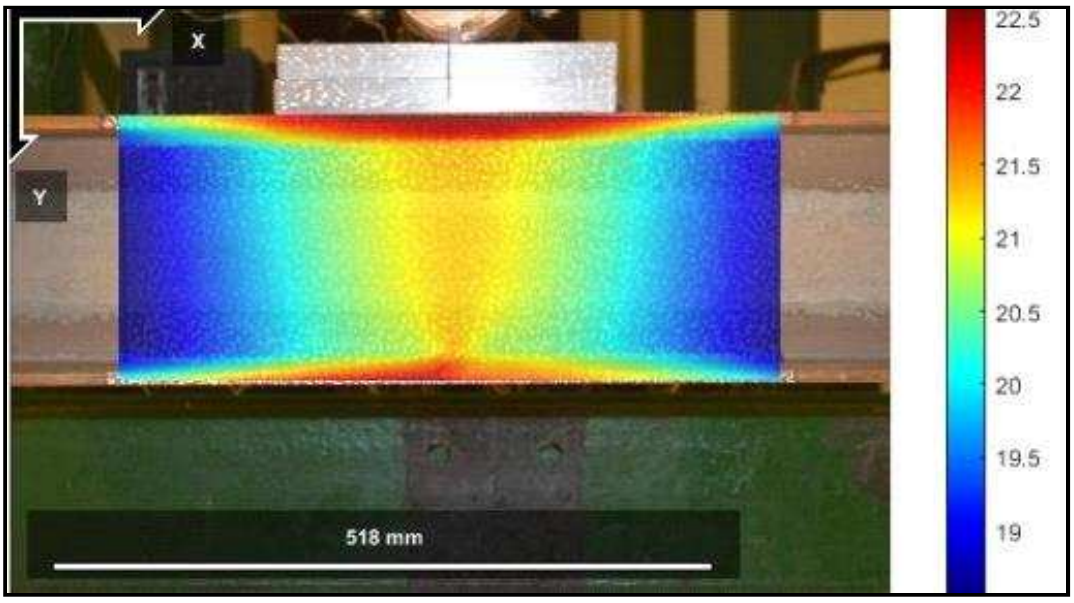

Figure 4-28: Specimen 1 displacement field right before failure

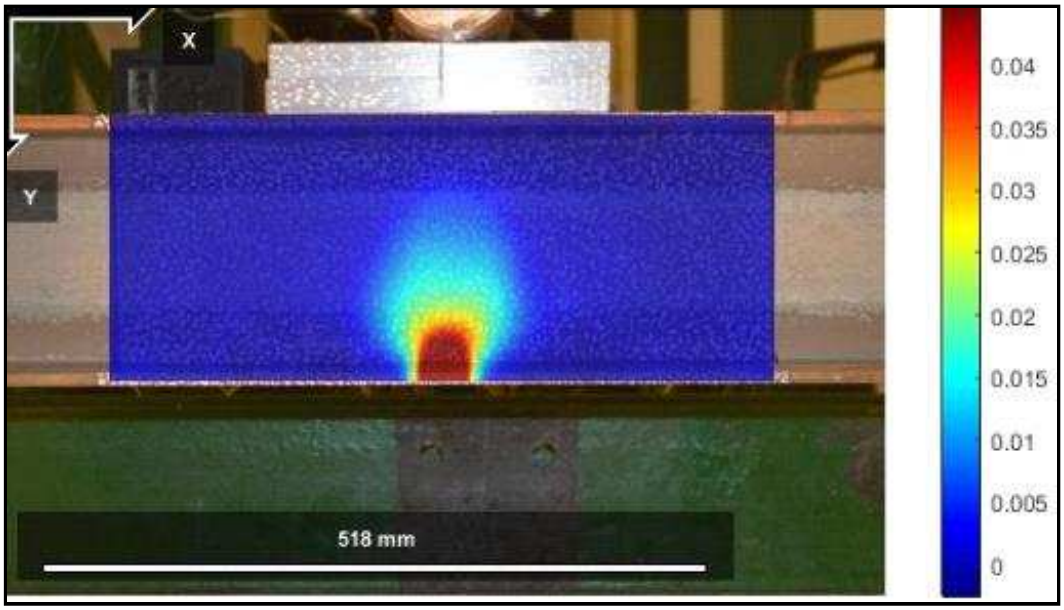

Figure 4-29: Specimen 1 nonlinear strain field right before failure

4.3.3.2 Specimen 2 Strain and Displacement Fields

Figure 4-30 includes vertical displacement of specimen 2 right before fracture, which was tested at non-uniform temperature of up to 200 °C. Figure 4-31 contains non-linear strain field of specimen 2 right before fracture. The insulation chamber made out of ceramic fiber glass around the beam specimen can be seen in figures. It had a door in front and it was opened every time a picture was taken. The frequent need for taking a picture in every step is for using the images for the DIC analysis.

The non-linear strain field for specimen 2 shown in Figure 4-31 has a similar overall behavior with specimen 1. However, the effect of temperature adds up to the nonlinearity of the strain field. Also, digital image correlation accuracy decreased with presence of temperature as DIC methods uses relative movement of pixels in a picture with respect to the reference picture, which is the unloaded picture of the same field.

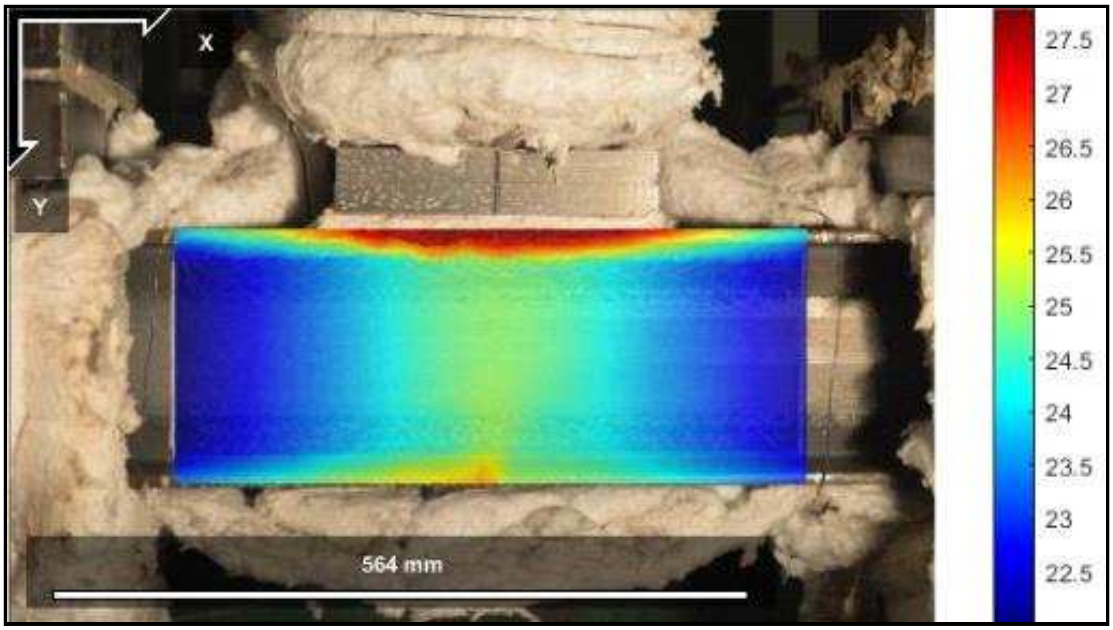

Figure 4-30: Specimen 2 vertical displacement field taken right before failure

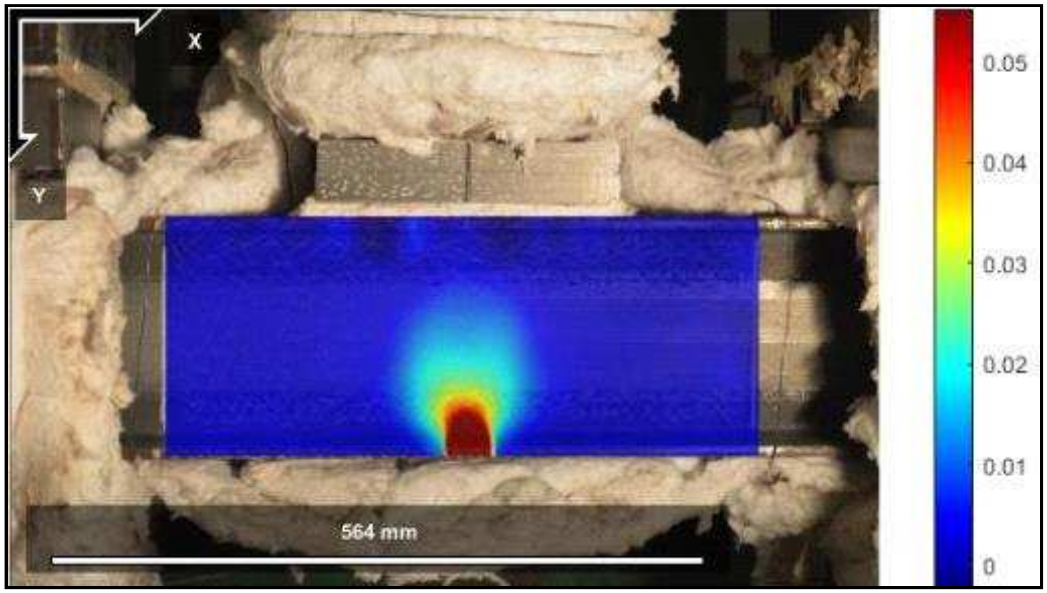

Figure 4-31: Specimen 2 nonlinear strain field right before failure

4.3.3.3 Specimen 3 Strain and Displacement Fields

Vertical displacement and nonlinear strain field for specimen 3 is included in Figure 4-32 and 4-33, respectively. The maximum vertical displacement of 30 mm, which was generated from the DIC analysis is consistent with the maximum displacement of 37.11 mm from the load-displacement curve.

The nonlinear strain value field in specimen 3 is higher than that of specimen 2 as expected. However, around the crack tip the strain field is lower for specimen 3 when compared to that of specimen 2. This could be due to the level of sharpening at the crack tip as a result of the crack introduction process.

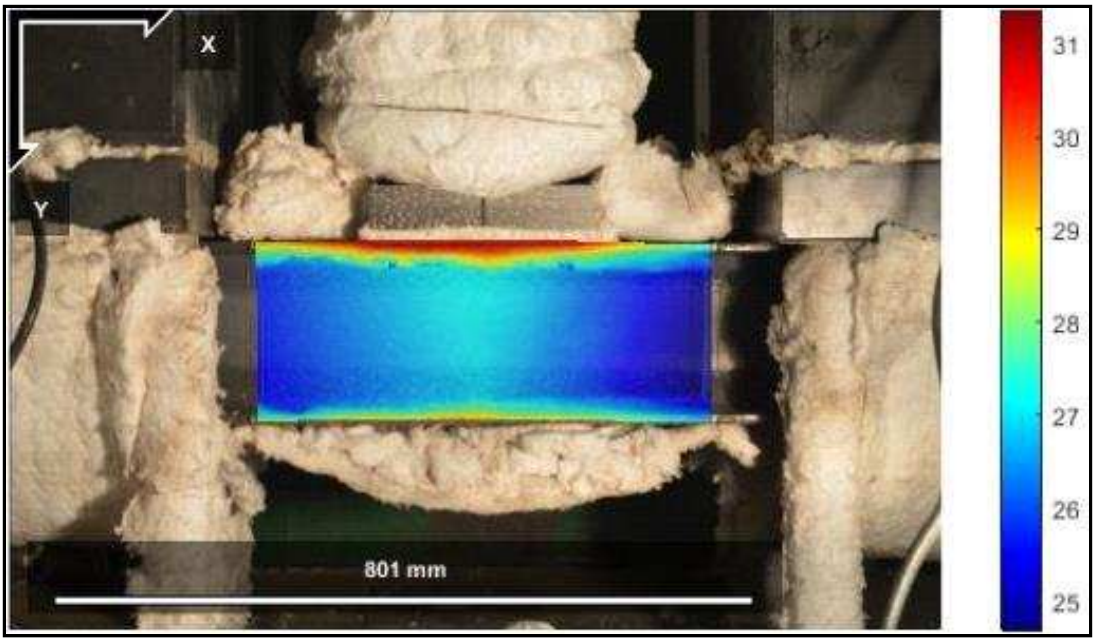

Figure 4-32: Specimen 3 vertical displacement field right before failure

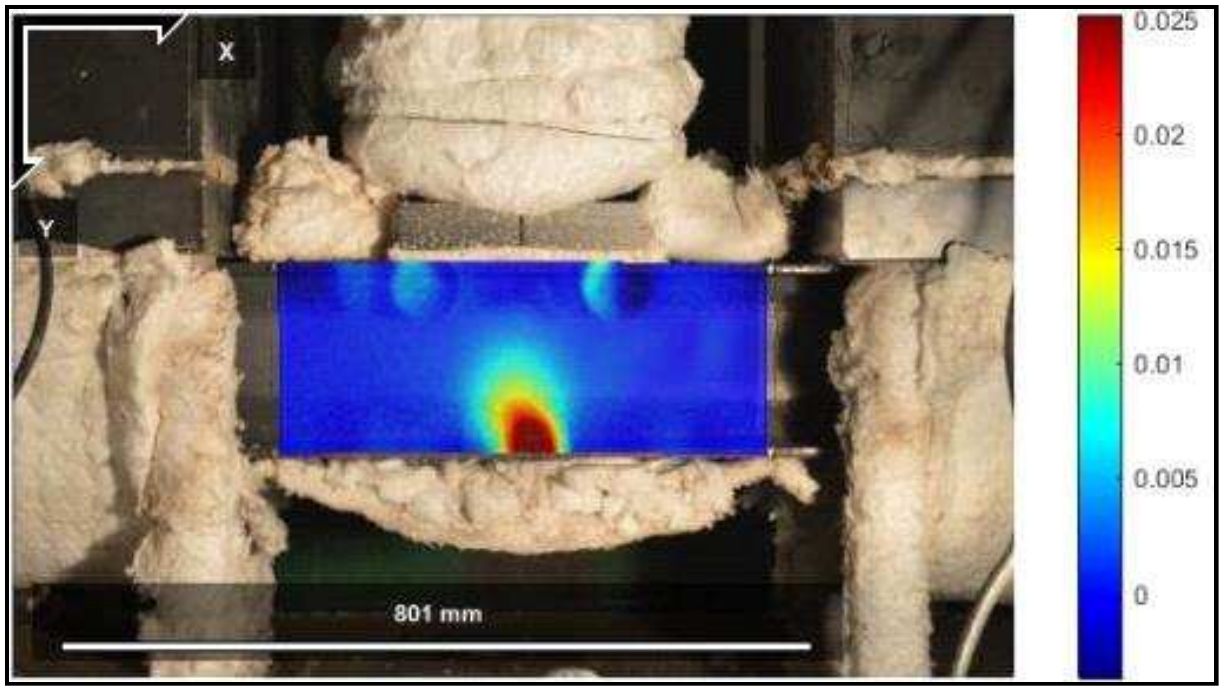

Figure 4-33: Specimen 3 strain field before failure

4.3.3.4 Specimen 4 Strain and Displacement Fields

Specimen 4 is the only test in which the specimen failed by excessive deflection rather than fracture. The vertical displacement field is included in Figure 4-34. The maximum deflection is about 90 mm, which compares well with the measure value of 95.73 mm from the load-displacement data. The deflection is much larger than that of the other specimens as expected. Specimen 4 shows higher displacement in the left portion of the image due to the excessive deflection that caused interaction between the beam and the out-of-plane bracing elements.

The nonlinear strain field for specimen 4 tested at non-uniform temperature of up to 600 °C is included in Figure 4-35. Since this specimen did not fracture, no concentration of high strain is seen near the bottom flange where the pre-existing crack is located. The crack did not grow at all and the beam simply deflected. There is a high strain concentration spot seen in Figure 4-35 at the

top right side. This does not necessarily represent any failure criterion and could possibly be due to experimental error in photo capturing. Since this region is not in the area of interest, which is near the crack, it can be neglected.

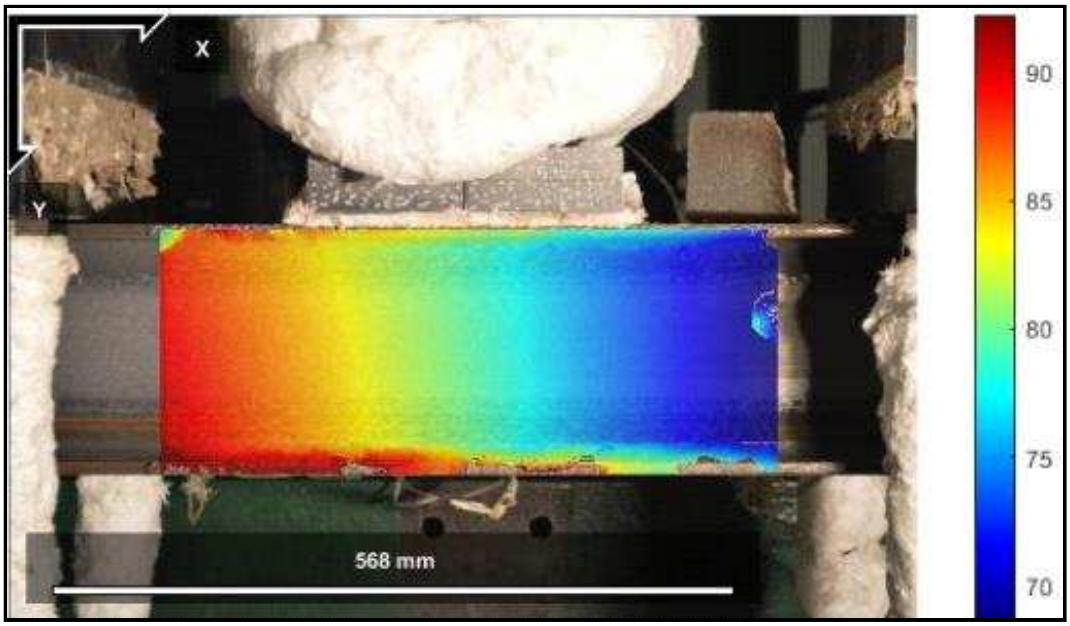

Figure 4-34: Specimen 4 vertical displacement field before failure

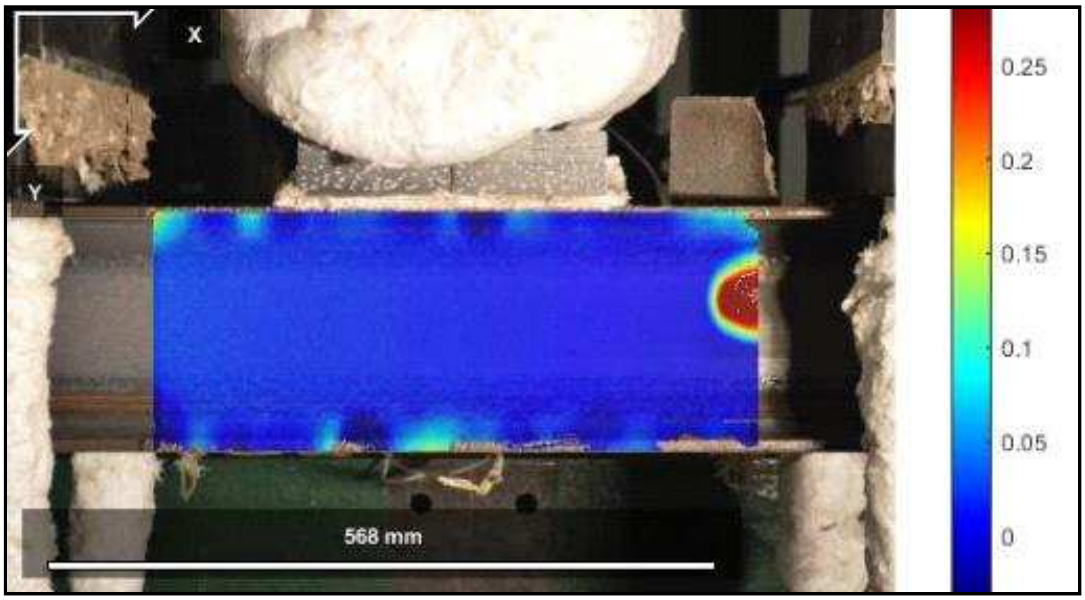

Figure 4-35: Specimen 4 nonlinear strain field right before failure

4.3.3.5 Comparison of Strain and Displacement Fields for all Specimens

Figure 4.36 below shows comparison of all DICs corresponding to the displacement field for all specimens. As can be seen in the figure, the displacement field for specimen 1 is more spatially distributed as opposed to specimen 2 and 3 where the displacement is more localized in the flange due to localized flange deformation as result of the heat. Specimen 4 shows higher displacement in the left portion of the image due to the excessive deflection that caused interaction between the beam and the out-of-plane bracing elements. Figure 4-37 shows the localized strain around the crack tip for specimens 1, 2, and 3 as expected. Specimen 4 does not show localized strain around the crack since the specimen failed by global bending.

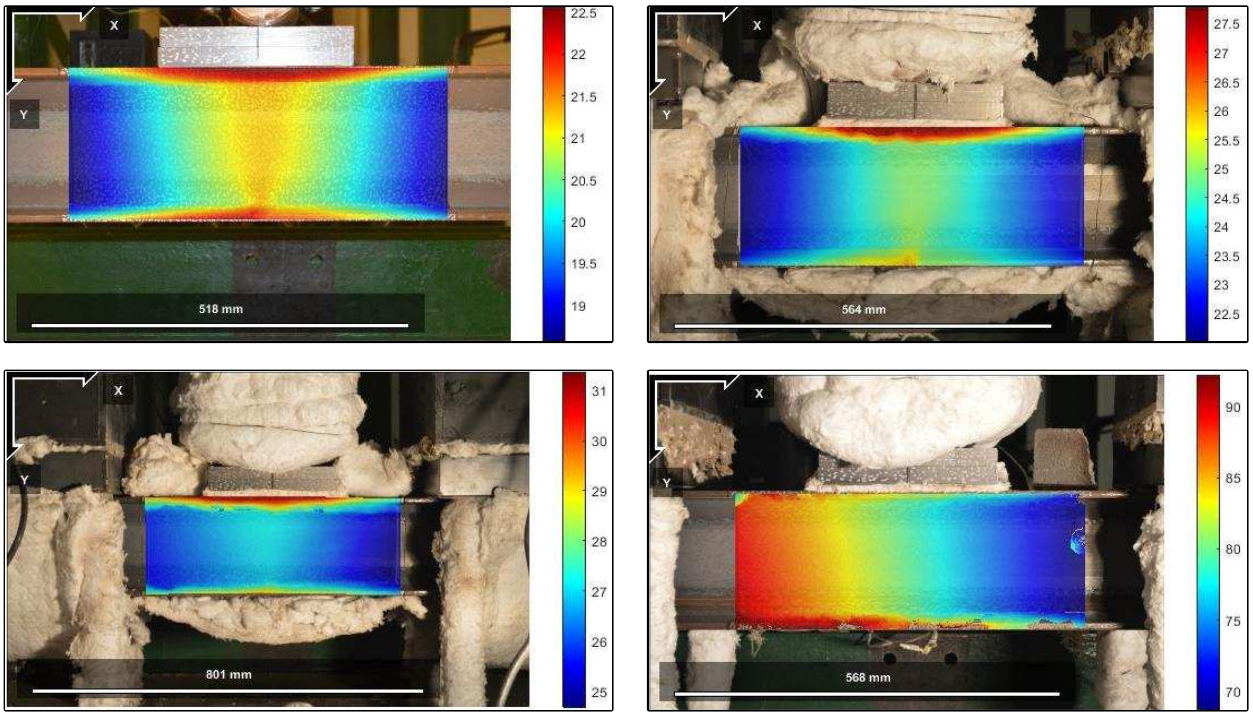

Figure 4-36: Specimen 4 nonlinear strain field right before failure

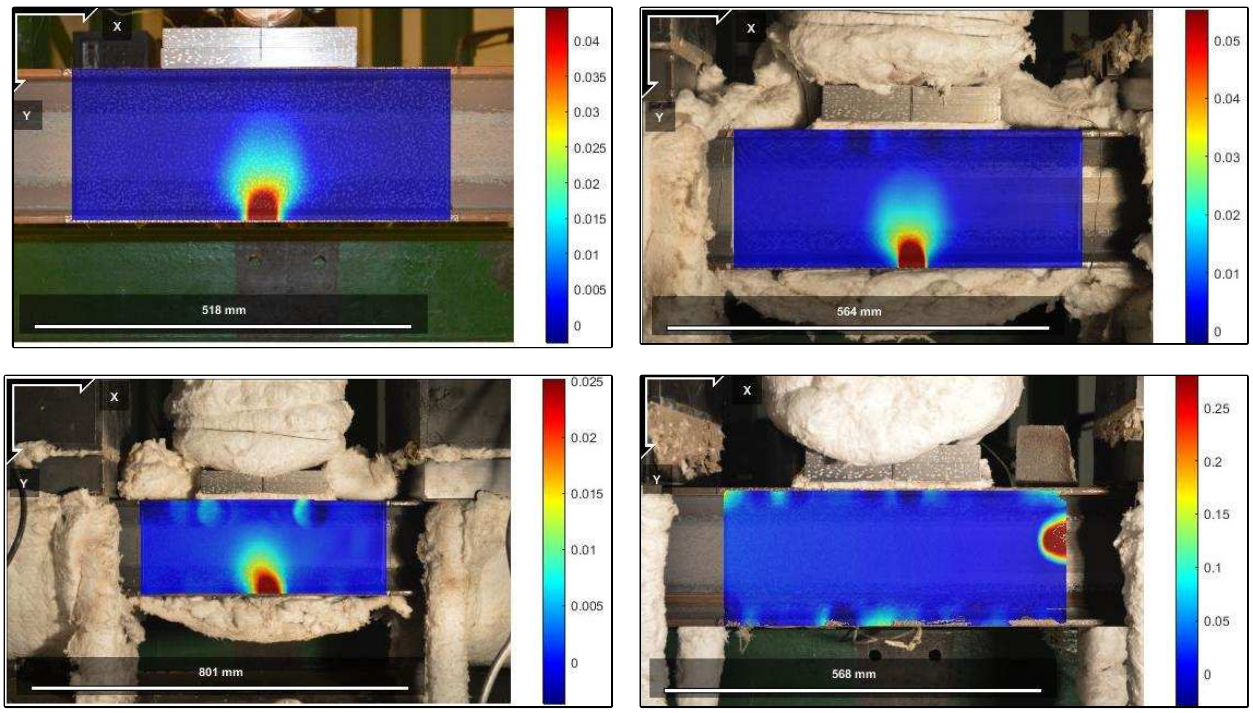

Figure 4-37: Specimen 4 nonlinear strain field right before failure

Chapter 5 - Conclusions, Field Implications & Future Works

5.1 Conclusions

In this study, experimental tests were conducted to evaluate the potential for fracture of W8X24 beams with pre-existing crack at the bottom flange under the combined load of non-uniform elevated temperature distribution and mid span point load. The tested beams were designed to represent steel bridge beam with pre-existing fatigue crack that is subjected to elevated steady state temperature. The experimental program and the instrumentation plan allowed for successful testing of four w-section beam specimens. The results of the analysis and data post processing from the experimental testing and instrumentation plan are outlined below.

5.1.1 Time-Temperature Curves

Using ceramic heaters installed on top flange, time temperature curves were developed for each specimen except specimen 1 which was tested at ambient temperature. These time temperature curves represent non-uniform temperature distribution along and across the beam. 2D finite element analysis was helpful in visualizing the steady temperature distribution in 2D along the specimen beams.

5.1.2 Mechanical Failure Results

1. With increasing non-uniform temperature, fracture toughness of steel increases and therefore a beam could tolerate more load before fracture in comparison with a cracked loaded beam at lower temperature.
2. The stiffness of the cracked steel beam decreases with increasing temperature

3. Reduction in the modulus of elasticity due to increase in temperature causes a competition in the failure mode between global bending and fracture along the cracked section.
4. From ambient temperature up to 400 Deg. C, fracture dominates the behavior. However, when the temperature reaches 600 Deg. C, such as the case with specimen 4, the behavior changes and the specimen fails in excessive deflection before it fractures. This is a result of reduction in the modulus of elasticity of steel, which degrades by almost 50% at 600 Deg. C.
5. When evaluating the fracture surface profile of the three specimens that failed in fracture, it can be concluded that presence of Chevron marks, which is a sign of brittle fracture, decreases with increasing non-uniform temperature. Some Chevron marks are seen in parts of specimen 1 fracture profile. For specimen 2 and 3, Chevron marks are not present. Instead, shear lips and angled surfaces are seen in the specimens which are signs of ductile fracture.

5.2 Field Implication

Steel bridge under fire event is a major concern that should be addressed through quantitative methods. The problem is further exacerbated by the existence of pre-existing fatigue cracks in steel bridges. The study presented in this thesis provide an certain level of understanding between the competition between ductile fracture and overall global deflection as a function of temperature. The data obtained in this study is intended to fill the gap in the literature on the performance of large-scale beams with pre-existing cracks and under elevated temperature. The data can be used to calibrate numerical models that can be utilized to conduct parametric studies for the development of performance-based guidelines.

5.3 Recommendations for Future Works

The following research aspects are recommended to be included in future studies.

1. Due to project constraints, only four specimens were tested at four selected temperatures. It is recommended that for future work, more specimens of different sizes be tested. This will allow for the evaluation of the effect of the geometrical dimensions of the beam on the temperature distribution and fracture characteristics.
2. Although the designated non-uniform temperature distribution provided a baseline comparison of the response against a non-heated beam represents, it is recommended that future testing includes time-temperature curves that represent real fire scenarios and temperature level on a bridge.
3. In addition to experimental testing, numerical finite element models could be developed and calibrated using experimental results then used in parametric studies to evaluate the effect of various temperature distributions and geometrical features of various beams.
4. Using the results of the experimental studies and the finite element simulations, closed form solutions can be developed to allow for accurate prediction of load displacement curves without the need of extensive experimental testing or finite element programs.

References

American Association of State Highway and Transportation Officials (AASHTO). (2004). LRFD bridge design specifications, 3rd Ed., Washington, D.C.

Ahrens, M. (2000). *US vehicle fire trends and patterns*. National Fire Protection Association.

American Institute of Steel Construction (AISC). (2007). Why do designers & owners choose structural steel? Retrieved September 28, 2016, from https://www.aisc.org/content.aspx?id=3792

American Society of Civil Engineers (ASCE). (1994). *Minimum design loads for buildings and other structures* (Vol. 7). American Society of Civil Engineers.

An, X., Ning, Y., Ma, G., & He, L. (2014). Modeling progressive failures in rock slopes with non-persistent joints using the numerical manifold method. *International Journal for Numerical and Analytical Methods in Geomechanics*,*38*(7), 679-701.

ASTM E119a (2008). "Standard Methods of Fire Test of Building Construction and Materials." American Society for Testing and Materials, West Conshohocken, PA.

ASTM, E. 2. (2007). Standard Test Methods for Notched Bar Impact Testing of Metallic Materials.

Aziz, E. M. (2015). *Response of fire exposed steel bridge girders*. Michigan State University.

Aziz, E. M., Kodur, V. K., Glassman, J. D., & Garlock, M. E. (2015). Behavior of steel bridge girders under fire conditions. *Journal of Constructional Steel Research, 106*, 11-22.

Bennets I, Moinuddin K. (2009). "Evaluation of the impact of potential fire scenarios on structural elements of a cable-stayed bridge." Journal of Fire Protection Engineering, vol. 19: pp. 85–106.

Blaber, J. (n.d.). Ncorr Digital Image Correlation MATLAB Code (Version V1.2) [Computer software]. Retrieved September 29, 2016, from http://www.ncorr.com/index.php

Bletzacker, R.W. (1966). "Effect of Structural Restraint on the Fire Resistance of Protected Steel Beam Floor and Roof Assemblies." Final Report. EES 246/266. Ohio State University, Columbus, Ohio.

Bradt, T. G. (2011). *Effects of fire damage on the structural properties of steel bridge elements*. Purdue University.

Cinitha, A., Umesha, P. K., & Iyer, N. R. (2012). Numerical investigation on structural behavior of steel beams under elevated temperature. *Journal of Structural Engineering*, *39*(5).

Connor, R. J., Dexter, R., & Mahmoud, H. (2005). NCHRP synthesis 354.*Transportation Research Board, Washington, DC*, 12. DC.

Dexter, R. J., & Ocel, J. M. (2013). *Manual for repair and retrofit of fatigue cracks in steel bridges* (No. FHWA-IF-13-020).

Dexter, R., H. Mahmoud, J. Padula, and G. Riveros. (2007). *Fitness-for-Purpose Evaluation of Hydraulic Steel Structures*. ERDC TR-07-15. Vicksburg, MS: U.S. Army Engineer Research Development Center, U.S. Army Corps of Engineers.

Dotreppe, J.C., Majkut, S., and Franssen, J.M. (2006). "Failure of a Tied-arch Bridge Submitted to a Severe Localized Fire, Structures and Extreme Events." IABSE Symposium: pp. 272-273.

Dowling, N. E. (1993). Mechanical behavior of materials Prentice-Hall. *Englewood Cliffs, NJ*, 347.

Eurocode, E. C. I. (1994). 1: basis of design and design actions on structures. *European Committee for Standardization, Brussels, Belgium*.

Fike, R., & Kodur, V. (2011). Enhancing the fire resistance of composite floor assemblies through the use of steel fiber reinforced concrete. *Engineering Structures*, *33*(10), 2870-2878.

Fisher, J. W., Kulak, G. L., & Smith, I. F. (1998). *A fatigue primer for structural engineers* (No. IMAC-BOOK-1998-002). National Steel Bridge Alliance, American Institute of Steel Construction.

Garlock, M., Paya-Zaforteza, I., Kodur, V., & Gu, L. (2012). Fire hazard in bridges: Review, assessment and repair strategies. *Engineering Structures*,*35*, 89-98.

International Building Code (IBC). (2012). International Building Code.

International Organization for Standardization (ISO). (1999). ISO 834. Retrieved October 12, 2016, from https://www.iso.org/obp/ui/#iso:std:iso:834:-1:ed-1:v1:en

Kodur, V. K. R., & Harmathy, T. Z. (2015). Properties of Building Materials 9. *SFPE Handbook of Fire Protection Engineering*, 277.

Kodur, V., Aziz, E., & Dwaikat, M. (2012). Evaluating fire resistance of steel girders in bridges. *Journal of Bridge Engineering*, *18*(7), 633-643.

Mahmoud, H. N., & Dexter, R. J. (2005). Propagation rate of large cracks in stiffened panels under tension loading. *Marine Structures*, *18*(3), 265-288.

Mahmoud, H., & Riveros, G. (2014). Fatigue reliability of a single stiffened ship hull panel. *Engineering Structures*, *66*, 89-99.

Mahmoud, H., Ellingwood, B., Turbert, C., & Memari, M. (2015). Response of steel reduced beam section connections exposed to fire. *Journal of structural engineering*, *142*(1), 04015076.

Mahmoud, H., Memari, M., & Turbert, C. (2015). The effect of earthquake characteristics on the localized behavior of moment connections under fire.

Manual, A. I. S. C. (2005). Steel Construction Manual.

McIntosh, P., & Farid, M. (2011). Fire protection of steel structure through the application of phase endothermic reactions. *Chemeca 2011: Engineering a Better World: Sydney Hilton Hotel, NSW, Australia, 18-21 September 2011*, 1252.

Memari, M., & Mahmoud, H. (2014). Performance of steel moment resisting frames with RBS connections under fire loading. *Engineering Structures*, *75*, 126-138.

Memari, M., Mahmoud, H., & Ellingwood, B. (2014). Post-earthquake fire performance of moment resisting frames with reduced beam section connections. *Journal of Constructional Steel Research*, *103*, 215-229.

Mendes P., Valente J., Branco F. (2000). "Simulation of ship fire under Vasco da Gama Bridge." ACI Structural Journal, vol. 97(2): pp. 285–90.

Naser, J. M., & Serrano Toledano, F. (2011). Analysis of vibration-induced fatigue cracking in steel bridges. Chalmers University of Technology, Göteborg, Sweden

National Bridge Inventory (NBI). (2013, December). Bridges by Year Built, Year Reconstructed and Material Type 2013. Retrieved October 10, 2016, from https://www.fhwa.dot.gov/bridge/nbi/no10/yrblt_yrreconst13.cfm

National Fire Protection Association (NFPA). (2012). Building Construction and Safety Code.

National Highway Traffic Safety Administration (NHTSA-FARS). (n.d.). National Fatality Statistics. Retrieved October 03, 2016, from http://www-fars.nhtsa.dot.gov/Main/index.aspx

NPTEL. (n.d.). Engineering Fracture Mechanics. Retrieved October 10, 2016, from http://nptel.ac.in/courses/112106065/

Sun, C. T., & Jin, Z. (2012). *Fracture mechanics*. Waltham, MA: Academic Press.

The Federal Highway Administration (FHWA). (2002, October). Bridge Rebuilt on The Fast Track. Retrieved September 28, 2016, from http://www.fhwa.dot.gov/publications/publicroads/02sep/05.cfm

Vimonsatit, V., Tan, K. H., & Qian, Z. H. (2007). Testing of plate girder web panel loaded in shear at elevated temperature. *Journal of structural engineering*, *133*(6), 815-824.

Wainman, D. E., & Kirby, B. R. (1989). *Compendium of UK Standard Fire Test Data: Unprotected Structural Steel*. British Steel Technical, Swinden Laboratories.

Wald, F., da Silva, L. S., Moore, D. B., Lennon, T., Chladna, M., Santiago, A., ... & Borges, L. (2006). Experimental behavior of a steel structure under natural fire. *Fire Safety Journal*, *41*(7), 509-522.

Wright, W., Lattimer, B., Woodworth, M., Nahid, M., & Sotelino, E. (2013). Highway bridge fire hazard assessment, draft final report. *Virginia polytechnic institute and state university. TRB Project*, (12-85).

Zhu, X. K., & Joyce, J. A. (2012). Review of fracture toughness (G, K, J, CTOD, CTOA) testing and standardization. *Engineering Fracture Mechanics*,*85*, 1-46.